8-2000

Statistically designed experimental study of sol-gel based film coating scheme for high temperature super conductors and buffer materials and related manufacturing process cost evaluation

Kevin Trembath

Follow this and additional works at: https://trace.tennessee.edu/utk_gradthes

To the Graduate Council:

I am submitting herewith a thesis written by Kevin Trembath entitled "Statistically designed experimental study of sol-gel based film coating scheme for high temperature super conductors and buffer materials and related manufacturing process cost evaluation." I have examined the final electronic copy of this thesis for form and content and recommend that it be accepted in partial fulfillment of the requirements for the degree of Master of Science, with a major in Chemical Engineering.

Atul Sheth, Major Professor

We have read this thesis and recommend its acceptance:

Accepted for the Council:
Carolyn R. Hodges

Vice Provost and Dean of the Graduate School

(Original signatures are on file with official student records.)
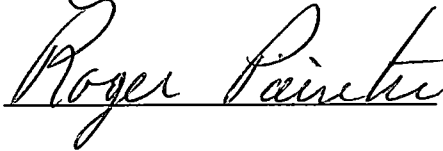
To the Graduate Council
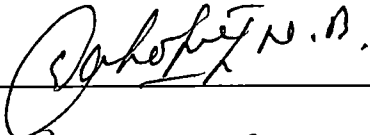
I am submitting herewith a thesis written by Kevin Trembath entitled "Statistically Designed Experimental Study of Sol-Gel Based Film Coating Scheme for High Temperature Super Conductors and Buffer Materials and Related Manufacturing Process Cost Evaluation" I have examined the final copy of this thesis for form and content and recommend that it be accepted in partial fulfillment of the requirements for the degree of Master of Science, with a major in Chemical Engineering.

_____
Atul Sheth, Major Professor

We have read this thesis and
recommend its acceptance:

_____

_____

_____

Accepted for the council:

_____
Associate Vice Chancellor and
Dean of The Graduate School

STATISTICALLY DESIGNED EXPERIMENTAL STUDY OF SOL-GEL BASED FILM COATING SCHEME FOR HIGH TEMPERATURE SUPER CONDUCTORS AND BUFFER MATERIALS AND RELATED MANUFACTURING PROCESS COST EVALUATION

A Thesis
Presented for the
Master of Science
Degree
The University of Tennessee, Knoxville

Kevin Trembath
August 2000

Abstract

In this work, processing factors that influence the epitaxial growth of LaAlO$_3$ on cubic-textured nickel substrates via sol-gel route are investigated using a Taguchi L12 experimental design Through experimental data collected on omega FWHM, phi FWHM, and composition of orientations, a set of models was generated to characterize the epitaxial growth response to the processing factors consisting of thermal processing time, temperature, atmosphere, nickel surface roughness, degree of precursor hydrolysis, withdrawal rate, and precursor solution concentration The processing conditions are then identified that would produce the greatest degree of epitaxial growth as defined through a nondimensional term

Also, this work explores the manufacturing aspects of the sol-gel based film coating scheme through a preliminary costing study. Production objectives were assigned to be directly comparable to similar cost studies carried out for other processes such as evaporative electron beam, pulsed laser deposition, and metal organic chemical vapor deposition. Also, the final product cost was compared to an industrial goal and sensitivity of assumptions made within the study are examined in regards to meeting the goal.

TABLE OF CONTENTS

LIST OF TABLES

LIST OF FIGURES

NOMENCLATURE

AFM	Atomic Forces Microscopy
ANOVA	Analysis of Variance
BSCCO	Bismuth Strontium Calcium Copper Oxide
e-beam	Electron Beam
FWHM	Full Width at Half Maximum
H_c	Critical Opposing Magnetic Field Strength
HTSC	High Temperature Superconductor
IBAD	Ion Beam Assisted Deposition
IPA	Isopropanol
J_c	Critical Current Density
kA	Kiloampere
M	Molarity (moles / L)
MA	Mega Ampere
MOCVD	Metal Organic Chemical Vapor Deposition
MSE	Mean Square Error
MSR	Mean Squares Regression
MVA	Mega Volt Ampere
NIST	National Institute of Standards and Technology
ORNL	Oak Ridge National Laboratory
NiO	Nickel Oxide
PIT	Powder-In-Tube (Process)

PLD	Pulsed Laser Deposition
PSI	Phase-Shifting Interferometry
R_a	Roughness Average
R^2	Correlation Coefficient
RABiTS	Rolling Assisted Biaxially Textured Substrate
$\bar{S}$	S-bar (Variance Model)
S_y^2	Mean Variance
SEM	Scanning Electron Microscope
SSE	Sums Squares Error
SSR	Sum Squares Regression
SST	Sums Square Total
T_c	Critical Temperature
TGA	Thermogravametric Analysis
UTSI	University of Tennessee Space Institute
VOC	Volatile Organic Compound
VSI	Vertical Scanning Interferometry
XRD	X-ray Diffraction
YBCO	Yttrium Barium Copper Oxide ($Y_1Ba_2Cu_3O_7$)
$\bar{Y}$	Y-bar (Response Model)
$\hat{y}$	Regression Model Points
y	Observed Data Points
$\bar{y}$	Arithmetic Mean of Data Points

YSZ   Yttrium Stabilized Zirconium

2θ 2 Theta (Detector Axis on XRD)

CHAPTER 1

INTRODUCTION

Superconductivity: Overview

What is superconductivity and superconductors? The term superconductivity generally is used to refer to the state of a material, which allows the complete conduction of electricity without resistance loses. Superconductors are also identified by their additional ability to repel magnetic fields away. A common demonstration of superconductivity is to allow a bar magnet to levitate over a chilled slab of superconducting material.

H.L Onnes reported the first superconducting material, Mercury, in 1911. In subsequent decades, researchers discovered other numerous superconductors. However, three major parameters; critical temperature (T_c), current density (J_c), and critical opposing magnetic field strength (H_c) limited all of these superconductors. Above critical values, electrical resistances reappeared and superconductors no longer were "super". For most of superconductivity's history, weak current carrying capacities and expensive refrigeration systems hampered the development of practical uses for superconductivity (Sheahen, 1994). Therefore, superconductivity was thought of as a mature or closed science and little in the way of industrialization of the technology occurred (Sheahen, 1994).

However, in 1986, Bednorz and Muller in IBM's Zurich Research Lab developed a new breed of superconductors. This next generation of superconductors were coined the

name high temperature superconductor (HTSC). HTSCs were capable of being run at temperature above 77K that allowed the use of less expensive liquid nitrogen cooling systems. HTSCs also performed better in the areas of current capacity and magnetic field resistance. HTSCs generated excitement from their potential applications and from the fact that they were discovered as an experimental surprise in a scientific area once thought closed (Sheahen, 1994). Soon thereafter, a HTSC superconducting industry was born in the midst of an explosive race of research into HTSCs

Recently, the fruits of this emerging industry are beginning to take shape. In May 1998, Waukesha Electric Systems announced the successful testing of a 1 Mega-Volt-Ampere (MVA), HTSC prototype power transformer (Waukesha Electric Systems, 1998). They also reported confirmation of technical feasibility and advantages of prototype scale-up to commercial size 30MVA transformers (Waukesha Electric Systems, 1998). In August 1999, the Southwire Company installed three 30-meter length HTSC wires at several manufacturing plants and anticipates carrying live loads in early 2000 (Southwire, 1999). This event may mark the first successful implementation of HTSC cables in field service With market projections of HTSC materials for 2020 ranging from $30 billion (Southwire's) to $122 billion (3M's), the industry seems to be on the verge of an explosive growth once proven processes and products are in place (Southwire, 1999; 3M, 2000). Therefore, research into the industrialization of current and newly developing HTSC technologies are gaining importance.

The Challenges of an Emerging Industry

Necessary to the successful development of any industrial process is an understanding of the critical process factors. This understanding embodies the comprehension of the significance of process factors in their individual and collective effect on product quality. This understanding allows engineers the ability to assess what tradeoffs are necessary to ensure the commercial as well as technical feasibility of a process. The challenge for a continued growth of the HTSC industry is to be able to effectively and to efficiently assess feasibility of emerging processes. The frantic pace of research and development in the HTSC field has created a wealth of unique processes, which lends to this challenge.

Objectives and Approach

This thesis concentrates on the area of HTSC wire fabricating technology. This thesis aims to explore both the technical and the commercial aspects of the sol-gel route for coated conductor manufacturing. Some of the technical aspects were examined through multifactorial, bench scale experiments. This work focused specifically on identifying the most influential processing parameters and their effects on epitaxial growth of layers, which act as the foundations upon which the HTSC layers are subsequently grown.

Commercial aspects were assessed through a preliminary life-cycle costing study. The sol-gel process schematic is shown as figure 1.1 on page 4. The goal of such an

Al sec-butoxide → Dissolver →

Alcohol Recovery ↑

2-methoxyethanol → Dissolver →

La isopropoxide → Dissolver →

2 methoxyethanol → Dissolver →

Reflux Distillation →

2-methoxyethanol + Water

Partial Hydrolyzer →

Lanthanum Aluminate Precursor

96% Ar + 4% H2 ↓

High Purity Ni-Rich Feed Stock → Rolling Operation → Annealing Furnance 900C → Textured Nickel Tape

LaAlO3 Dip Coating Unit

Off gas Treatment ↑

Pyrolyzer 400C

O2 ↑

96% Ar + 4% H2 →

Batch Thermal Treatment 1200C

Copper Methoxide → Dissolver ← Triethanolamine

Barium Isopropoxide

2-methoxyethanol → Dissolver →

Dissolver →

Yttrium Isopropoxide ↑

Alcohol Recovery ↑

Reflux Distillation →

Partial Hydrolyzer →

YBCO Precursor Solution

2-methoxyethanol + Water

O2 ↓

Pyrolyzer 400C ←

Off gas Treatment ↓

YBCO Dip Coating Unit

Batch Thermal Treatment 900C ←

Finished Product For Passivation And Slitting Processes

O2 ↑

Figure 1 1 Sol-Gel Based Film Coating Scheme for HTSC Processing

4

industrial process would be to produce 18,000 kilometers of the superconductor each year for ten years These goals were developed on the basis of life cycle cost study work performed by Dr. James Chapman at the University of Tennessee Space Institute (UTSI) on electron beam deposition (e-beam), pulsed laser deposition (PLD), and metal organic chemical vapor deposition (MOCVD) routes to superconductor manufacturing (Chapman 1998, 1999).

CHAPTER 2

BACKGROUND AND LITERATURE REVIEW

HTSC Wire Fabrication Techniques

Early wire fabrication methods combined standard wiremaking techniques such as drawing, swaging, and extruding with modified heat treatment for HTSCs. HTSC powders were produced and then given wire shape and form by a variety of methods: congealing powders with a binder, powder packing in tubes to be extruded, and depositing HTSC powder on a core These methods also included a heat treatment step to produce the superconducting solid phase of the HTSC. Silver was often used as the form-holder or binder in these processes because of several key properties. First, ceramic HTSCs are naturally brittle and easy to fracture. Silver, on the other hand, possesses greater fracture toughness, thus adding to the wire's overall toughness as a form holder. Next, silver has good conductor properties, which provides a relatively low-resistance link between HTSC grains when used as binder Finally, silver does not interfere with oxygen stoichiometry of HTSC during heat treatment (Sheahen, 1994). Silver offers the fastest diffusion path for oxygen of all metals and silver oxides breakdown at relatively low temperatures to avoid scavenging of the oxygen (Sheahen, 1994).

An example of such a powder process would be a popular method used by a variety of companies including the American Superconductor and Intermagnetics General. This method is called power-in-tube (PIT). Figure 2.1, page 7, shows a typical PIT process for the BSCCO (Bismuth Strontium Calcium Copper Oxide) HTSC. This method involved production of HTSCs into a powder form The powder material was
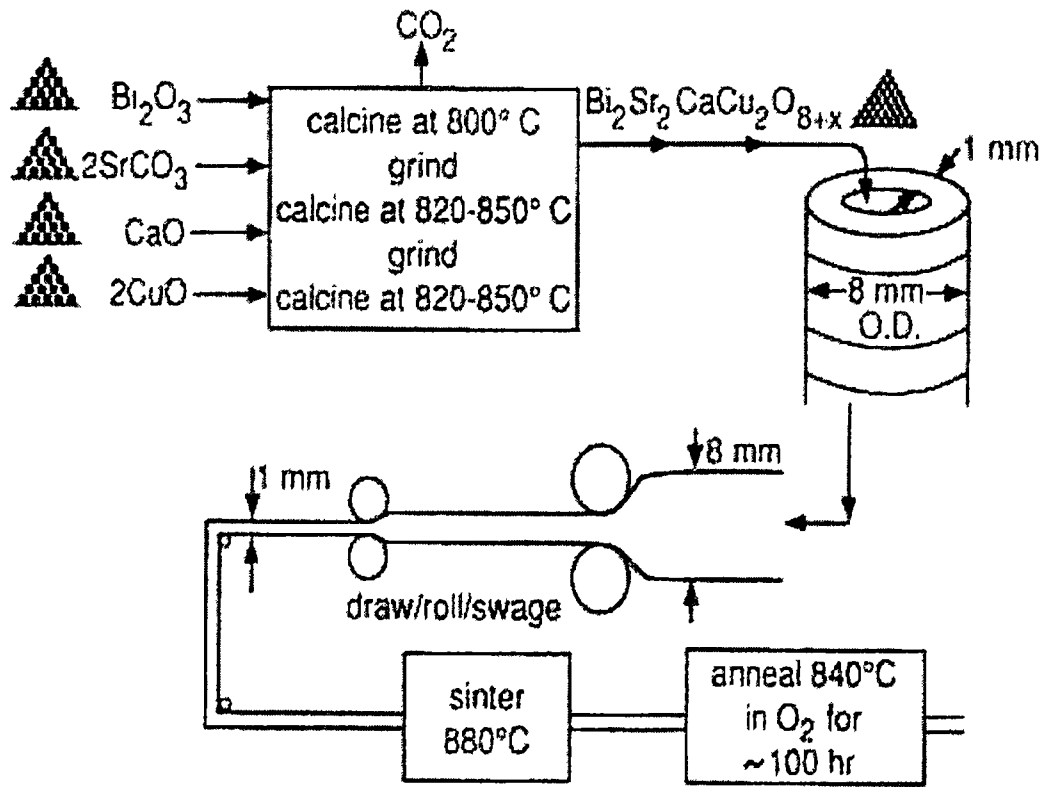
Figure 2.1 BSCCO Powder-In-Tube Wire Manufacture

Source: Sheahen, T.. Introduction to High-Temperature Superconductivity. New York:

Plenum Press, 1994

then packed inside hollow silver tubes. The tubes were drawn through an extruder into fine wire and then subsequently heat-treated to promote sintering.

Modern fabrication methods center on two competing methods, IBAD (Ion Beam Assisted Deposition) and RABiTS (Rolling Assisted Biaxially Textured Substrate) IBAD was developed by Los Alamos National in 1995 IBAD uses an ion gun aligned at a specific angle to promote deposition of oxide films in a preferred orientation. IBAD creates a template in this manner upon which HTSC materials can be grown. In 1996, Oak Ridge National Laboratory developed the RABiTS RABiTS also involves the generation of a template prior HTSC material deposition. However, RABiTS develops a template through the use of mechanical rolling and the use of thermal treatment to develop aligned, cubic-textured metal substrates. Both methods may also incorporate the deposition of buffer layers, or chemically inert layers, in-between the substrate and HTSC. Figure 2.2, page 9, illustrates an example HTSC wire architecture with the RABiTS scheme.

The development of these substrate technologies has offered a foundation upon which an outburst in different methods for the deposition and growth of both the HTSC and buffer layers. These methods vary for example from physical deposition: sputtering (magnetron and ion beam), electron beam, and plasma spray, to chemical methods: metal organic vapor deposition, electrophoresis, spray pyrolysis, and sol-gel. Table 2.1, page 10, shows a complete listing of published schemes for fabrication of HTSC films and wires. Of particular interest to this thesis is sol-gel techniques, a detailed explaination of this technique is presented later in this chapter.
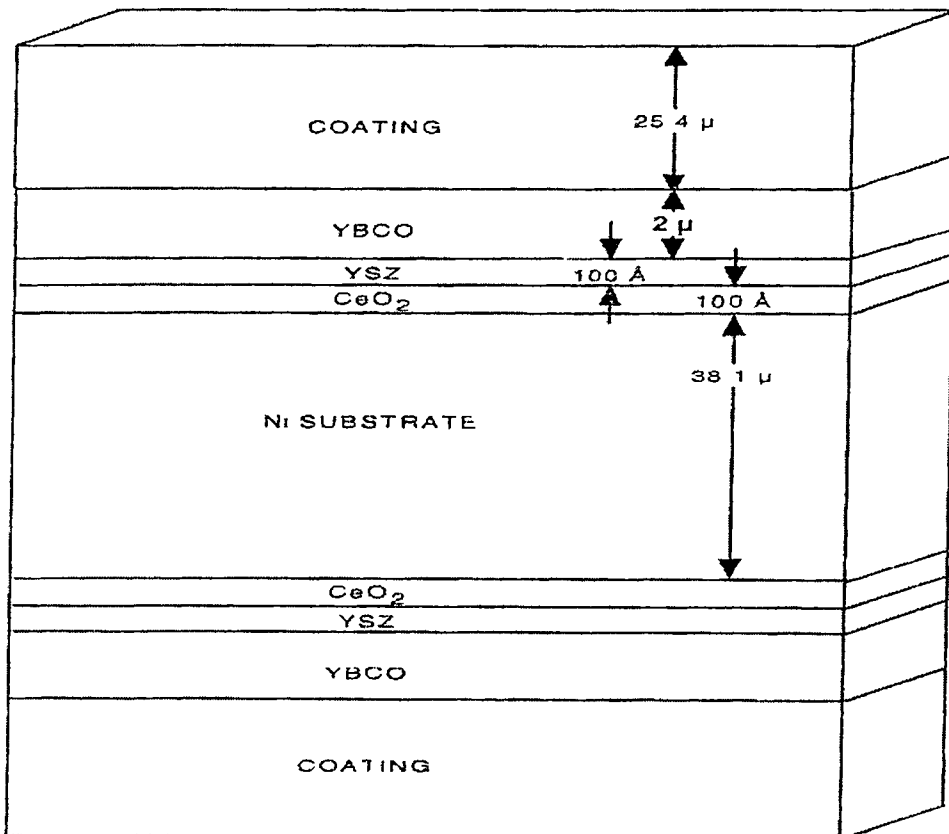
Figure 2.2 Possible RABiTS Architecture

The architecture shows the multilayering of substrate (Nickel), buffer layer (CeO$_2$/YSZ),

superconductor layer (YBCO), and insulation layer

Source: Chapman., J. Life Cycle Cost Study for Coated Conductor Manufacture by Metal

Organic Chemical Vapor Deposition. Tullahoma: University of Tennessee Space

Institute, July 1999

9

Table 2.1 List of Published Schemes for Fabricating HTSC Fabrication

Physical Methods	Chemical Methods
Sputter Deposition	Chemical Vapor Deposition (CVD)
-Magnetron Sputtering	-Metal Organic CVD (MOCVD)
-Ion Beam Sputtering	Sol-Gel
Electron Beam Evaporation	Metalorganic Decomposition (MOD)
Flash Evaporization	Electrodeposition
Plasma Spray	Aerosol/Spray Pyrolysis
Molecular Beam Epitaxy	Liquid Phase Epitaxy (LPE)
Laser Ablation	Powder Suspensions or Slurries related
	-Electrophoresis

Adapted from Lasrado, V. Bench Scale Evaluation of Solution-Growth Based Techniques

For Manufacturing HTS Wire/Tape. Master's Thesis. Knoxville: University of

Tennessee, December 1998.

The Nature of Superconductivity

The nature of superconductivity places a vital role in determining what are processing parameters used to produce an HTSC product. There a wide variety of models available which attempt to describe the nature of superconductivity in certain materials. For example, Bardeen, Cooper, and Schrieffer developed a widely accepted model (BCS), which is foundation for much of the contemporary theory about the superconductivity phenomenon. Central to this and subsequent models are several key concepts.

In conventional materials, electrons travel through a conductor individually. They collide with atoms and are scattered which dissipates energy. This energy loss to the surroundings is that associated with electrical resistance. In superconducting materials, electrons travel in pairs, called Cooper pairs. However, when pairs encounter atoms they will not scatter because the probability of both electrons undergoing the same scattering event is negligible. Instead, the Cooper pairs will split apart. There is a finite energy cost associated to this splitting. Thereby, Cooper pairs can continue through a network of lattices without generating electrical resistance until this energy cost is overcome and the pairs split.

In practical superconducting materials, many different grains are present and grain boundaries persist everywhere. Current flow is illustrated in figure 2.3, page 12. Grain boundaries are often referred to as weak links. Weak links are a barrier through which superconducting current must tunnel through. Strong weak links can effectively break up cooper pairs. The tunneling phenomenon is generally described in quantum
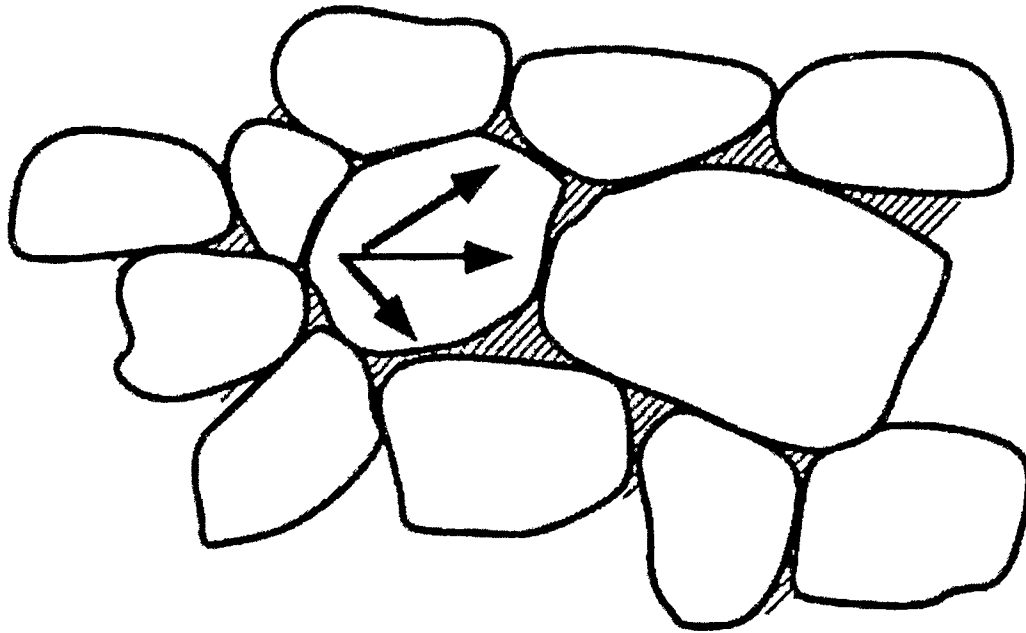
Figure 2.3 Superconducting Current Flow in Polycrystalline Material.

Note: Current can flow along many paths

Source: Sheahen, T. Introduction to High-Temperature Superconductivity. New York: Plenum Press, 1994.

mechanics terms utilizing the dual wave nature of particles. But for the sake of brevity and simplicity, this thesis will not describe this phenomenon, but only present ways in which weak links are being circumvented to increase current density.

There are three approaches to improving current density in HTSCs (Sheahen, 1994). The first approach is to have current flow through grains in the most favorable direction. (Sheahen, 1994). For YBCO, current flows more easily in the a and b directions of the lattice than in the c direction (Sheahen, 1994). Thereby, it is desirable to not have grains coupled together on the c-axis. This alignment of the grains can be accomplished with epitaxial thin film technologies like the previously mentioned RABiTS process. The second approach is to reduce the number of weak links in the direction of desired current flow (Sheahen, 1994). In other words, one wants to reduce the number of grain boundaries, impurities, and cracks in the current direction. Finally, the third approach is to decrease boundary thickness (Sheahen, 1994). This is often accomplished by careful control of the processing conditions to reduce the number of impurities and to manipulate grain size in the HTSC.

As mentioned previously, magnetic fields also limit superconductive current flow. This has importance for many applications including wire making. Tinkham performed experiments rotating c-axis aligned YBCO in the a-b plane (Tinkham, 1988). Figure 2.4, page 14, shows how J_c falls off with magnetic field orientation and strength. Typically with HTSC, when magnetic field is increased beyond a critical value (H_{c1}), small circular regions of material no longer become superconducting and are referred to as being in a vortex state. The density of vortex regions to superconducting regions is increased up to a second value (H_{c2}), where the entire material returns to a non-superconducting state.
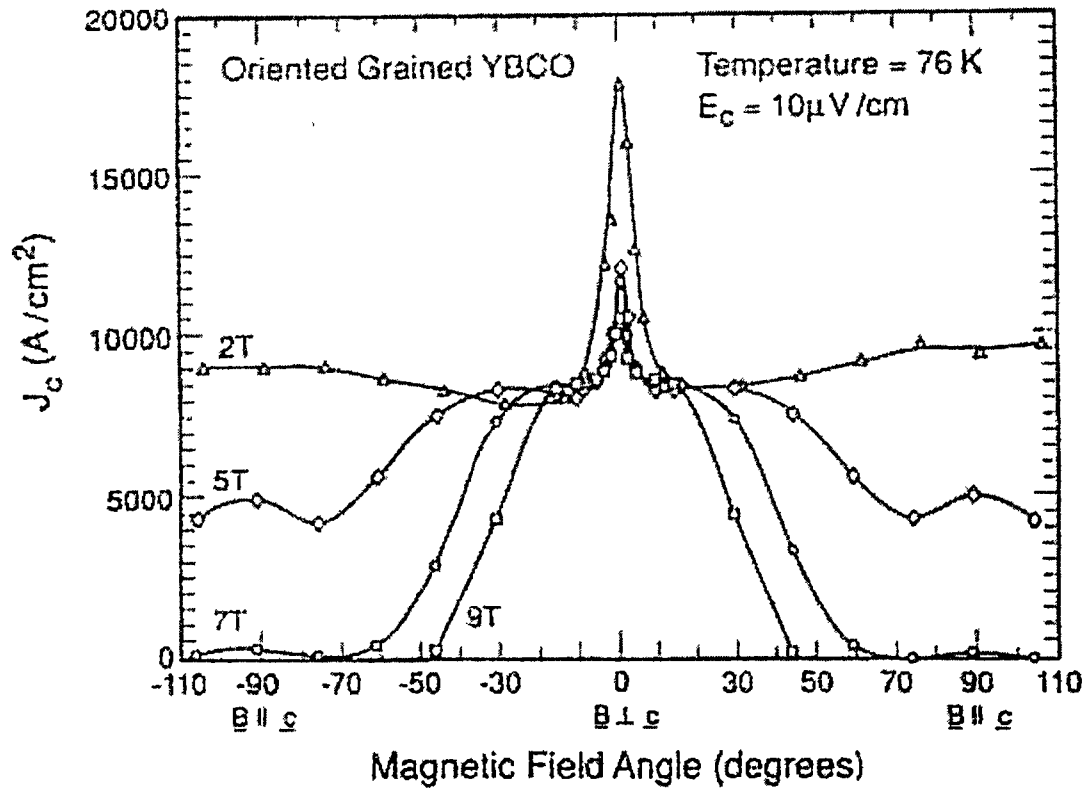
Figure 2.4 Transport Critical Current Density J_c as a Function of the Angle Between the

Magnetic Field and the a-b Plane for $YBa_2Cu_3O_7$.

Source: Sheahen, T. Introduction to High-Temperature Superconductivity. New York:

Plenum Press, 1994.

Superconducting current flows unimpeded in the sections surrounding a vortex region. However, the Lorentz force of nearby passing current can move the penetrating magnetic flux lines which in-turn generates an effective resistance (Sheahen, 1994).

Magnetic flux lines are pinned or stopped from moving by repulsion with other flux lines, by running into grain boundaries, and by running into impurities (Sheahen, 1994). Generally, multiple flux lines can be frozen or pinned around one barrier site because of natural repulsion forces. However, flux movement was also found to be initiated by thermal energies. This is know as flux creep. Yeshuran and Malozemoff proposed that at a value (H_{irr}, which lies between H_{c1} and H_{c2} and is a function of J_c and temperature) flux pinning is no longer possible (Yeshuran & Malozemoff, 1988). They coined the phrase "giant flux creep" for this event.

Together, magnetic field and crystal alignment limitations have a great impact on the properties of HTSCs. Thereby, creating the need to use specially processed HTSC materials for each individual application. Numerous tradeoffs, will need to be assessed to meet such specification demands. Knowledge of these basic superconductivity concepts will help in this decision process.

YBCO

YBCO or $Y_1Ba_2Cu_3O_7$ is the most commonly studied HTSC. The atomic lattice is presented in figure 2.5, page 16. As mentioned earlier, the superconducting current has greater density in the a-b directions (Sheahen, 1994). This is attributed to the copper oxide planes running in the a-b directions (Sheahen, 1994) Yttrium has been substituted
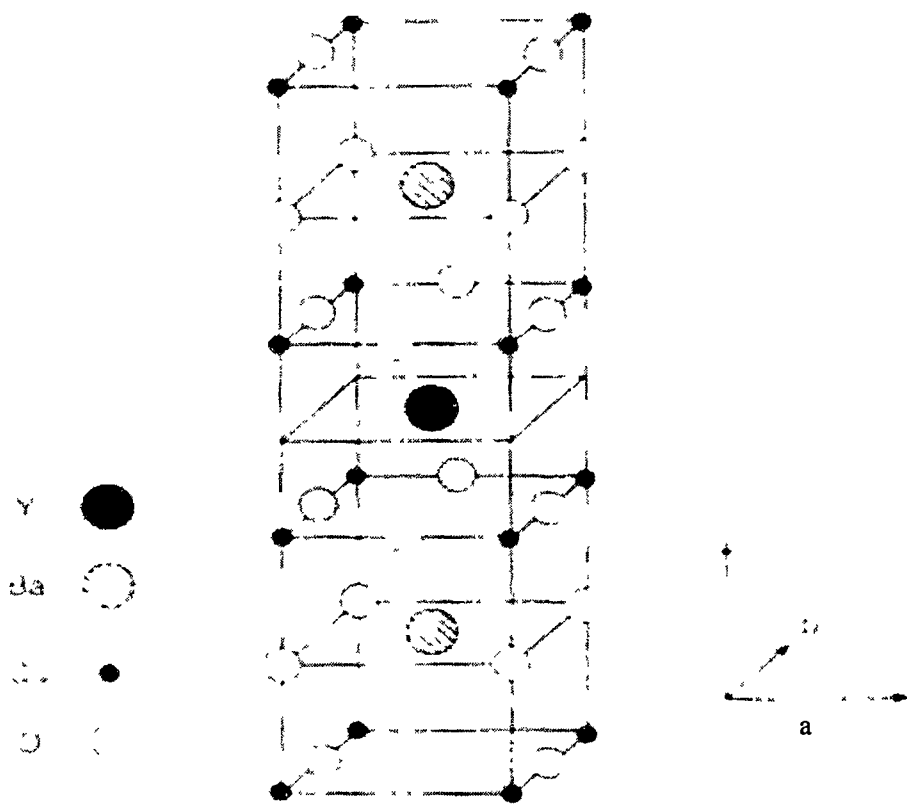
Figure 2.5 YBCO ($YBa_2Cu_3O_7$)

Note: The superconducting phase has two oxygen vacancies not shown

Source: Sheahen, T. Introduction to High-Temperature Superconductivity. New York:

Plenum Press, 1994.

with various other rare earth elements, but the T_c changes very little. Thus, Yttrium merely acts as a spacer and a charge carrier (Sheahen, 1994).

Formation of epitaxial YBCO from solution or powder methods involves a complicated time and temperature post-anneal program. Figure 2.6, page 18, is an example of a time and temperature program developed by the ORNL. Post anneals require special atmospheres of O_2 to help regulate the formation of YBCO with the correct oxygen stoichiometry to form the 1-2-3 phase. Common problems associated with processing are the additional formation of unwanted phases like barium cuprate and 2-1-1 YBCO Continual changes in precursor solution chemistry are helping to eliminate the formation of some of these phases. For instance, ORNL is also developing an all-iodide approach, which avoids the formation of $BaCO_3$ (ORNL Annual Report, 1998)

Current conduction under magnetic fields in YBCO generally fairs better than in other HTSCs like BSCCO (Bismuth Strontium Calcium Copper Oxide) (Sheahen, 1994). Flux pinning in YBCO is commonly accomplished by oxygen vacancies in the lattice (Chudnovsky, 1990). In addition, Kwok, at Argonne National Laboratory, demonstrated the intrinsic flux pinning properties of YBCO's copper oxide planes when magnetic fields were precisely aligned (Kwok, 1991). However, a condition know as lattice flux melting occurs in YBCO when both the magnetic field and the current do not lie in the a-b planes (Sheahen, 1994). During lattice flux melting, vacancies or barriers are no longer able to pin multiple lines. In other words, the flux lines no longer are able to be frozen together in a traffic jam at the pinning sites. This practically destroys the current carrying properties of YBCO (Sheahen, 1994). Lattice flux melting is a function of temperature and magnetic field strength.
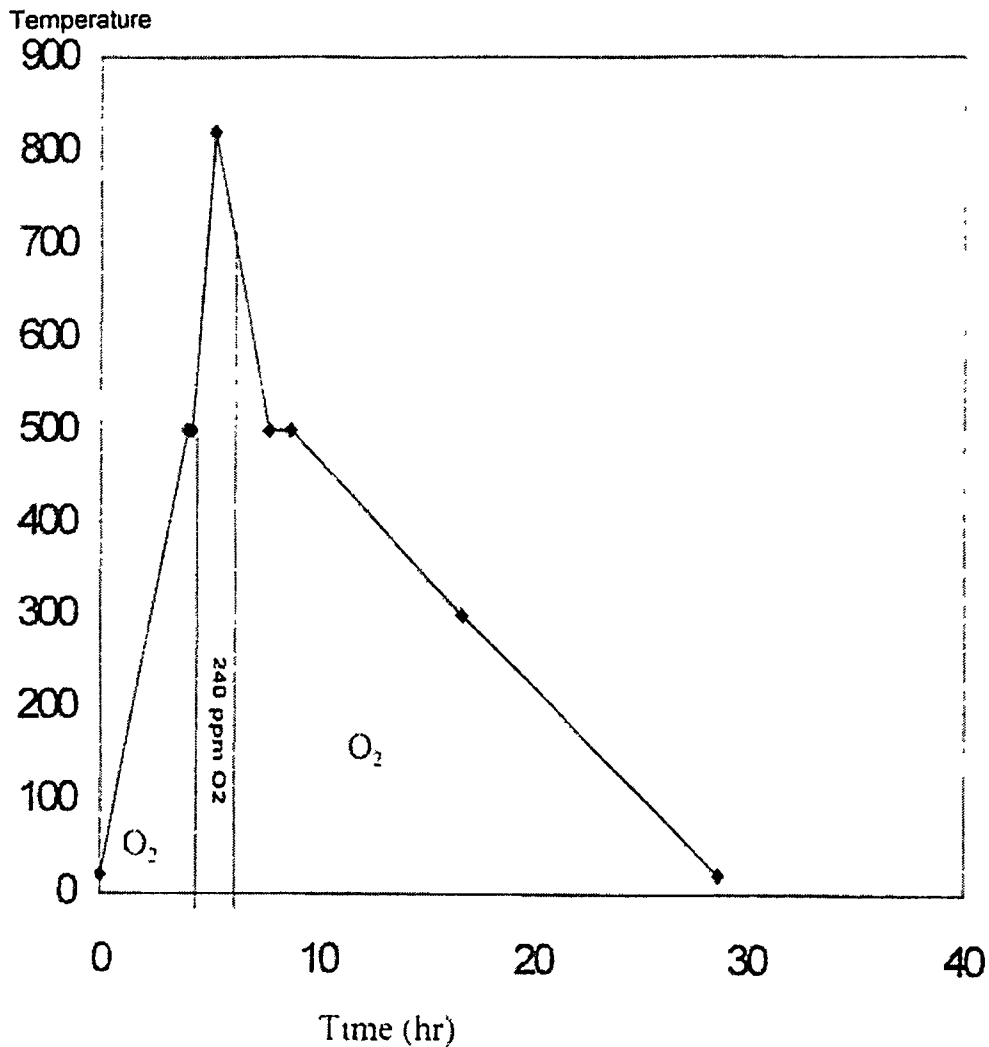
Figure 2.6 Time and Temperature Program for the Processing of YBCO

Note· This diagram also shows the necessary changes in processing atmosphere

Source: Lasrado, V. Bench Scale Evaluation of Solution-Growth Based Techniques For Manufacturing HTS Wire/Tape. Master's Thesis. Knoxville: University of Tennessee, December 1998.

RABiTS Nickel Substrates

RABiTS nickel could be produced by the following steps. First, high purity nickel (>99.99%) is consecutively rolled in a series of deformations which total over 90%. Then, the nickel is recrystalized by annealing at temperatures of 700°C or more for several hours at oxygen pressures of less than 10^{-6} torr. Annealing has been found to develop a sharp cubic texture in the Ni (ORNL Annual Report, 1998). Figure 2.7, page 20, shows the sharpening of Ni textures with pole figures by annealing. Also of consequence, stable nickel oxide is formed at a temperature of 700°C with an oxygen partial pressure greater than 10^{-13} torr (ORNL Annual Report, 1998). Consequently, a forming gas atmosphere (4% hydrogen in argon) is used because the hydrogen reacts with the oxygen at the nickel's surface to form water instead of nickel oxide (ORNL Annual Report, 1998).

RABiTS Buffer Layers

Buffer layers in the RABiTS scheme act to form chemical barrier between the nickel backbone and the superconducting layer The criteria for determining buffer layer applicability has been addressed by M. Paranthaman of ORNL (Lasrado, 1998). A good buffer layer should be: smooth and continuous, biaxially aligned, low thermal expansion coefficient mismatch with substrate and HTSC, chemically stable up to 780°C in low partial pressures of O_2, and low lattice mismatch with HTSC (Lasrado, 1998).

19

(a) (b)

RD

(c) (d)

(111) (200)
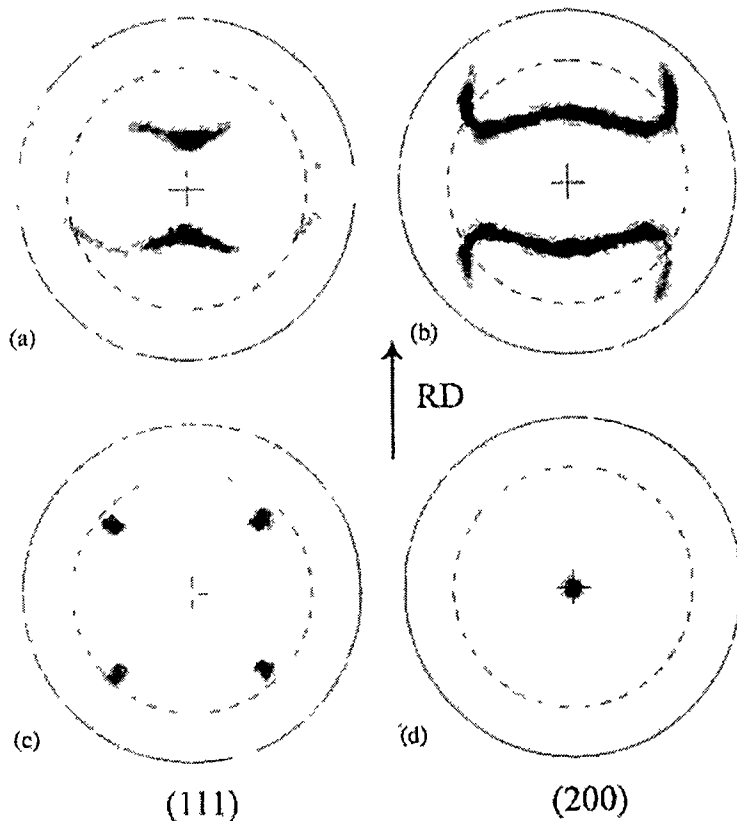
Figure 2.7 Improvement in Texture with Recrystallization

(a and b) (111) and (200) x-ray pole figures showing a copper-type texture in 99.99% Ni

sheet after rolling to >90% reduction. (c and d) (111) and (200) x-ray pole figures for the

same sheet after recrystallization at 1000°C for 4 hr showing the development of a strong

cube texture.

Note: RD refers to rolling direction.

Source: Simon, C. Experimental Study of the Effects of Annealing Time, Equilibrium

Angle, and Absolute Misorientation Angle on Thermal Grain-Boundary Grooving in

Cube-Textured Nickel Master's Thesis. Knoxville: University of Tennessee, 1999.

The most commonly used buffer layer architecture for RABiTS is that of YSZ/CeO$_2$/Ni J$_c$s of 3 MA/cm^2 have been reported by ORNL using PLD (pulsed laser deposition) of YBCO on this architecture (ORNL Annual Report, 1998). Commonly used materials for buffer layers deposited by the sol-gel route are rare earth aluminates and gallates. For instance, lanthanum aluminate and neodymium aluminate have been successfully deposited epitaxially on textured Ni substrates at ORNL (ORNL Annual Report, 1998). YBCO films with J$_c$s of 1 M A/cm^2 have been demonstrated on LaAlO$_3$ and NdAlO$_3$ buffered strontium titanate (SrTiO$_3$), single crystals (ORNL Annual Report, 1998).

X-ray Diffraction

X-ray diffraction (XRD) is a common method of nondestructive composition analysis of solid materials. X-rays are also capable of showing how crystals are arranged in a material. Thereby, they are able to tell researchers about the texture and the degree of epitaxy in the materials being investigated.

XRD machines generate x-rays by accelerating electrons against a target metal, copper for instance. High voltages accomplish this acceleration. As electrons bombard the target metal they knock out electrons in the target metal's shells (k shell in the case of copper). Electrons from the outer shells drop down into this shell and emit x-rays in the process. The wavelength of the x-rays is characteristic of the target metal's electronic configuration and the shell from which the electron drops down.

For instance, if an electron drops down from the L shell to the K shell then this is referred to as K_α x-rays. It is also possible, but to a lesser degree, for electrons further out in the M shell to drop into the vacancy. The K_β refers to these x-rays In contemporary XRD machines, a monochromatic device is used to filter out most of the K_β rays. However, the practical filtering of all K_β signals is not possible. Thereby, especially strong diffraction signals of K_α usually have corresponding small K_β signals along with them.

The diffraction phenomenon of x-rays is defined as follows. "A diffracted beam may be defined as a beam composed of a large number of scattered rays mutually reinforcing one another" (Cullity, 1978). Figure 2.8, page 23, depicts the diffraction of x-rays in an atomic lattice. In essence, x-rays can be scattered in many directions, but only at certain diffraction angles, denoted by 2θ, does the scattering x-rays mutually reinforce each other to produce discernable signals. Bragg's law exactly describes this phenomenon as follows:

$$\lambda \equiv 2d \sin \theta_B ,$$

where d is the distance of atomic spacing and θ_B is referred to as Bragg's Angle

It is important to note, that in real conditions, signals of lesser intensity are also produced close to the diffraction angles suggested by Bragg's law. This is due to slight misorientation in polycrystalline materials and varying trajectories in incident x-rays (Cullity, 1978). Because of this effect, diffraction patterns take on a bell shaped curve as
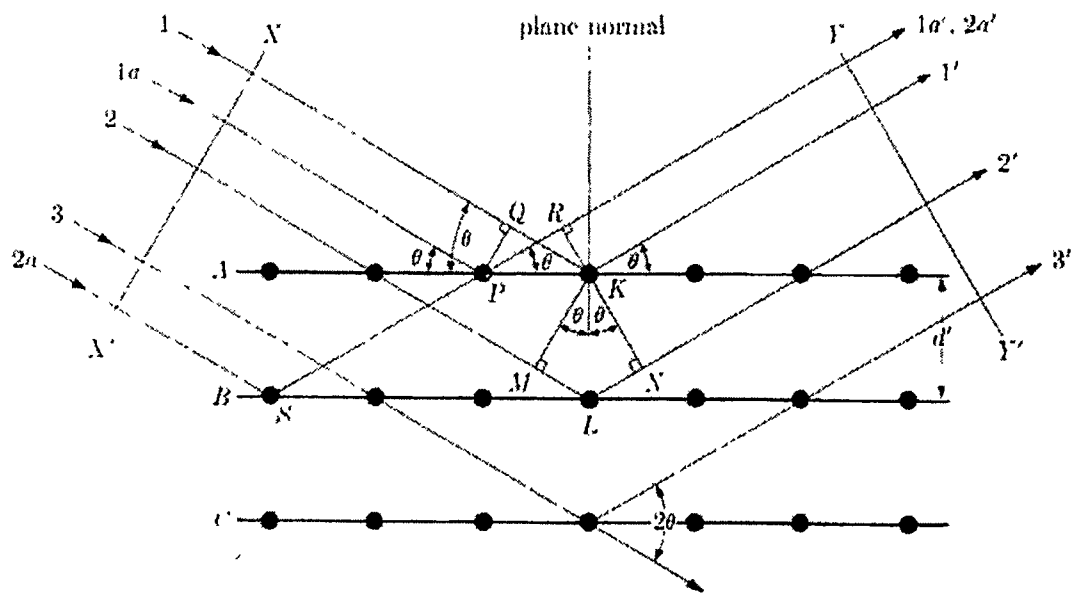
Figure 2.8 Diffraction of X-rays by Atomic Lattice

Adapted from Cullity, B. Elements of X-ray Diffraction. Reading: Addison-Wesley,

1978.

shown in Figure 2.9, page 25. The full width at half maximum (FWHM) of the diffraction peak is commonly used to characterize the degree of misorientation in polycrystalline materials. The smaller the number, the greater the degree of alignment or the more closely the material resembles a single crystal.

Sol-Gel Processing

"A sol is a colloidal suspension of solid particles in a liquid" (Brinker & Scherer, 1990). A gel is a substance where one molecule reaches macroscopic dimensions and extends throughout the solution (Brinker & Scherer, 1990). Sol-gel is in essence the transformation of small, suspended molecules (sol) into a few large molecules that persist throughout the liquid like a skeletal structure (gel). A basic overview of sol-gel processing of ceramic thin-films is as follows. Precursors or starting materials (metal salts or metals/metalloids with organic ligands) in the forms of sols are coated onto a substrate. The solvent rapidly evaporates off and the precursors transform into an amorphous gelatin state. This gel is then heat treated to promote crystallization into a structured, thin-film, ceramic form.

At the heart of sol-gel chemistry is the reactions that transforms small colloidal particles into a massive skeletal-structured gel. This thesis will primarily concern itself with chemistry associated with metal alkoxides, since most superconductor/buffer layer precursors are of this nature. Metal alkoxides are metal or metalloid elements with alkyl

24
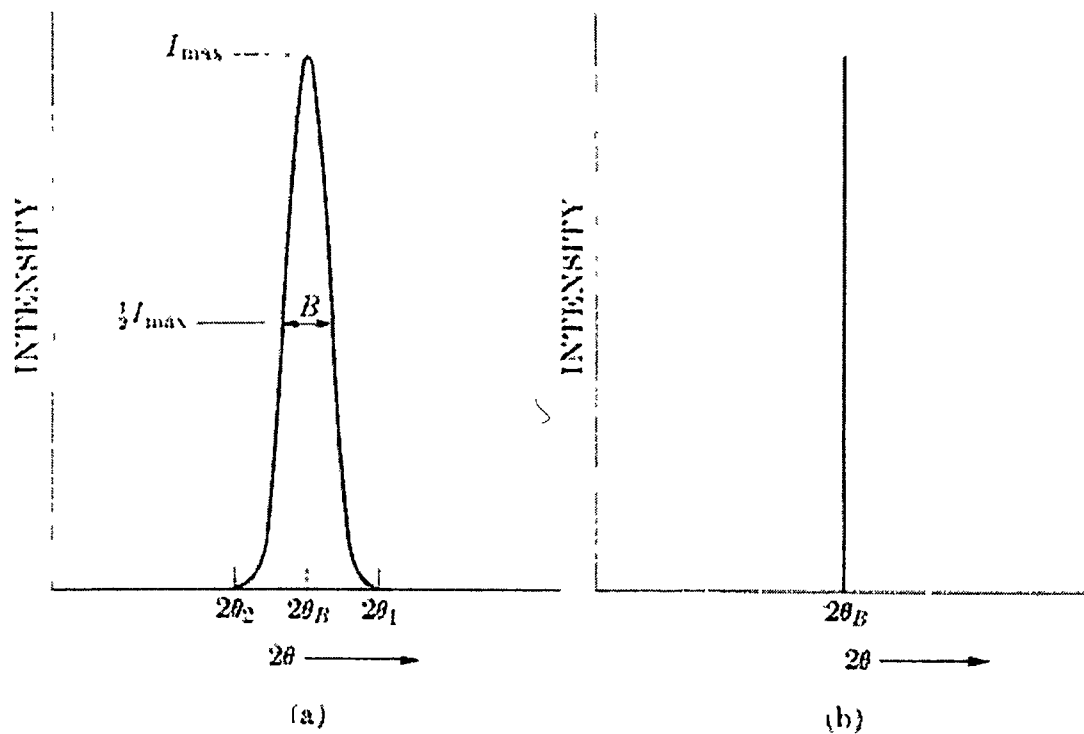
Figure 2 9 Diffraction Lines

(a) Real diffraction pattern illustrating the effect of slight deviations from the Brag angle.

(b) An ideal diffraction pattern where diffraction occurs only at the Brag angle.

Adapted from Cullity, B. Elements of X-ray Diffraction. Reading: Addison-Wesley, 1978.

ligands. They are often represented as $M(OR)_z$, where R is an alkyl group and M is the metal atom. Metal alkoxides have two distinct reactions in sol-gel chemistry. These are the hydrolysis and the condensation reactions.

In simple hydrolysis reactions, water molecules solvate a metal cation and form three types of ligands: aquo {$M-(OH_2)$}, hydroxo {M-OH}, or oxo {M=O}. The type of ligand that forms depends on the magnitude of charge transfer from H_2O to M (e.g., oxo would occur at highest magnitude). For coordinately saturated metals (e.g. metal alkoxides), hydrolysis involves the following reaction steps: nucleophilic addition, proton transfer, and a departure of a leaving group. Figure 2.10, page 27, illustrates a typical hydrolysis reaction.

Condensation reactions occur between hydrolyzed molecules and other hydrolyzed or unhydrolyzed molecules. Condensation reactions occur following a mechanism similar to hydrolysis reactions, which is nucleophilic addition, proton transfer, and leaving group removal. The two common types of condensation reactions are shown in figure 2 11, page 28.

More complex condensation reactions can occur between different, partially hydrolyzed metal alkoxides. These reactions require special considerations such as the matching of the rates of hydrolysis between the differing metal alkoxides to promote condensation between them (Brinker & Scherer, 1990). For instance, annual reports from ORNL have stated that the use of a bidentate or bifunctional 2-methoxyethoxy ligands promote the formation of mixed metal sols (ORNL Annual Report, 1996). ORNL's annual reports also suggests that through 2-methoxyethoxy ligands, the hydrolysis and

$$H-\underset{\underset{\displaystyle H}{|}}{O} + M-OR \quad \longrightarrow \quad \underset{\displaystyle H}{\overset{\displaystyle H}{\diagdown}} O: \rightarrow M-OR \quad \longrightarrow \quad HO-M \leftarrow O \overset{\overset{\displaystyle R}{\diagup}}{\underset{\underset{\displaystyle H}{\diagdown}}{}}$$

$$\text{(a)} \qquad\qquad \text{(b)} \qquad\qquad \text{(c)}$$

$$\longrightarrow \quad M-OH + ROH$$

$$\text{(d)}$$
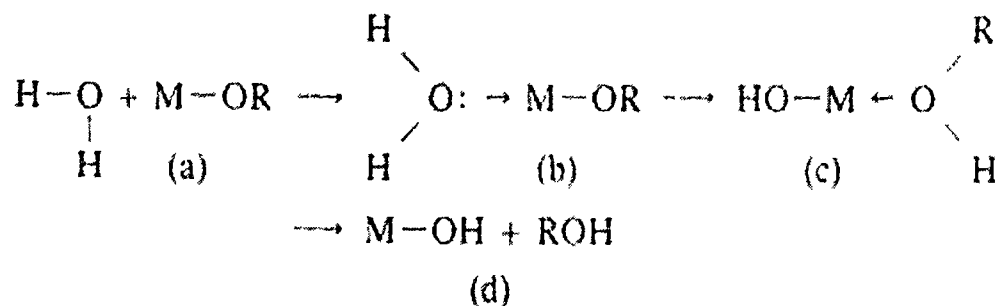
Figure 2.10 Metal Alkoxide Hydrolysis Reaction

(a-b) Nucleophilic addition of water.

(c-d) Hydrogen transfer from attached water molecule to ligand followed by the subsequent removal of the ligand as an alcohol.

Adapted from Brinker, C. & Scherer, G. Sol-Gel Science. New York: Academic Press, 1990.

27

$$M-\underset{\underset{H}{|}}{O} + M-OR \longrightarrow M-\underset{\underset{H}{\diagdown}}{O:} \rightarrow M-OR \longrightarrow M-O-M \leftarrow O\underset{\underset{H}{\diagdown}}{\overset{\diagup R}{}}$$

$$\longrightarrow M-O-M + ROH$$

(a)

$$M-\underset{\underset{H}{|}}{O} + M-OH \longrightarrow M-\underset{\underset{H}{\diagdown}}{O:} \rightarrow M-OH \longrightarrow M-O-M \leftarrow :O\underset{\underset{H}{\diagdown}}{\overset{\diagup H}{}}$$

$$\longrightarrow M-O-M + H_2O.$$
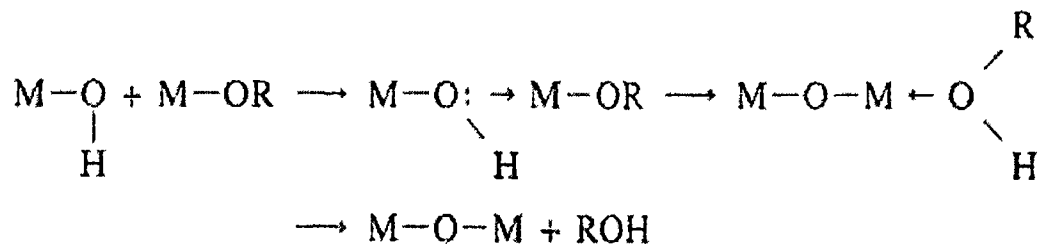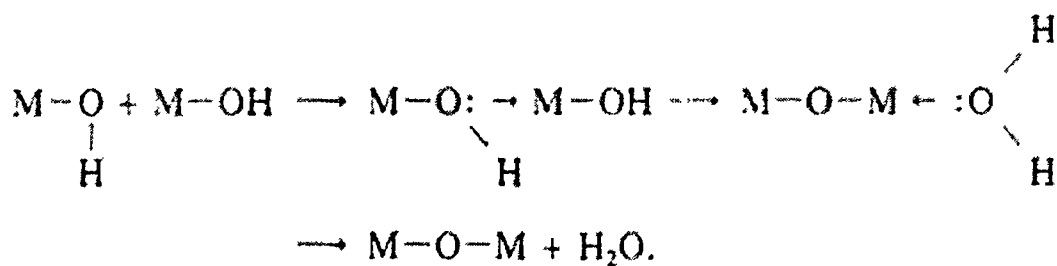
(b)

Figure 2 11 Metal Alkoxide Condensation Reactions

(a) Alcoxolation reaction, where an alcohol is the leaving group.

(b) Oxolation reaction, where a water molecule is the leaving group.

Adapted from Brinker, C. & Scherer, G. Sol-Gel Science. New York: Academic Press, 1990.

condensation rates can be controlled to diminish the formation of precipitates (ORNL Annual Report, 1996).

Transformation of sol to gel occurs by continual hydrolysis and condensation reactions in combination with the evaporation of solvent until a large molecular skeleton forms. The final structures of gels can be described as either a fractal-agglomeration of monodisperse particles or a network of polymeric chains that may be cross-linked to some degree. The structure that will be produced depends on many factors including: the molecular complexity of precursor, the solvent used, the temperature, presence of other anions, the rate of condensation, the rate of hydrolysis, and the rate of solvent removal.

Dip Coating

Figure 2.12, page 30, shows the various stages in the dip coating process. Basically in the dip coating process, liquid is entrained by the moving substrate. Some of the liquid is returned to the solution in drainage, while the other part dries onto the substrate. As the entrained liquid evaporates on the substrate, then the sols are brought into closer contact with one another. This allows further condensation reactions and eventually gelation results. The resulting gel is continually compacted by evaporation and subsequently increasing capillary pressures. This shrinkage causes continual condensation reactions and a stiffening of the gel. The stiffened gel then becomes mechanically anchored on the substrate. Figure 2.13, page 31, shows an illustration of gel formation during dip coating. The thickness of the films formed is governed by up to six forces: viscous drag on the moving substrate, force of gravity, surface tension in the
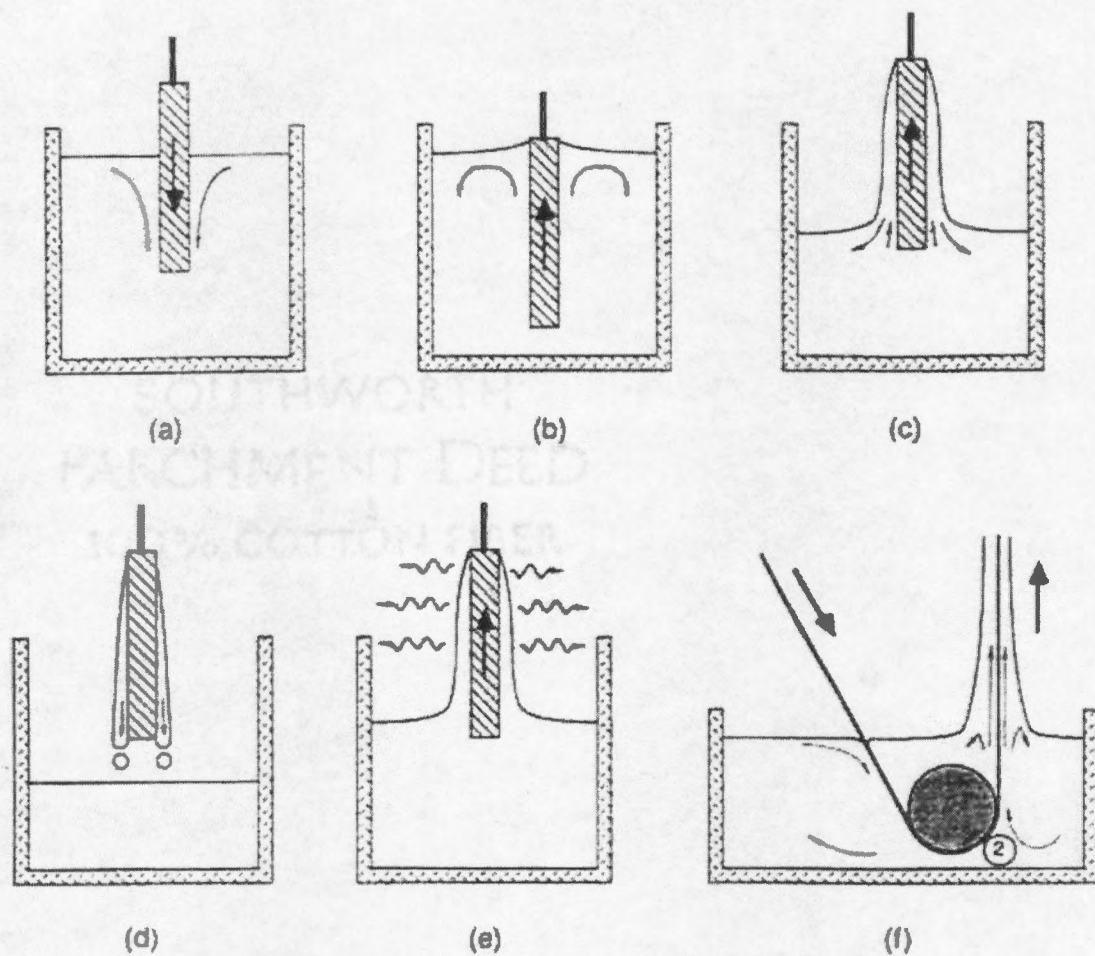
Figure 2.12 The Dip Coating Process

(a)Immersion (b) Start-up (c) Deposition & Drainage (d) Drainage (e) Evaporation

(f) A continuous system.

Adapted from Brinker, C. & Scherer, G. Sol-Gel Science. New York: Academic Press, 1990.
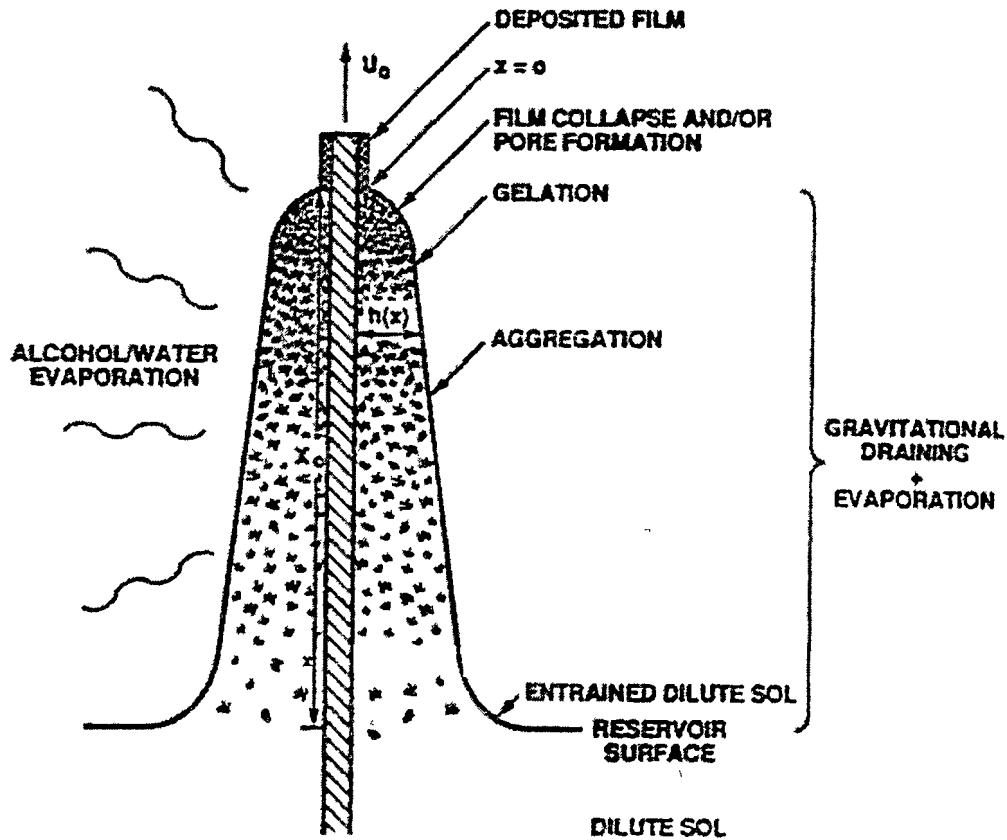
Figure 2.13 Gel Formation in Dip Coating

Schematic of the steady state sol-gel dip coating process, showing the sequential stages of

structural development that result from draining accompanied by solvent evaporation and

continued condensation reactions.

Adapted from Brinker, C. & Scherer, G. Sol-Gel Science. New York: Academic Press,

1990.

meniscus region, inertial force of boundary layer liquid arriving at the deposition region, surface tension gradient, and disjoining or conjoining pressure (Brinker & Scherer, 1990).

The dip coating process can uniquely effect the morphology of the gel films. The rate of withdrawal of the substrate can promote a competition between the evaporation and condensation rates. This competition can effect the structure of the gels. In weakly branched sols, such as polymeric chains with a low degree of cross-linking, it has been observed that films had no discernable porosity when the withdrawal rate was increased (Brinker & Scherer, 1990). This has been explained by the hypothesis that the limited condensation reactions that occur during film formation allowed the weakly linked polymers to interpenetrate each other and to remain compliant, which allows even further densification through collapse from capillary pressures (Brinker & Scherer, 1990). In highly branched sols, for greater chain lengths, the observed porosity is higher (Brinker & Scherer, 1990). This can be attributed to the stiffness of the network and ability to resist collapse (Brinker & Scherer, 1990).

Experimental Design

Experimental design characterizes the type of effect an input factor has on a response. Figure 2.14, page 33, shows the four possible effects that a factor can have on a response. Experimental design can distinguish and account for individual effects and interaction effects of multiple factors that are varied throughout an experiment. This is accomplished through specially designed and coded experimental matrices like the two level design shown in Table 2.2, page 34. Two level refers to the two settings (high and

Factor A shifts the average.
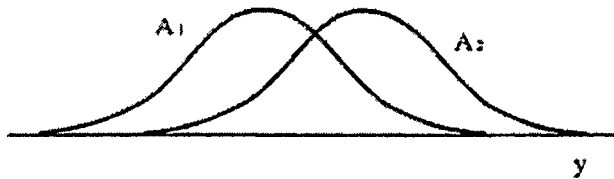
Factor B shifts the standard deviation.
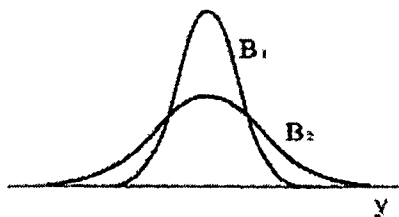
Factor C shifts both the average and the standard deviation.
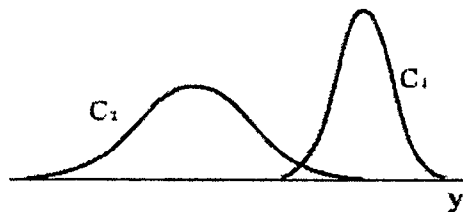
Factor D has no affect on the average or the standard deviation.
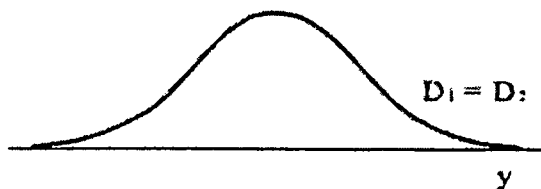
Figure 2.14 Possible Influences of Input Factors on a Response

Adapted from Schmidt, S. & Launsby, R. Understanding Industrial Designed Experiments Colorado Springs: Air Academy Press, 1998.

Table 2.2 Arbitrary Two Level Coded Experimental Design Matrix

Factor Row #	A	B	C	D	E	F	G
1	-1	-1	-1	-1	-1	-1	-1
2	-1	-1	-1	-1	-1	1	1
3	-1	-1	1	1	1	-1	-1
4	-1	1	-1	1	1	-1	1
5	-1	1	1	-1	1	1	-1
6	-1	1	1	1	-1	1	1
7	1	-1	1	1	-1	-1	1
8	1	-1	1	-1	1	1	1
9	1	-1	-1	1	1	1	-1
10	1	1	1	-1	-1	-1	-1
11	1	1	-1	1	-1	1	-1
12	1	1	-1	-1	1	-1	1

Note: The low settings of each factor are represented by (-1) and the high setting of each

factor is represented by (1)

low) for the input factors. Common types of experimental design include full factorial, Box-Behnken, Plackett-Burman, and Taguchi designs.

Of interest in the design of such matrices is the orthogonality of the matrix. An orthogonal matrix for a 2-level design can be defined as one in which the sum of all the coded values in the vertical columns equals zero and the dot product of all the possible column pairs equals zero (Schmidt & Launsby, 1998). Matrices, which lack orthogonality, are characterized by an aliasing (or equating) of factors with one another, which thereby leads to the masking of the individual effects of each factor (Schmidt & Launsby, 1998). Also, matrices that are nonorthogonal suffer from multicollinearity. Multicollinearity can cause a variable with known positive effect to show a negative effect based analysis of nonorthogonal matrices (Schmidt & Launsby, 1998).

The effects and significance of factors and interactions in an experimental design can be determined through graphical plots, through regression modeling, and through analysis of variance (ANOVA). Graphical analysis involves a strategy of "picking the winner" from plots or charts. For example, a Pareto chart plots a comparison of the magnitude of effect on the response for each factor or interaction. This in turn can be used to select the most important factor by qualitative or visual means.

In regression modeling analysis, the objective is to develop a mathematical model that adequately predicts the behavior of both data collected and future data. The form of the mathematical model is determined forehand by the experimenter. The mathematical form includes constants, which are fit to data by the method of least squares. For instance, a linear regression model would be of the form $y = ax + b$.

ANOVA builds upon the concept of regression modeling. ANOVA develops models by partitioning the difference between the observed value and the mean of observed values into two segments by inserting a regression model. Figure 2.15, page 37, illustrates graphically this partitioning. The regression model is then optimized by making the variance in observed points (y) around the regression model points ($\hat{y}$), much less than the variance in observed data around it's arithmetic mean ($\bar{y}$). This is accomplished by first calculating the variance of the observed data around its mean variance (S_y^2).

$$S_y^2 \equiv \frac{\sum_{i=1}^{n}(y_i - \bar{y}_i)^2}{n-1} \equiv \frac{SST}{n-1}, \text{ where SST stands for sums squares total and n is the sample}$$

$$\text{size and,}$$

$$SST \equiv \sum_{i=1}^{n}(y_i - \bar{y})^2 \equiv \sum_{i=1}^{n}(y_i - \hat{y}_i)^2 + \sum_{i=1}^{n}(y_i - \hat{y})^2 \equiv SSE + SSR, \text{ where SSR stands for sum}$$

$$\text{squares regression and SSE stands for sum squares error}$$

Next the mean square error (MSE) or measure of variance of observed data around the regression model is calculated.

$$MSE \equiv \frac{\sum_{i=1}^{n}(y_i - \hat{y}_i)^2}{n-2} \equiv \frac{SSE}{n-2}$$
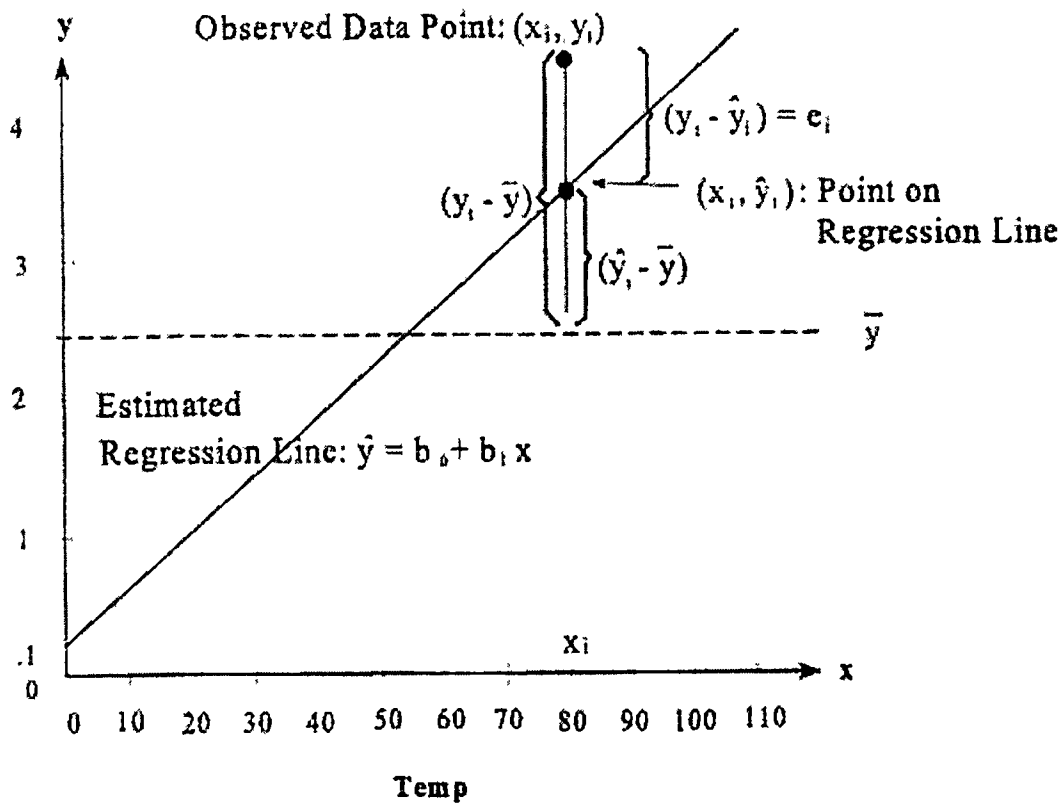
Figure 2.15 Partitioning in Regression Modeling

Source: Schmidt, S. & Launsby, R. <u>Understanding Industrial Designed Experiments</u>.

Colorado Springs: Air Academy Press, 1998.

The regression model is then optimized by making the MSE much smaller then the S_y^2. The strength of the regression model is determined by the R^2 (correlation coefficient) value, where

$$R^2 \equiv 1 - \frac{SSE}{SST}$$

Figure 2.16, page 39, shows the graphical interpretation of the meaning of high and low R^2 values for regression models. For example, an R^2 value of 0.5 indicates that 50% of the variability in y is explained through the regression model's relation with x and 50% of the data is noise or unaccounted variation.

Regression coefficients can be checked for significance by P-values. For regression coefficients the P-value represents the probability that a regression coefficient is significant. The P-value is often performed as a two-tailed test, and thus denoted P(2 tail). A two-tail test statistically tests a null hypothesis (H_o) with an alternative hypothesis (H_1) as such:

$$H_o \cdot \mu_{(+)} = \mu_{(-)}$$

$$H_1 \cdot \mu_{(+)} \neq \mu_{(-)}$$

For instance the null hypothesis could be that a factor is significant. Consequently, the alternative hypothesis would be that the regression coefficient is not significant. The errors associated in testing such a hypothesis are listed in Table 2.3, page 40. Type I errors in this example represent the error involved in assuming that a

38
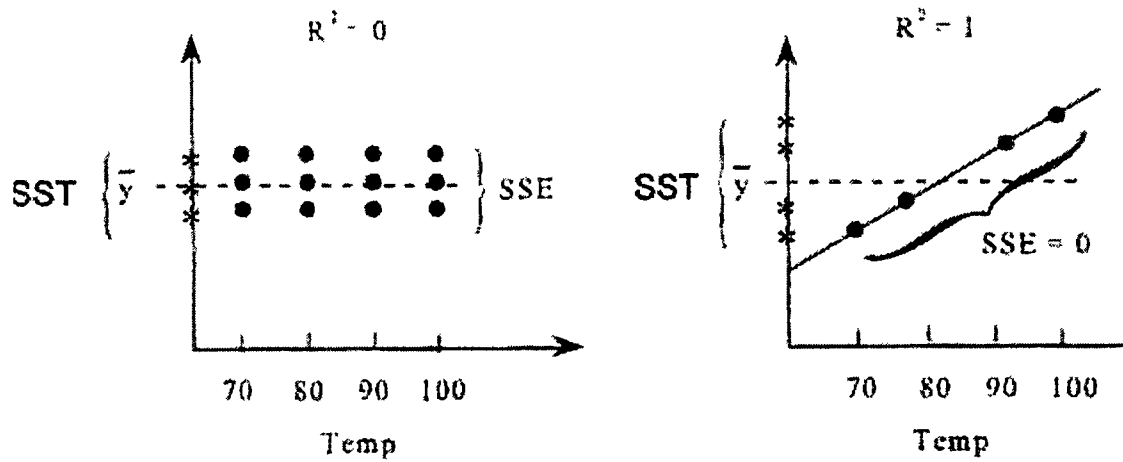
Figure 2.16 Graphical Representation of the Correlation Coefficient (R^2).

Source: Schmidt, S. & Launsby, R Understanding Industrial Designed Experiments.

Colorado Springs, Air Academy Press, 1998.

Table 2.3 Type I or II Error Occurs if Conclusion is Not Correct

		True State of Nature	
		H_o	H_1
Conclusion Drawn	H_o	Conclusion is correct	Conclusion Results in Type II Error
	H_1	Conclusion Results in Type I Error	Conclusion is Correct

Adapted from Schmidt, S. and Launsby, R. Understanding Industrial Designed

Experiments. Air Academy Press: Colorado Springs, CO. 1998

coefficient was significant when it was truly not significant. Type II errors, on the other hand, represent the error is assuming that the factor was not significant when it was truly significant. A P(2 tail) represents an estimate of the probability of making a type I error. As a rule of thumb, P(2 tail)<0.05 indicates significant factor, while 0.05< P(2 tail) < 0.10 is a gray area in which the factor is usually considered significant (Schmidt & Launsby, 1998). Type II errors are fixed by degrees of freedom and sample size.

ANOVA can also check the overall significance of the regression model with a F-test. First a F value is determined from the mean squares regression and mean squares error, as

$$F \equiv \frac{MSR}{MSE}$$

Then this value is compared to a critical F value ($F_\alpha(1, n-2)$). As a rule of thumb suggested by Schmidt and Launsby for Taguchi L12 matrix with less than 8 factors and 4 repetitions, an F-value greater than 6.0 suggests that the postulated model accounts for a significant amount of variation in the response (1998). While F < 4.0 suggests no relation of variation in response with model and 4.0<F<6.0 is a gray area which is left to the experimenter's decision (Schmidt & Launsby, 1998)

Optical Profilometry

Optical profilometry employs two different modes to scan smooth and rough surfaces. These modes are phase-shifting interferometry (PSI) and vertical scanning interferometry (VSI). PSI is used to measure very smooth or polished surfaces. In PSI, a

white-light beam is passed through an interferometer. The interferometer splits the beam into two halves. One half of the beam is directed towards the sample's surface. The other half of the beam is directed to a reference surface. The two beams are then recombined after reflecting off each respective surface. This recombination forms a pattern known as interference fringes, which appears as alternating light and dark bands on a monitor. The point at which the fringe's contrast is the highest corresponds to the optimum focus. After the beam is focused then a measurement is made. In PSI, this is accomplished by small, known amount of adjustments in the position of the reference surface. This causes a shift in the frequency of the reference beam and the system records the intensity of the resulting interference pattern at many different phase shifts. The height, h(x,y), can then be extracted from the following equation:

$$h(x,y) \equiv \frac{\lambda}{4\pi}\phi(x,y)$$ *,Where λ is the wavelength of the source beam, $\phi(x,y)$ is the phase*

data or integrated intensity data

The VSI mode differs from PSI in that it measures the fringe contrast or modulation instead of the phase of the interference fringes In VSI, the sample is translated into and out of focus by a translation device. An intensity signal is then recorded at each point on the surface. An algorithm is then used to calculate the surface heights from the fringe contrast or modulation data. This algorithm involves removal of low-frequency components, rectification by square-law detection, low-pass filtering, and curve-fitting interpolation to determine the exact vertical height at which the peak was produced.

CHAPTER 3

EXPERIMENTAL PROCEDURES

Lanthanum Aluminate Precursor Preparation

The preparation method of $LaAlO_3$ was based on the method used by Vineet Lasrado (1998). Inside an argon-filled, dry glove box, lanthanum isopropoxide was first added to a single-necked, round-bottomed, 300ml flask and weighed. Next, an equimolar amount of aluminum sec-butoxide was added to the flask. Then 150ml of 2-methoxyethanol was added and the mixture was stirred. Then the flask was closed with a glass stopper.

Meanwhile, a glass still was being prepared. Figure 3.1, page 44, diagrams the still used. First, the still was vacuum pumped for a minute and then back-filled with Argon. After the pressure built up, the still was re-vacuumed and then again back-filled with argon. This process was repeated several times. Finally, the argon was allowed to build up to a pressure of 2 psi and then the still bottom was opened to the air. Amidst the flowing argon, the round-bottomed flask was quickly attached to the still and then the excess pressure was released through the outlet line. Then, the argon flow was shut off and the outlet line was closed.

The solution in the flask was continuously stirred and heated to a temperature of $124^{\circ}C$. Occasionally, the outlet line was reopened to let out pressure. The solution was refluxed for 30 minutes and then 50 ml of isopropanol and 2-methoxyethanol were removed. After another 30 minutes then another 50ml was distilled. Finally, after a last
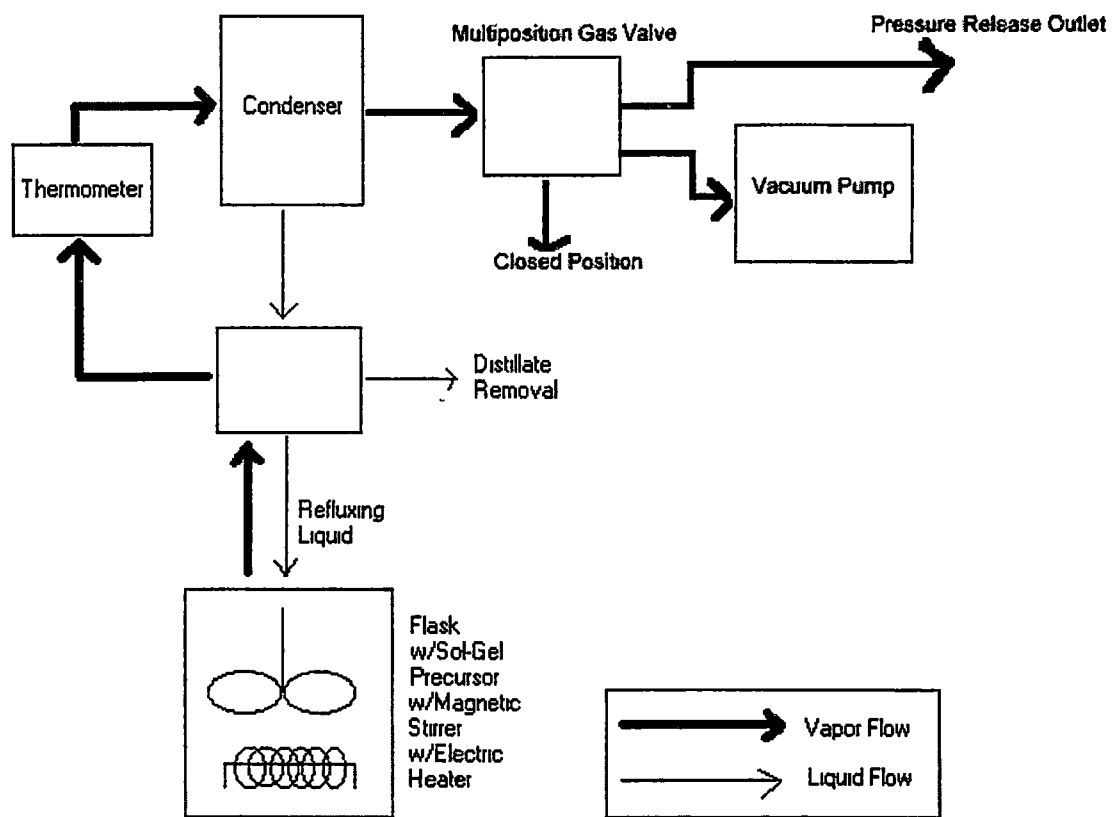
Figure 3.1 Diagram of Reflux Still for Precursor Solution Preparation

increment of 30 minutes, the solution was adjusted to a concentration of 0.5M of aluminum and lanthanum cations by removing the appropriate amount of solvent. This unhydrolyzed precursor solution was then cooled and stored in an inert glove box in preparation of partial hydrolysis.

A solution of 0.25M H_2O in 2-methoxyethanol was prepared separately to hydrolyze the precursor solution. A volume ratio of this solution was added to a portion of the unhydrolyzed precursor. This ratio is referred to as the degree of hydrolysis. The hydrolyzed solution was aged for at least one day prior to use.

Nickel Substrate Preparation

Mike Tomsic of Plastronic Inc. supplied UTSI with Plastronic "A" and "B" samples of roll-textured nickel. The difference in the samples was the type of roll used on the nickel. This nickel could be further treated through a resistive annealing process developed by Marvis White at UTSI. First, the chamber holding the sample between two electrodes was evacuated of air down to a pressure of 10^{-7} torr by use of a diffusion pump. Then an evaporative surface cleaning procedure followed. This procedure involved adjusting the voltage limit between the two electrodes to 20 volts. Then the current was switched on and quickly adjusted to 57 amps. This current was maintained for thirty seconds. Then the current was immediately lowered back down to zero. The vacuum pressure gage would show an increase of pressure to 10^{-4} torr during this period. The diffusion pump was then used to again lower the pressure to 10^{-7} torr. At this point, the chamber was backfilled with argon to atmospheric pressures. Lastly, the current

45

would be switched on and slowly raised to the desired value. Typical values used for annealing were 20 volts and 55-62 amps for 1 hour or more. A common difficulty incurred was the random melting of some of the nickel strips at high amperes. This was probably due to differences in thickness of the received nickel stock from Plastronic.

Cube Textured Nickel Oxide (NiO) on Ni Development

In some experiments, cubic textured, NiO was grown on the nickel substrate after the annealing process. This was accomplished by performing another vacuum surface cleaning step (as described above for nickel substrate preparation) and then introducing 50 microns of O_2. A current of 30 amps was applied for 15-17 minutes and then the sample was removed. When heat treating the deposited $LaAlO_3$ thin-film on the textured NiO/Ni substrate, a processing gas of just argon was used.

Dip Coating Procedures

Figure 3.2, page 47, shows the bench scale dip coating apparatus. Basically, commands were entered into the Microsoft Window's Terminal program. The computer then relayed the commands to the controller. The controller then drove the motor on the shaft, which moved the translating arm. A sample could be introduced into liquid inside an open container and then withdrawn at the desired constant velocity. The sample was then allowed to dry in air for a couple of minutes before being heat-treated.
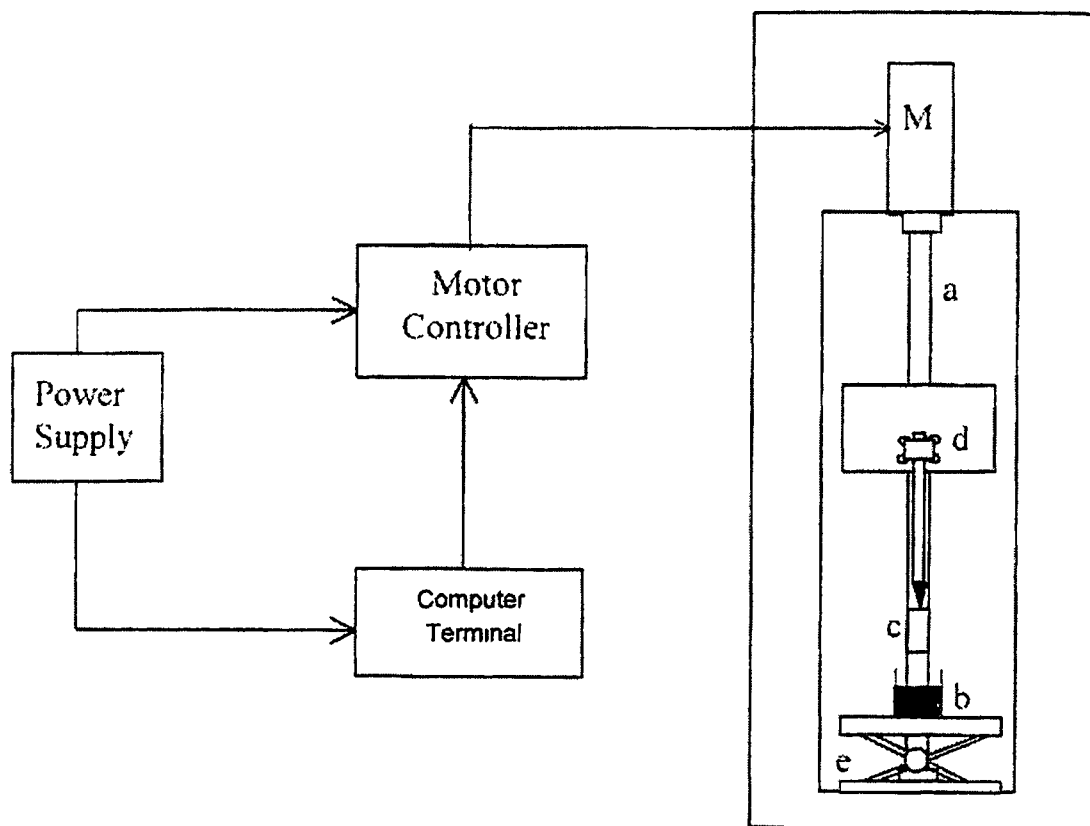
Figure 3.2 Diagram of Bench Scale Sol-Gel Dip Coating Unit

(a) Shaft (b) Solution Dispenser (c) Substrate (d) Translation Unit (e) Laboratory Jack

Adapted from Lasrado, V. Bench Scale Evaluation of Solution-Growth Based Techniques

For Manufacturing HTS Wire/Tape. Master's Thesis. Knoxville: University of

Tennessee, December 1998

47

Heat Treatment

After the sample was dried then it was ready for heat treatment. Initially, the sample was placed at the end of a one-end-open, mullite tube. The tube was then sealed with a specially designed cap that has openings for a thermal couple, a gas outlet tube, and a quartz, gas inlet tube of nearly equal length to the mullite tube. The tube was purged with a processing atmosphere for one hour. This processing atmosphere consisted mainly of high purity argon with 0 or 4 % hydrogen. Four percent hydrogen in argon is often referred to as forming gas. In the case of NiO textured samples, no argon was used. The tube was then raised on the platform and inserted into a tube furnace via a drawer slide mounted on a variable height platform. Typical temperatures used were $1150^{\circ}C$. The tube was then removed after 1/2 or 1 hour. The tube was then allowed to cool until near ambient temperatures by natural convection with the surrounding air. Then the cap was removed and the samples were taken out for analysis.

X-ray Diffraction Analysis

X-ray diffraction analysis was carried out with a Philips Analytical X'Pert system. This XRD (x-ray diffraction) machine was capable of scanning about multiple axes by use of a goniometer. The goniometer allows the machine to move along the omega, phi, and psi axis as well as simultaneously oscillate in the y-axis. Figure 3.3, page 49, shows an illustration of the goniometer's capable movements. Scans along the phi and the
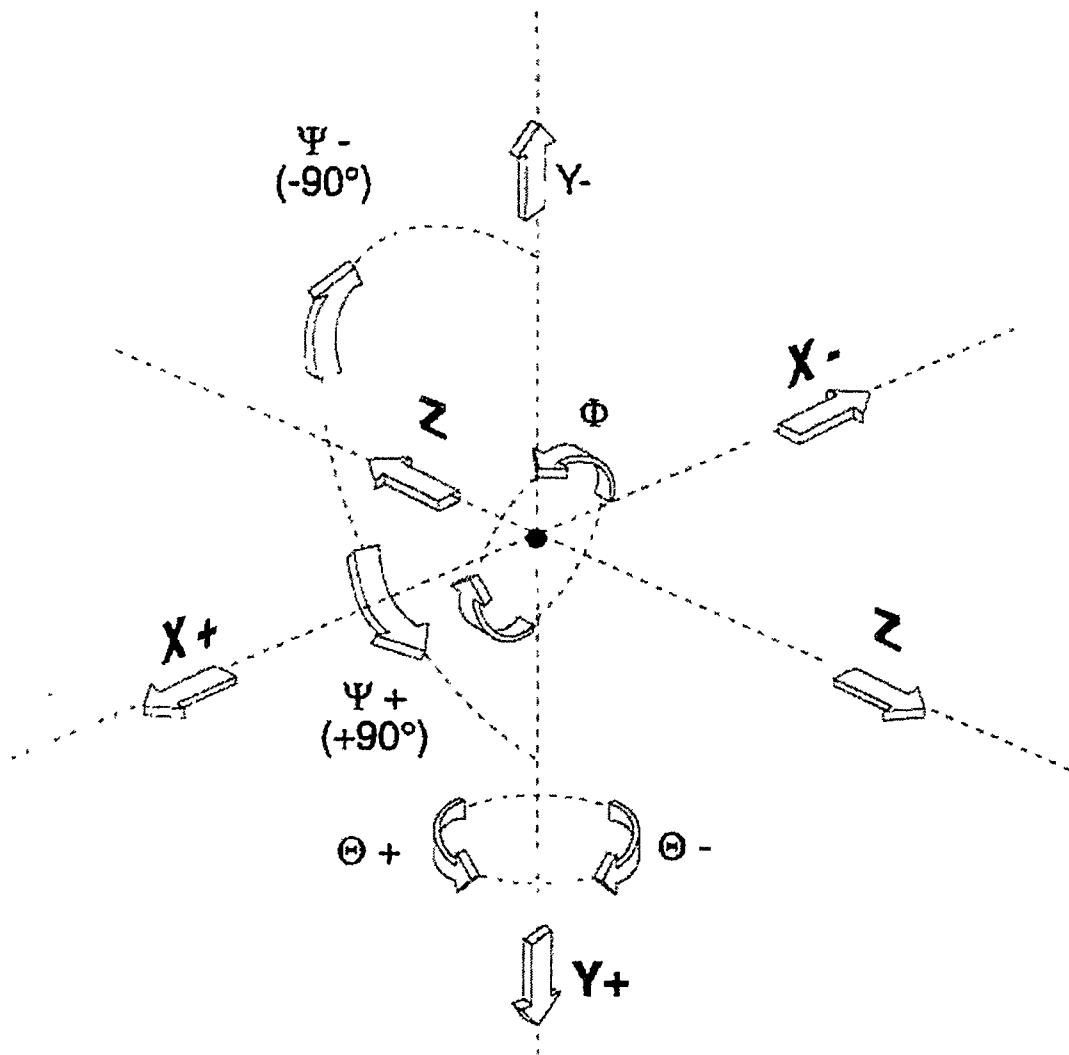
Figure 3.3 Capable Goniometer Movements

Source: Philips Analytical X'Pert-MRD User Guide 1995

omega axis were used to indicate the quality or sharpness of in-plane and out-plane texture respectively These scans generally referred to as phi and omega scans. Rotation of the detector about 2θ axis with fixing the omega axis at $\frac{1}{2}$ 2θ generated phase scans. Phase scans indicate the composition of a material as well as all the different out-plane orientations present. Finally, rotation in the phi axis coupled with a tilt in the psi axis produced pole figures. Pole figures can be used to detail the quality and quantity of orientations in the in-plane.

Raw data were collected and analyzed utilizing several software packages. Rocking curve data (phase scans) was analyzed using Jade 3.1 (by Materials Data Inc.). The peaks or diffraction lines were compared with a CD-ROM powder diffraction database and labeled if identifiable. Raw data for phi and omega scans were smoothed and curve fitted by Peakfit^{TM} version 4.0 (Jandel Scientific Software). Typically, the data were smoothed by 5% using a Savitzky-Golay algorithm and then curve fitted with Gaussian, Voigt, or Pearson VII algorithms.

Quantification of Epitaxial Growth

Epitaxial growth was evaluated in terms of the Phase, Omega, and Phi XRD scans. Phase scans were used to identify the major out-plane crystallographic orientations. Figure 3.4, page 51, shows a sample of a phase scan of $LaAlO_3$ on a cube textured nickel substrate. Preferred orientation can be readily determined from this scan. A quantitative number can be derived from the relative peak heights of the different orientations. For this work, a phase ratio number was defined as follows:
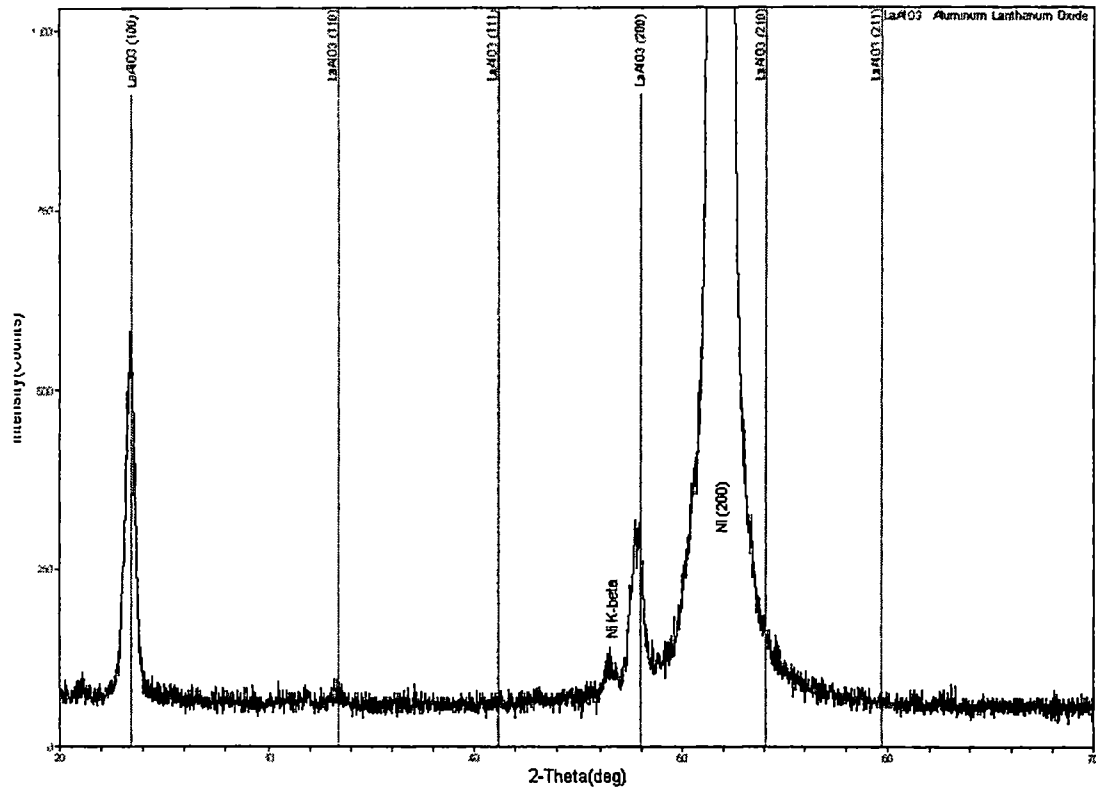
Figure 3.4 Typical Phase Scan of LaAlO$_3$ on Nickel Substrate

$$Phase\ Ratio = [(I_{100}+I_{200})/(I_{100}+I_{111}+I_{110}+I_{200})]*[I_{100}+I_{200}]$$

where I_{xxx} is the maximum intensity (counts recorded by XRD detector) of the diffraction

line corresponding to the xxx orientation

The phase ratio number basically represents the fraction of desired orientations by the total number of orientations present. This fraction was then multiplied by a weighting factor. The weighting factor is just the intensities of the desired phases. This weighting factor was used to insure results biased towards production of thick, highly epitaxial layers. For example, phase scans of two different samples are taken. Sample #1 has intensities of $I_{100}= 350$, $I_{200}= 150$, $I_{111}= 20$, and $I_{110} =80$. Sample #2 has only detectable intensities of $I_{100}= 50$, $I_{200}= 25$, $I_{111}= 0$, and $I_{110} = 0$. In just comparing the samples by fraction of desired orientation the sample #2 would be taken to have better results since all the orientations detected were desirable. However, with the weighting factor included then sample #1 is clearly preferred (416 to 75).

The sharpness or how perfectly the crystals are aligned in the in-plane and out-plane was determined by phi and omega scans respectively. Figures 3.5 and 3.6, page 53 and 54 respectively, show typical phi and omega scans obtained in this work. The full width at half maximum (FWHM) of the peaks were used to quantify the in-plane and out-plane alignment. This was defined as the follows:

Phi = average FWHM value of the 45° 135° 225° 315° peaks with reference to the (111)

plane
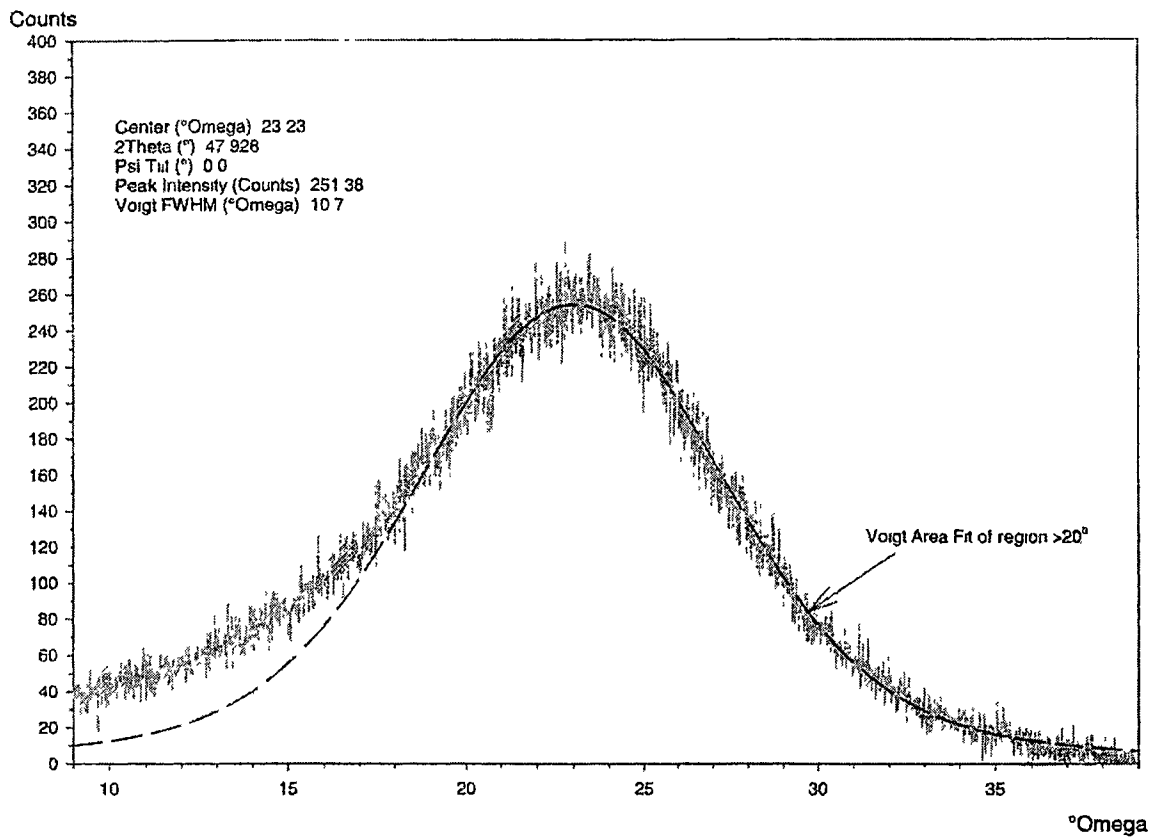
Figure 3.5 Typical (200) LaAlO$_3$ Omega Scan in the Rolling Direction

53

Counts

Average Pearson VII Δφ for the 4 peaks of (001)<100> is 10,81

Center (°Phi) 45 86
Peak Intensity (Cts) 106 8
Pearson VII FWHM (°Phi) 10 73

Center (°Phi) 136 2
Peak Intensity (Cts) 118 2
Pearson VII FWHM (°Phi) 11 25

Center (°Phi) 225 6
Peak Intensity (Cts) 112.6
Pearson VII FWHM (°Phi) 10 27

Center (°Phi) 316 16
Peak Intensity (Cts) 120 5
Pearson VII FWHM (°Phi) 10 97

Peaks at 45, 135, 225, and 315° are from (001)<100> oriented LaAlO$_3$
Peaks at 0, 90, 180, and 270° are from (001)<110> oriented LaAlO$_3$

°Phi

Figure 3 6 Typical (111) LaAlO$_3$ Phi Scan

Values for Phi and Omega for $LaAlO_3$ film on nickel substrates typically vary from 8° to 20°. On single crystal substrates such as Strontium Titanate, FWHM values are very small (~0.3).

To more concisely quantify epitaxial growth, one would require the knowledge of the phase ratio, phi, and omega scan measurements. In this work, they were combined to determine an arbitrary unit less number, Epitaxial #, as follows:

Epitaxial # = (a *Phase Ratio) / (b*omega) /(c*phi)

where a{x-ray counts^{-1}}, b{degrees^{-1}} , c{degrees^{-1}} are weighting coefficients

The weighting coefficients would ideally be determined experimentally from the response of the current carrying capacity of the superconductor layer to variation in the above parameters for the YBCO material. However, for this work one over the average of the experiment results for each scan was used as the weighting coefficient. Typical values are given in Chapter 4.

Lastly, an additional method of possibly measuring epitaxy was omitted. This method would involve comparing the relative amounts of correctly oriented $LaAlO_3$ in the in-plane to 45° twinned crystals. This could be quantified from either pole figures or from 360° phi scans. Figure 3.7, page 56, shows a pole figure for Plastronic's "B" cubic-textured nickel. An ideal cubic crystal will only have four dots or poles at the corners. A 360° phi scan will show the four peaks from the twin $LaAlO_3$ crystal as well as the four

55
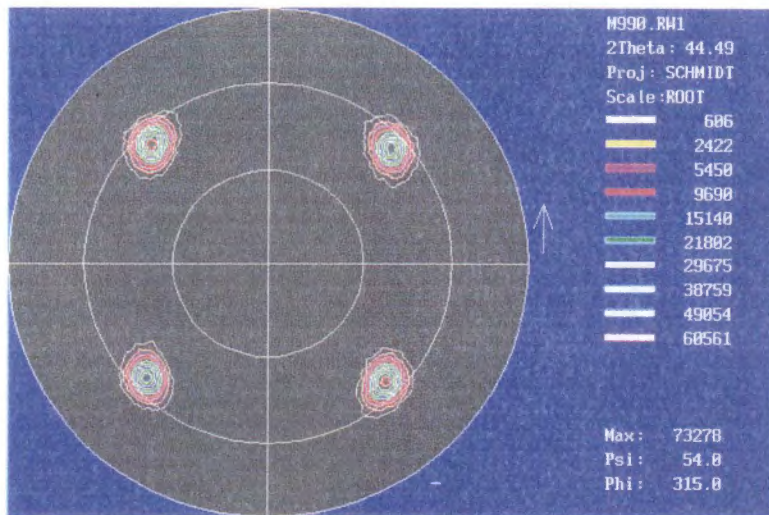
Figure 3.7 (111) Ni Pole Figure of Plastronic "B" Cubic Textured Nickel

Note: Poles at 45°, 135°, 225°, 315° are reflections of Ni (100)[001]

peaks for the (100) oriented material. The number of correctly oriented to twin crystals could be determined from a relative intensity ratio from either scan. However, most of the LaAlO$_3$ films developed during experimentation had very low intensities. Moreover, only the strong peaks showed discernable signs of in-plane twins This may skew a model based on those results to favor weak intensity results. As a result, pole figures were only used to qualitatively determine the degree of epitaxial growth.

Multifactorial Screening Experiment

Seven factors were screened using a two level Taguchi L12 design. The uncoded experimental matrix is shown in Table 3.1, page 58. The settings for each variable are then coded as −1 for low setting and +1 for high setting. The different models could be generated on using phi, omega, phase ratio, or a combined epitaxial # as the response. Trends and the level of significance of the factors can be determined from this type of experimental design.

The following is a description of each factor and its two level settings. Oven temperature or thermal treatment temperature of the coated samples had high and low values of 1150°C and 950°C respectively. Oven atmosphere refers to the percentage of hydrogen in argon during thermal treatment. The high and low values chosen were 4% hydrogen and 0% hydrogen. Oven time or thermal treatment time was the set at ½ hour and 1 hour. Solution concentration prior to hydrolysis was 0.1M and 0.25M. Degree of hydrolysis was set to 1 and 1.3. Withdrawal rate was either 1.5 cm/min or 4 cm/min.

Table 3.1 Uncoded Two Level Taguchi L12 Matrix

	Factors						
Row #	Oven Temperature (°C)	Oven Atmosphere (vol %H$_2$ in Ar)	Oven Time (hrs)	Solution Concentration (M)	Withdrawal Rate (cm/min)	Surface Roughness	Degree of Hydrolysis
1	950	0%	0.5	0.10	1.5	0	1.0
2	950	0%	0.5	0.10	1.5	1	1.3
3	950	0%	1.0	0.25	4.0	0	1.0
4	950	4%	0.5	0.25	4.0	0	1.3
5	950	4%	1.0	0.10	4.0	1	1.0
6	950	4%	1.0	0.25	1.5	1	1.3
7	1150	0%	1.0	0.25	1.5	0	1.3
8	1150	0%	1.0	0.10	4.0	1	1.3
9	1150	0%	0.5	0.25	4.0	1	1.0
10	1150	4%	1.0	0.10	1.5	0	1.0
11	1150	4%	0.5	0.25	1.5	1	1.0
12	1150	4%	0.5	0.10	4.0	0	1.3

Finally, surface roughness was a discrete factor where the nickel was polished (+1) or not polished (-1). The interactions between factors were assumed small in comparison to the individual factors themselves. Four repetitions were chosen for each of the twelve rows for a total sample size of forty eight runs. The sample size was determined by "rules of thumb" given by Schmidt and Launsby (1998). DOE KISS student version software (Air Academy Press, LLC. and Digital Computations, Inc.) was used to develop and analyze the two level design using multiple regression, Pareto Charts, and ANOVA techniques. Lastly, eight confirmation runs were used to verify trends observed in experimentation. Schmidt's and Launsby's "rule of thumb" for number of confirmation runs in the range of 4 to 20 confirmation runs, was used to determine the confirmation run size (1998).

Surface Roughness and Measurement

WYKO Vision^{TM} RT500 surface/optical profilometer was used in this work. The optical profilometer was used to examine differences in roughness of nickel substrates prepared by various techniques. The VSI (vertical scanning interferometry) mode was used. The WKYO manual suggested that the maximum vertical resolution for VSI was three nanometers The roughness of the nickel samples was assumed to be greater then that. The optical profilometer had a lateral resolution of 2.6X or 368 x 236 data points or pixels in a 1.8 mm by 2.4 mm scanning window.

Data were collected with regard to the roughness average (Ra), defined as;

$$R_a \equiv \frac{1}{MN} \sum_{k=1}^{M} \sum_{j=1}^{N} |Z_{jk}|$$

where N & M are the number of data points in each direction of the array, and Z is the Height

Uncoated samples were wiped cleaned with methanol and then placed underneath the microscope on the stage. Some samples were bent or deformed from residual stresses of rolling or from handling after thermal treatment. These samples were flattened as best as possible underneath some dead weights and then placed on the stage. Measurements were taken at random interval along the sample. Measurements were mainly taken in the center region of the nickel tape away from the ends. The very ends (last mm or so) of the samples are generally curled from being sliced from the main stock. For most samples, a natural tilt was present. The RT500 software allows this tilt to be removed from the data. Figure 3.8, page 61, shows an illustration of this feature.

Electropolishing of the Nickel Strips

Electropolishing was preformed in an agitated 500 ml beaker containing an electrolytic solution. A stainless steel cathode was held at one end of the beaker. The sample was lowered into the solution and held by a laboratory ring stand and clamp. A low ripple rectifier was used to supply current across the steel cathode, the electrolyte, and the nickel strip.

(a)

WYKO   Mag: 2.6 X
       Mode: VSI   **Surface Data**

Surface Statistics:
Ra: 6.52 um
Rq: 7.56 um
Rz: 27.77 um
Rt: 28.60 um

Set-up Parameters:
Size: 236 X 368
Sampling: 7.49 um

Processed Options:
Terms Removed:
None
Filtering:
None

mm
2.4
2.0
1.5
1.0
0.5
0.0

um
17.819
10.000
5.000
0.000
-5.000
-10.780

0.0 0.3 0.6 0.9 1.2   1.8   mm

(b)

WYKO   Mag: 2.6 X
       Mode: VSI   **Surface Data**

Surface Statistics:
Ra: 1.15 um
Rq: 1.36 um
Rz: 6.67 um
Rt: 16.91 um

Set-up Parameters:
Size: 236 X 368
Sampling: 7.49 um

Processed Options:
Terms Removed:
Tilt
Filtering:
None

mm
2.4
2.0
1.5
1.0
0.5
0.0

um
14.411
11.000
8.000
5.000
2.000
-2.500

0.0 0.3 0.6 0.9 1.2   1.8   mm

Figure 3.8 Removal of Natural Tilt in Samples

(a) Scan of Nickel Substrate taken without tilt removed.

(b) Scan taken with tilt removed.

An electrolyte of 70% volume glacial acetic acid and 30% volume (60% concentration perchloric acid) was used originally used based on recommended electrolytes for nickel from the American Society of Testing and Materials' literature. However, the plating rate was too fast and the edges of the nickel tape were eaten away. Diluting the electrolyte solution with an equal volume of water and using 3.5 volts produced better results by visual inspection. The polishing rate was 0 42mg/min and the current density was approximately $0.033A/cm^2$. Samples polished appeared slightly brighter in the polished region from visual inspection.

CHAPTER 4

EXPERIMENTAL RESULTS AND DISCUSSION

Taguchi L12 Screening Experiment

Tables 4.1-4 3 , pages 64-69, show the results of phi, omega, and phase scans.

Table 4 4, pages 70-71, shows the calculated epitaxial # for each experimental run. The

epitaxial # was calculated using the weighting coefficients of a $=1/108.29$, b $= 16.26$, and

c $= 1/19.08$. That is the values of phi, omega, and phase ratio were weighted by each

respective average.

Each of the sets of raw data (phi, omega, phase ratio, and epitaxial #) were

modeled for predicted response ($\overline{Y}$ or Y-bar model) and for predicted variance among

different samples ($\overline{S}$ or S-bar model). The general form used for regression models was:

$$\overline{Y} \equiv constant + a_1 * Temp + b_1 * Atmos + c_1 * Time + d_1 * Conc + e_1 * Withdrawal$$
$$+ f_1 * Roughness + g_1 * Hydrolysis$$

$$\overline{S} \equiv constant + a_2 * Temp + b_2 * Atmos + c_2 * Time + d_2 * Conc + e_2 * Withdrawal$$
$$+ f_1 * Roughness + g_1 * Hydrolysis$$

,where $a_1, a_2, b_1, b_2, c_1, c_2, d_1, d_2, e_1, e_2, f_1, f_2, g_1, g_2$ are the coefficients determined from

regression and temp (oven temperature), atmos (oven atmosphere), conc (solution

concentration), withdrawal (withdrawal rate), roughness (surface roughness), and

hydrolysis (degree of hydrolysis) are the independent variables which represent the

coded factors (-1, +1)

Table 4 1 Phase Ratio Results for Taguchi L12 Screening Experiments

Sample ID	I_{100}	I_{110}	I_{111}	I_{200}	$I_{100+200}$	I_{total}	$(I_{100}+I_{200})^2/(I_{total})$
1A	35	50	0	0	35	85	14
1B	40	37	0	0	40	77	21
1C	43	25	0	0	43	68	27
1D	0	0	0	0	0	0	0
2A	48	0	0	63	111	111	111
2B	63	52	0	0	63	115	35
2C	45	40	0	0	45	85	24
2D	68	44	0	0	68	112	41
3A	150	170	0	100	250	420	149
3B	115	205	0	85	200	405	99
3C	115	70	30	80	195	295	129
3D	90	60	30	60	150	240	94
4A	30	0	0	0	30	30	30
4B	0	0	0	0	0	0	0
4C	50	0	0	0	50	50	50
4D	45	0	0	0	45	45	45
5A	50	40	0	0	50	90	28
5B	70	50	0	55	125	175	89
5C	60	55	0	45	105	160	69
5D	50	0	0	0	50	50	50
6A	0	0	0	0	0	0	0
6B	0	0	0	0	0	0	0
6C	50	0	0	0	50	50	50
6D	35	0	0	0	35	35	35
7A	65	65	0	60	125	190	82
7B	215	105	0	115	330	435	250
7C	105	140	0	55	160	300	85
7D	50	100	0	0	50	150	17
8A	150	85	0	65	215	300	154
8B	75	160	0	70	145	305	69
8C	75	80	0	75	150	230	98
8D	205	55	0	70	275	330	229
9A	75	90	0	55	130	220	77

Table 4.1 Continued

9B	105	50	0	75	180	230	141
9C	160	80	0	90	250	330	189
9D	150	105	0	0	150	255	88
10A	90	0	0	68	158	158	158
10B	250	0	0	265	515	515	515
10C	255	0	0	140	395	395	395
10D	295	0	0	160	455	455	455
11A	60	30	25	50	110	165	73
11B	75	25	0	50	125	150	104
11C	40	20	0	0	40	60	27
11D	80	50	0	70	150	200	113
12A	210	0	0	130	340	340	340
12B	40	20	0	50	90	110	74
12C	50	0	0	30	80	80	80
12D	120	0	0	75	195	195	195

Table 4.2 Omega FWHM Results for Taguchi L12 Screening Experiments

Sample ID	Omega FWHM
1A	17.11
1B	17.19
1C	18.32
1D	17.89
2A	17.31
2B	16.60
2C	16.70
2D	17.18
3A	15.86
3B	15.12
3C	15.47
3D	17.25
4A	17.93
4B	17.77
4C	17.28
4D	16.85
5A	17.08
5B	16.68
5C	15.78
5D	16.60
6A	17.17
6B	16.93
6C	17.27
6D	17.17
7A	16.64
7B	14.53
7C	16.86
7D	16.82
8A	15.84
8B	15.94
8C	17.31
8D	14.99

Table 4.2 Continued

9A	17.42
9B	16.84
9C	14.30
9D	17.15
10A	15.45
10B	12.51
10C	13.18
10D	12.32
11A	17.39
11B	16.25
11C	15.38
11D	17.09
12A	13.82
12B	16.21
12C	14.15
12D	15.57

Table 4.3 Phi FWHM Results for Taguchi L12 Screening Experiments

	Pearson VII FWHM Peaks				
Sample ID	45°	135°	225°	315°	Avg.
1A	20.61	21.41	21.16	22.78	21.49
1B	18.68	17.58	18.76	21.45	19.12
1C	25.92	22.37	21.22	27.59	24.27
1D	28.35	26.83	24.73	27.16	26.77
2A	18.17	16.31	15.67	19.28	17.36
2B	18.42	17.93	13.31	18.27	16.98
2C	18.75	19.95	15.97	18.36	18.26
2D	18.93	17.76	18.88	20.21	18.95
3A	17.03	16.64	14.58	21.40	17.41
3B	20.92	18.84	13.36	19.03	18.04
3C	17.85	17.75	15.54	17.78	17.23
3D	27.18	23.23	13.56	21.25	21.30
4A	18.14	24.14	19.78	22.26	21.08
4B	26.42	23.60	18.30	25.80	23.53
4C	26.56	25.15	16.34	28.33	24.09
4D	21.91	23.02	20.99	22.67	22.15
5A	23.39	21.44	21.35	25.71	22.97
5B	26.99	N/A	N/A	N/A	26.99
5C	19.23	19.51	17.17	20.38	19.07
5D	21.81	22.60	22.09	22.70	22.30
6A	20.61	18.82	19.40	20.99	19.96
6B	18.70	24.02	16.46	23.73	20.73
6C	18.68	19.78	19.77	21.64	19.97
6D	20.17	24.44	15.08	28.08	21.94
7A	14.66	15.00	14.89	17.08	15.41
7B	11.21	11.05	11.83	12.43	11.63
7C	11.82	13.25	12.41	13.80	12.82
7D	21.00	23.14	18.18	23.75	21.52
8A	12.56	13.65	12.70	12.16	12.77
8B	14.03	14.59	13.88	16.17	14.67
8C	13.51	17.02	15.82	16.27	15.65
8D	14.71	16.94	12.62	15.68	14.99

Table 4.3 Continued

9A	16.02	15.91	13.43	18.92	16.07
9B	27.18	27.75	15.59	23.71	23.55
9C	12.94	16.55	15.10	16.01	15.15
9D	18.62	15.90	14.08	16.90	16.38
10A	22.00	18.45	16.43	21.62	19.62
10B	15.09	14.07	13.49	15.09	14.43
10C	13.09	15.21	11.93	13.44	13.42
10D	14.11	13.78	12.07	14.43	13.60
11A	20.52	20.92	21.51	20.51	20.86
11B	17.58	21.17	14.59	19.09	18.11
11C	13.85	13.92	13.75	14.78	14.07
11D	22.31	21.33	19.34	23.65	21.66
12A	16.04	21.19	13.93	17.26	17.11
12B	17.04	21.73	18.21	23.41	20.09
12C	20.33	20.53	16.91	20.69	19.62
12D	23.04	19.42	19.38	20.33	20.54

Table 4.4 Epitaxial # Results for Taguchi L12 Screening Experiments

Sample ID	Epitaxial #
1A	0.11
1B	0.18
1C	0.18
1D	0.00
2A	1.06
2B	0.35
2C	0.22
2D	0.36
3A	1.54
3B	1.04
3C	1.39
3D	0.73
4A	0.23
4B	0.00
4C	0.34
4D	0.35
5A	0.20
5B	0.57
5C	0.66
5D	0.39
6A	0.00
6B	0.00
6C	0.42
6D	0.27
7A	0.92
7B	4.24
7C	1.13
7D	0.13
8A	2.18
8B	0.84
8C	1.03
8D	2.92

Table 4.4 Continued

9A	0.79
9B	1.02
9C	2.50
9D	0.90
10A	1.49
10B	8.17
10C	6.40
10D	7.78
11A	0.58
11B	1.01
11C	0.35
11D	0.87
12A	4.12
12B	0.65
12C	0.83
12D	1.75

The nickel substrate was Plastronic "A" nickel for all samples in the Taguchi L12 screening experiments. It was not resistively annealed prior to polishing. The nickel underwent recrystallization during the thermal treatment after coating. This was evident from pole figure scans. Figure 4.1, page 73, shows a before and after pole figure scan for the Plastronic "A" nickel.

Significance and Trends Identified Solely by Omega FWHM

Table 4.5, page 74, shows the results of multiple regression analysis of the Taguchi L12 experimental design. It is important to note that those coefficients which were not significant (P(2 tail)>0.10) were considered to have zero magnitude. _ Magnitudes other than zero may be as a result of experimental error or of natural variance in the sample. Figure 4.2, page 75, shows the Pareto charts of both the $\overline{\overline{Y}}$ and the $\overline{\overline{S}}$ model. From Pareto charts, oven temperature was found to be both an important factor in both lowering the omega FWHM and increasing the variance among samples. According to P(2 tail) testing of each coefficient in the $\overline{\overline{Y}}$ model, the following additional terms were judged significant: oven atmosphere, oven time, solution concentration, and surface roughness.

The effect of time and temperature on improving the $LaAlO_3$ out-plane sharpness may be due to increased crystallization rate of $LaAlO_3$ and reduction in the residual amorphous material Residual amorphous $LaAlO_3$ would cause the broadening of out-plane texture peaks. Another possible effect is that the increasing time and temperature

(a)
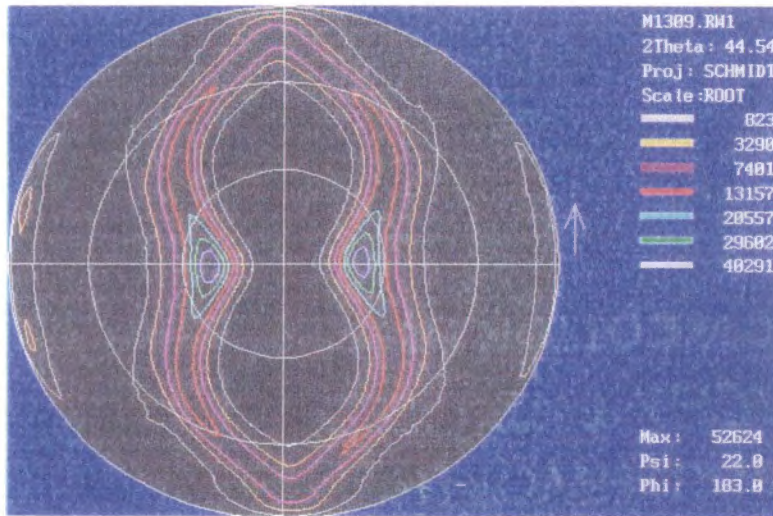
(b)
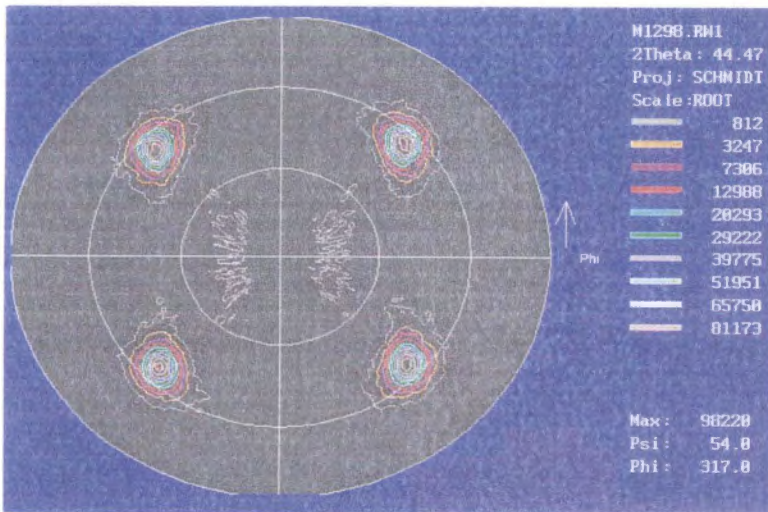
Figure 4.1 Effect of Nickel Recrystallization

(a) Plastronic "A" (111) Ni pole figure

(b) Plastronic "A" (111) Ni pole figure after 1 hour at 1150°C.

Note: Poles at 45°, 135°, 225°, 315° correspond to (100)[001] Ni.

Other poles correspond to (212)[212] cube textured Ni twin.

Table 4.5 Significant Factors Based Solely on Omega FWHM Data

Response Model (Y-hat)			Variance Model (S-hat)		
Factor	Regression Coefficient	P (2 Tail)	Factor	Regression Coefficient	P (2 Tail)
Oven Temperature	-0.68	0.00	Oven Temperature	0.33	0.00
Oven Atmosphere	-0.27	0.09	Oven Atmosphere	-0.06	0.26
Oven Time	-0.39	0.01	Oven Time	0.02	0.68
Solution Concentration	0.35	0.03	Solution Concentration	0.00	0.97
Withdrawal Rate	-0.04	0.78	Withdrawal Rate	0.08	0.16
Surface Roughness	0.34	0.03	Surface Roughness	-0.11	0.07
Degree of Hydrolysis	0.19	0.22	Degree of Hydrolysis	-0.14	0.04
Constant	16.26		Constant	0.84	

Note: Significant Factors are Underlined

(a)
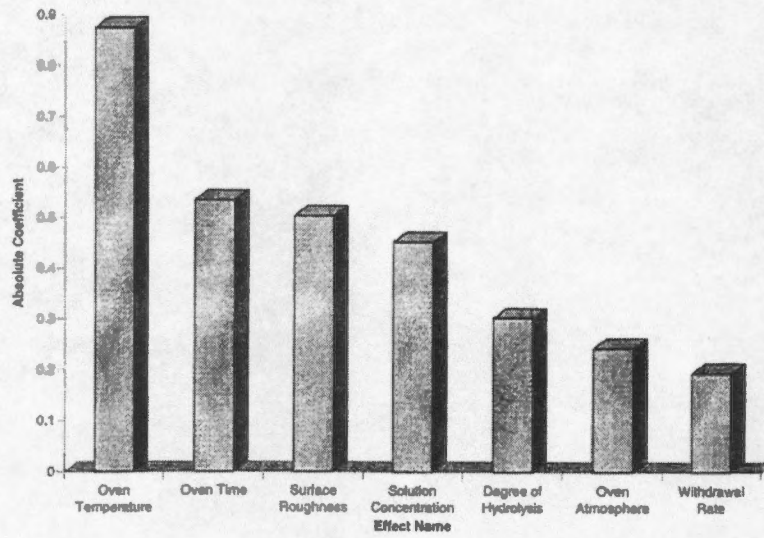
(b)
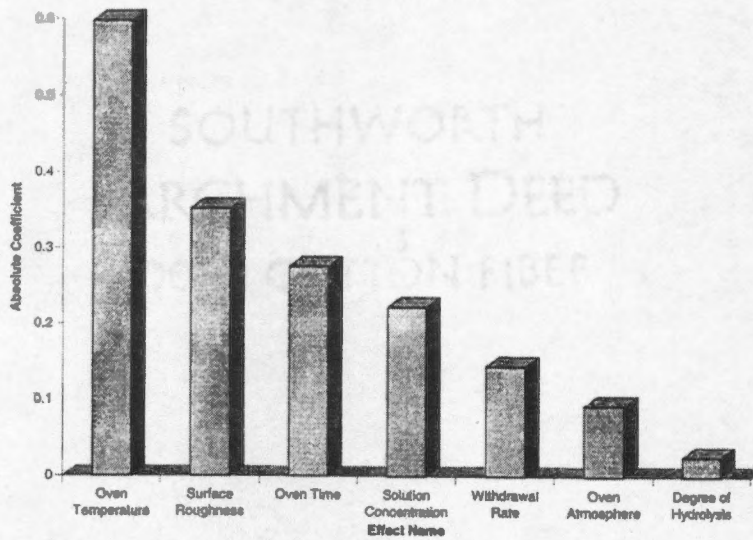
Figure 4.2 Pareto Charts for Omega FWHM Data

(a) $\overline{Y}$ Pareto Chart   (b) $\overline{S}$ Pareto Chart

Note: Where absolute coefficient refers to the absolute value of the regression coefficient.

could improve the texture of the nickel substrate. However, this could be ruled out when omega and phi scans of the nickel substrate were taken. Figure 4.3, page 77, shows an effect plot of the time and temperature on the nickel substrate's out-plane and in-plane textures The very small slopes suggest that the nickel texture was not improved and varied only slightly over the Taguchi L12 experimental design. Therefore, it is unlikely that the nickel texture improvements could have accounted for the enhanced performance in the omega FWHM of $LaAlO_3$.

The increase in out-plane sharpness with the presence of 4% H_2 in is in agreement with the ORNL study performed on the epitaxially growth of CeO_2 under various partial pressures of forming gas. ORNL demonstrated that the increasing the partial pressure of forming gas increased the epitaxial growth up to a maximum point (ORNL Annual Report, 1998). They concluded that the forming gas or (more specifically the hydrogen) helped decrease the formation of complex NiO (ORNL Annual Report, 1998). NiO has been suggested as a possible interference to the epitaxial growth of buffer layers (ORNL Annual Report, 1998).

The omega FWHM decreased with polished samples as opposed to unpolished. The significance of surface roughness could be interpreted as analogous to building a house. For instance, to build a level home the foundation has to be level as well as the ground surrounding it. In analogy, the nickel substrate not only has to be a sharp crystal texture, but also it has to be a smooth, low roughness surface.

Less concentrated precursor solutions produced sharper omega FWHM. This may be related a crystallization rate which is fixed by time and temperature At lower concentrations, there the resulting film is thinner than films created from more
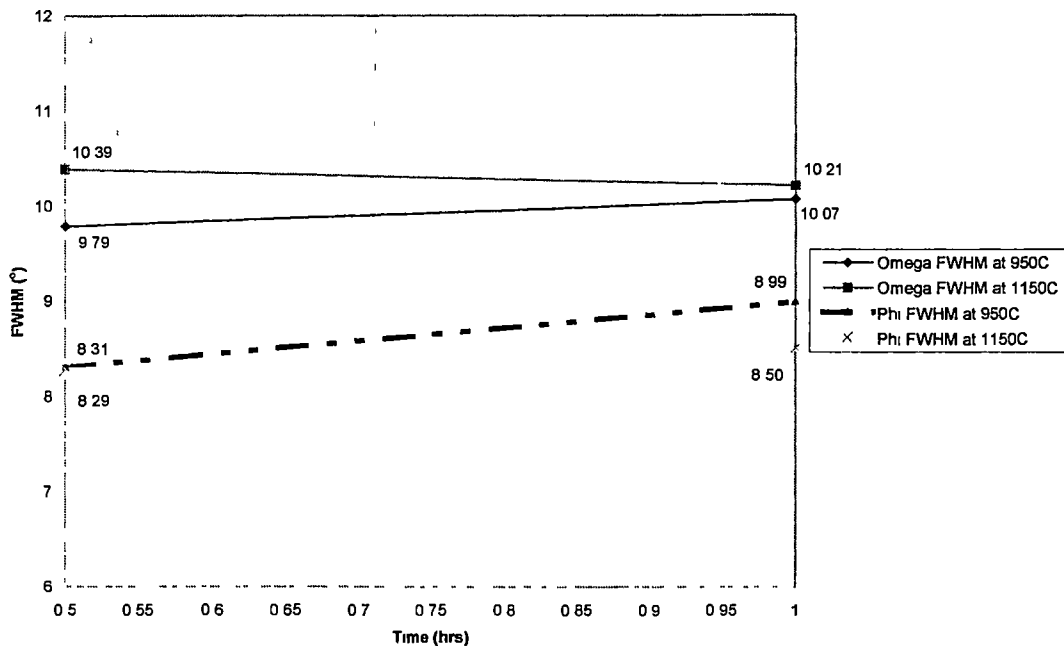
Figure 4.3 Effect of Time and Temperature on Nickel Substrate In-Plane and Out-Plane

Texture

concentrated precursors. The crystallization rate may be slow enough to allow for incomplete crystallization of thicker films. The would lead to the presence of amorphous material which will widen the omega FWHM.

In the $\bar{S}$ model, surface roughness and degree of hydrolysis were also found to be significant. Increases in degree of hydrolysis and roughness reduced the amount of scatter in the response. Experimental error in the electropolishing of the surface may have accounted for the increased scatter. The current flow and consequent current density may have changed slightly from sample to sample due to observed variance in the nickel substrate thickness. Slight differences in the current from sample to sample for the same voltage was also noted during electropolishing. Thus, the random nature of the thickness of the nickel strip and experimental error in placement of the sample in relation to the cathode may have accounted for the additional scatter. The effect of degree of hydrolysis was unclear and may have been as a result of experimental error.

Significance and Trends Based Solely on Phi FWHM

Table 4.6, page 79, shows the results of the analysis based solely on phi FWHM data. Figure 4.4, page 80, shows the Pareto charts for both the $\bar{Y}$ and the $\bar{S}$ model. In examining $\bar{Y}$ model's P(2 tail)s for each coefficient, increasing oven temperature and time was found to be significant for improving the in-plane texture. The reasoning behind this is probably similar to that for the omega scan above. This agreement between the omega and the phi $\bar{Y}$ models may be an indicator of the correctness of the model, if one

78

Table 4.6 Significant Factors Based Solely on Phi FWHM Data

Response Model (Y-hat)			Variance Model (S-hat)		
Factor	Regression Coefficient	P (2 Tail)	Factor	Regression Coefficient	P (2 Tail)
<u>Oven Temperature</u>	-2.25	0.00	Oven Temperature	0.48	0.26
<u>Oven Atmosphere</u>	1.25	0.01	Oven Atmosphere	-0.18	0.64
<u>Oven Time</u>	-0.81	0.07	Oven Time	0.02	0.96
Solution Concentration	-0.13	0.76	Solution Concentration	0.23	0.57
Withdrawal Rate	0.62	0.16	Withdrawal Rate	-0.23	0.56
Surface Roughness	0.06	0.88	Surface Roughness	-0.16	0.69
Degree of Hydrolysis	-0.67	0.13	Degree of Hydrolysis	-0.70	0.13
Constant	19.08		Constant	2.42	

Note: Significant Factors are Underlined

(a)
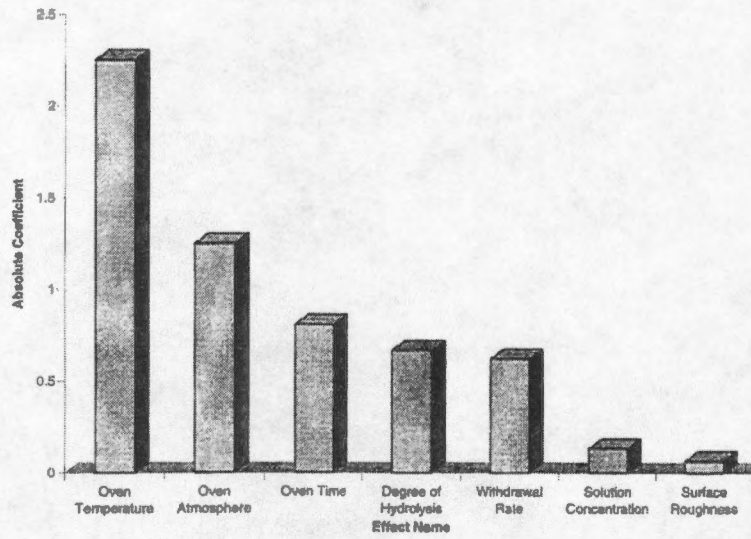
(b)

Figure 4.4 Pareto Charts for Phi FWHM Data

(a) $\overline{Y}$ Pareto Chart   (b) $\overline{S}$ Pareto Chart

Note: Where absolute coefficient refers to the absolute value of the regression coefficient.

assumes that the mechanism for epitaxial growth is similar for both the out-plane and in-plane textures. The oven atmosphere term indicated widening of in-plane texture with the addition of H_2 in argon ORNL had reported that the epitaxial growth improved with an increase in the forming gas partial pressure up to an optimum point and then diminished with further increases in pressure (ORNL Annual Report, 1998). ORNL suggested the impurities in the forming gas such as moisture and O_2 may have become sufficient enough to stabilize the growth of NiO again (ORNL Annual Report, 1998). For the Taguchi L12 tests, impurities in the gases and experimental error may have caused the in-plane texture to worsen with the addition of hydrogen.

In the multiple regression $\bar{S}$ model, no terms were found to be significant. ANOVA analysis of the model showed that the model may just be representing the random noise (F~1). Moreover, there was no correlation between the variance in the response with any factor. It is uncertain whether more data points would reveal any direct correlation between a factor and scatter in the response.

Significance and Trends Based Solely on Phase Ratio

Table 4.7, page 82, shows the results of analysis based solely on the phase ratio data. Figure 4.5, page 83, shows the Pareto charts for both the $\bar{Y}$ and the $\bar{S}$ model. Oven temperature again is found to be the most significant in both the $\bar{Y}$ and the $\bar{S}$ models. This is in agreement with the results from ORNL. ORNL has shown with various phase scans at different temperatures that the peaks grow stronger with increasing temperatures

Table 4.7 Significant Factors Based Solely on Phase Ratio Data

Response Model (Y-hat)			Variance Model (S-hat)		
Factor	Regression Coefficient	P (2 Tail)	Factor	Regression Coefficient	P (2 Tail)
Oven Temperature	58.7	0.00	Oven Temperature	32.6	0.01
Oven Atmosphere	15.7	0.22	Oven Atmosphere	7.9	0.36
Oven Time	29 2	0.03	Oven Time	9.5	0.28
Solution Concentration	-28.0	0.03	Solution Concentration	-13.8	0.15
Withdrawal Rate	-1.4	0.91	Withdrawal Rate	-4.1	0.62
Surface Roughness	-29.4	0.02	Surface Roughness	-15.7	0.11
Degree of Hydrolysis	-21.0	0.10	Degree of Hydrolysis	6.0	0.48
Constant	108.3		Constant	57.7	

Note: Significant Factors are Underlined
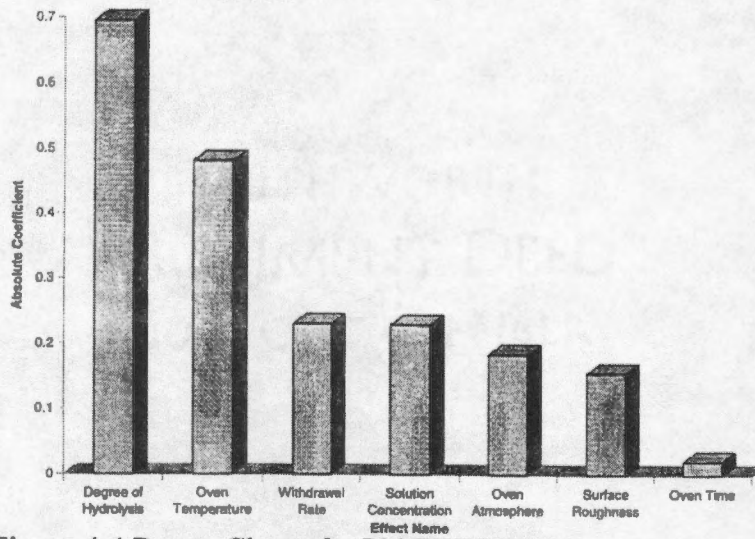
(a)
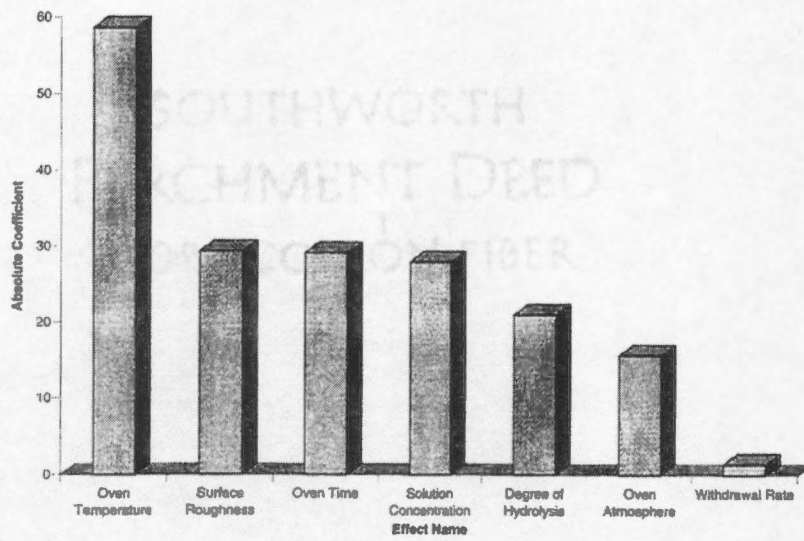
(b)

Figure 4.5 Pareto Charts for Phase Ratio Data

(a) $\overline{Y}$ Pareto Chart   (b) $\overline{S}$ Pareto Chart

Note: Where absolute coefficient refers to the absolute value of the regression coefficient.

(ORNL Annual Report, 1996). The implication is that more LaAlO$_3$ is probably crystallizing. The increased variance with oven temperature may be related to the amount of crystals formed. The intensity-to-amount of crystal material relationship is not a simple linear relationship. Small increases in crystalline material lead to much larger intensities This then widens the difference between the samples and causes a change in the variance.

Multiple regression also identified surface roughness, solution concentration, oven temperature, and oven atmosphere for the $\overline{Y}$ model as the significant parameters All of these terms were identified as significant in the omega model too. Some agreement between the omega and phase ratio data was anticipated. A phase scan projects the entire composition of the general orientations (100&200,111,110) in the out-plane. Whereas, an omega scan shows the how sharply the material is aligned to one of the general out-plane orientations. Steps that improve the sharpness of an orientation on the omega scan may increase its intensity on the phase scan and vice versa.

Significance and Trends in the Final Epitaxial #

Table 4.8, page 85, shows the results of regression analysis based on epitaxial #. Figure 4.6, page 86, shows the Pareto charts for both the $\overline{Y}$ and the $\overline{S}$ model. Again the oven temperature is found to be the most significant factor in both response and variance. This verifies the assumption that the factors significant in the previous models should be significant in a combined model too.

Table 4.8 Significant Factors Based on Epitaxial # Data

Response Model (Y-hat)			Variance Model (S-hat)		
Factor	Regression Coefficient	P (2 Tail)	Factor	Regression Coefficient	P (2 Tail)
Oven Temperature	0.88	0.00	Oven Temperature	0.60	0.03
Oven Atmosphere	0.24	0.25	Oven Atmosphere	0.09	0.62
Oven Time	0.54	0.01	Oven Time	0.28	0.19
Solution Concentration	-0.45	0.03	Solution Concentration	-0.22	0.27
Withdrawal Rate	-0.19	0.36	Withdrawal Rate	-0.14	0.45
Surface Roughness	-0.50	0.02	Surface Roughness	-0.35	0.11
Degree of Hydrolysis	-0.30	0.15	Degree of Hydrolysis	0.03	0.89
Constant	1.32		Constant	0.83	

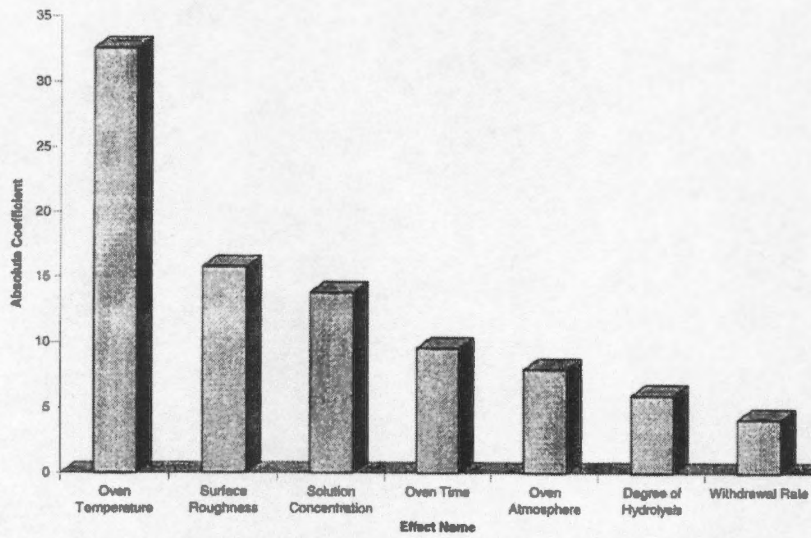Note: Significant Factors are Underlined

(a)
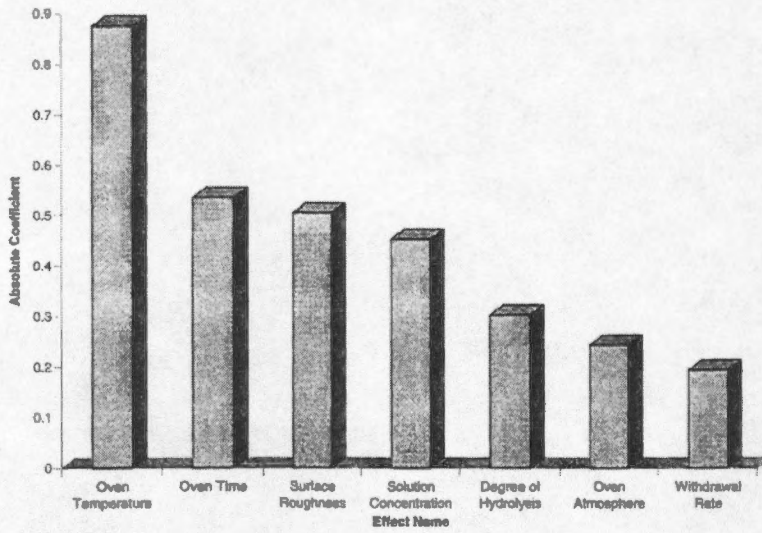
(b)
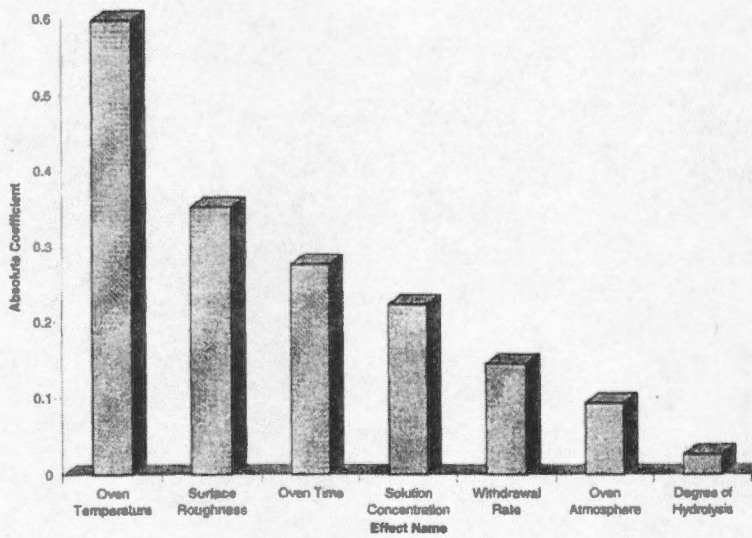
Figure 4.6 Pareto Charts for Epitaxial #

(a) $\overline{Y}$ Pareto Chart   (b) $\overline{S}$ Pareto Chart

Note: Where absolute coefficient refers to the absolute value of the regression coefficient.

Multiple regression supports this hypothesis by again showing the additional significant terms in the $\overline{Y}$ model as solution concentration, surface roughness, and oven time. The epitaxial # is primarily in agreement with the phase ratio results. The phase ratio had much more variance around its mean value during the experiment. As a result, the phase ratio's greater range of deviation has given itself a greater weighting in the epitaxial #, and the effect of the oven atmosphere has been skewed out as insignificant, even though it had significant influence on both the omega and the phi FWHM models.

Finally, the withdrawal velocity had no effect on the epitaxial growth over the range it was studied (1.5-4 cm/min). Work done by Lasrado, suggests that at much higher velocities (greater than 40 cm/min), the in-plane and out-plane sharpness decreased on single crystals of $SrTiO_3$ (1998). However, over the short ranges used in this thesis, the factor was found to be insignificant with respect to all the data and the final epitaxial #.

In terms of the $\overline{S}$ model, the only significant term was found to be the oven temperature. The data scattering effect of surface roughness as noted in the omega data was not present in the epitaxial #. This was probably caused by the phase ratio and the phi scan data outweighing the omega scan data.

Strength of Regression Models and Conformation Runs

Table 4.9, page 88, shows F-values and R^2 values for all the models. The R^2 values for most of the models indicated a rather high lack of fit. Schmidt and Launsby give possible reasons for low R^2: (1) the factors are not related to the response, (2) low

Table 4.9 Performance of Regression Models

Model Name	F	R^2
Y-bar (Omega FWHM)	5 93	0 51
S-bar (Omega FWHM)	9 98	0 95
Y-bar (Phi FWHM)	6 22	0 52
S-bar (Phi FWHM)	0 94	0 62
Y-bar (Phase Ratio)	6 00	0 51
S-bar (Phase Ratio)	4 11	0 88
Y-bar (Epitaxial #)	5 69	0 50
S-bar (Epitaxial #)	2 99	0 84

Note: See pages 38 and 41 for definitions of R^2 and F.

and high settings of the factors too close together, and (3) the model used is wrong. (1998). On the first point, the values of F=6 for all the $\overline{Y}$ models suggest that the variance in the response is not just a representation of the total population's mean variance. Also, for the omega and phase ratio $\overline{S}$ models, F values were near or exceeded 6, indicating that there was some relationship between the independent variables and the dependent variable in the $\overline{Y}$ and $\overline{S}$ models. For the second point, the low and high settings, with the exception of the withdrawal velocity, were set apart at distances as large as possible while still obtaining meaningful results. For instance, when a concentrated solution 0.25M was hydrolyzed by a degree of 1.3 it caused precipitates to fall out of solution, indicating that parameter was bound to by an upper limit of 0.25M.

However, dealing with the third point, the model may be wrong as the assumptions of linearity and no interaction of terms may not be true. The 2-level Taguchi L12 design does not account for any nonlinearly and or interactions between the terms. Any adjustments made to include quadratic and interaction terms would lessen the degree of orthogonality through confounding or aliasing of all the factors with one another. Such confounding or multicolinearity could lead to incorrect results such as the reversal of signs on the regression coefficients. Another source of error may have incurred during the XRD analysis. Several scans produced low signal-to-noise ratios. That is that the peaks barely rose above the background levels. This was probably due to small deposition thicknesses or large amounts of the coating remaining in an undetectable amorphous state.

Eight confirmation runs were preformed at the settings described in Table 4.10, page 91, to test the observed trends. The same weighting coefficients as found from the Taguchi L12 screening experiments were used for calculating epitaxial #. The results, shown in Table 4 10, indicate drastic improvement in the omega, phi, phase ratio, and finally the epitaxial #. This suggests that the identified trends were to some degree correctly predicted by the regression coefficients on all the models. In comparison of sharpness of the data with the work done by Vineet Lasrado on ORNL RABiTS nickel, the average omega FWHM value for the confirmation runs (11.94°) is slightly higher than the average of the values reported (10.55°). The average phi FWHM (12.31°) is lower than the average reported value (15.75°). Finally, with regards to in-plane twinning of LaAlO$_3$, both (100) and the (110) poles were visible on pole figures of the confirmation run samples. Figure 4.7, page 92, shows a LaAlO$_3$ pole figure. The intensity of the in-plane twin is about half of the (100) material. In-plane twinning has been reported by both ORNL and Vineet Lasrado. (Lasrado, 1998; ORNL Annual Report, 1998)

LaAlO$_3$/NiO/Ni Scheme Results

A textured (100) NiO layer was deposited on some Ni substrates after resistive annealing for one hour. This procedure, developed by Marvis White, was outlined earlier in Chapter 3. Verification of the epitaxial cube textured NiO was accomplished through phase, phi, and omega scans. A NiO phase scan is presented in Figure 4.8, page 93. Figure 4.9, page 94, shows an omega scan of the NiO (200), figure 4.10, page 95, shows a phi scan of (111) NiO, and Figure 4.11, page 96, shows a Ni(111) pole figure. LaAlO$_3$

Table 4.10 Confirmation Runs

Factor Settings			
Oven Temperature 1150°C , Oven Atmosphere 4% H_2, Oven Time 1hr, Surface Roughness 0(Polished), Degree of Hydrolysis 1.3, Solution Concentration 0.1M, Withdrawal Rate 4cm/min			
Results			
Confimation Run #	Omega FWHM (°)	Phi FWHM (°)	Phase Ratio	Epitaxial #
1	12.45	12.19	344.0	6.49
2	10.60	10.80	727.0	18.19
3	10.24	10.81	708.0	18.31
4	11.63	11.34	567.0	12.33
5	10.52	11.58	662.0	15.57
6	12.43	12.49	418.0	7.70
7	12.64	11.84	464.0	8.87
8	15.01	17.42	172.0	1.88
Average	11.94	12.31	507.8	11.17
Standard Deviation	1.47	2.01	182.0	5.55
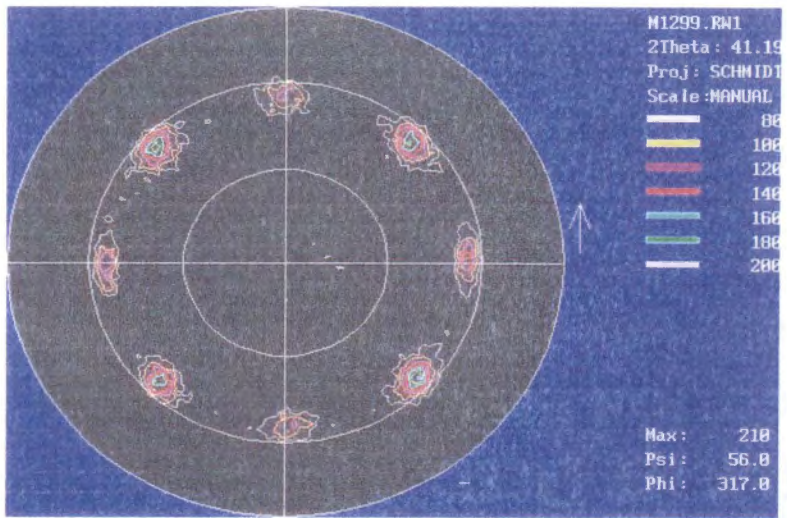
Figure 4.7 (111) Pole Figure of LaAlO$_3$ on Ni

Note: Poles at 45°, 135°, 225°, 315° correspond to (100) [001] oriented material.

Poles at 0°, 90°, 180°, 270° corresponds to in-plane twin (110) [001].
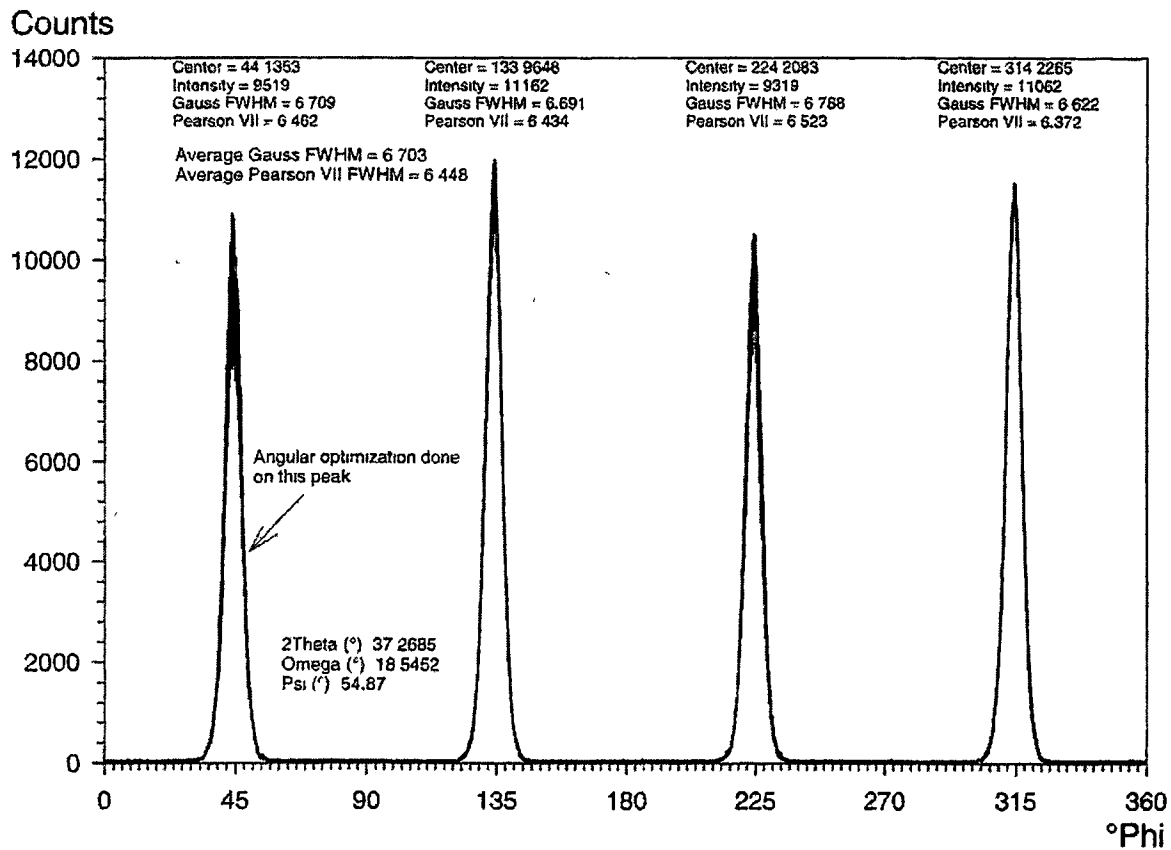
Figure 4.8 (111) NiO Phi Scan

Note. Sample (N103) Annealed in O_2 for 20 seconds.
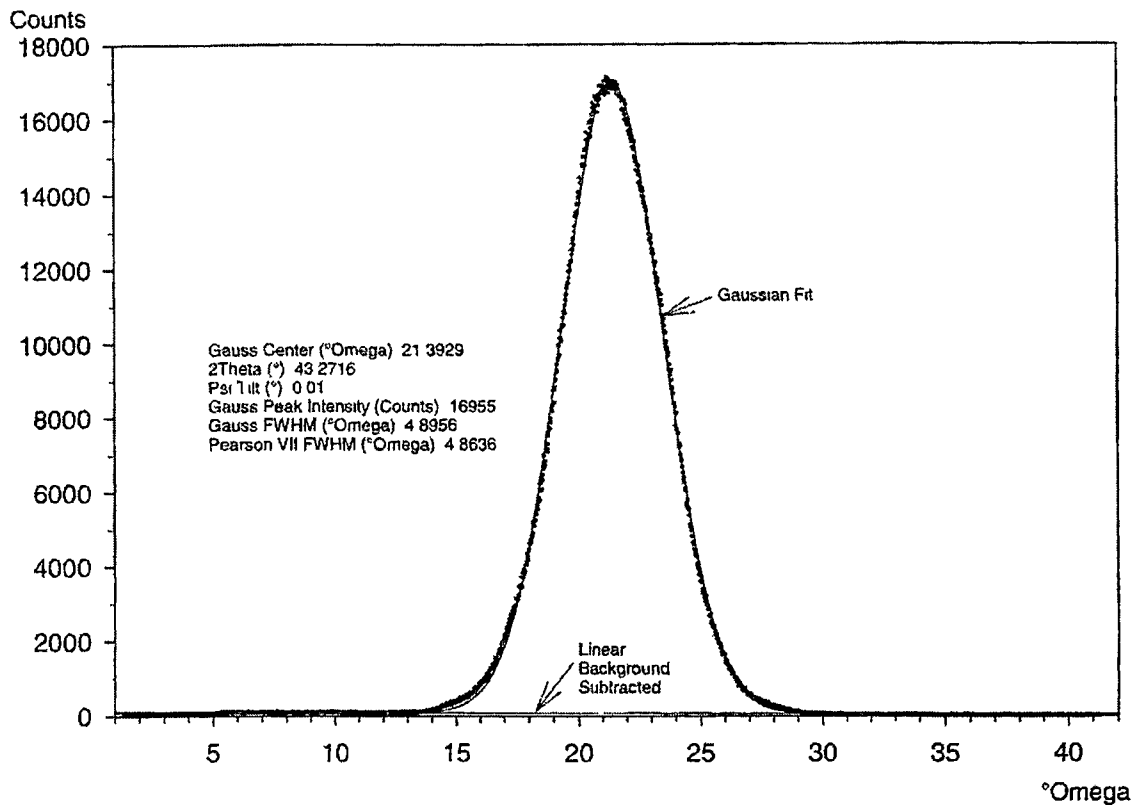
Figure 4 9 NiO (200) Omega Scan

Note: Sample (N103) Annealed in O_2 for 20 seconds.
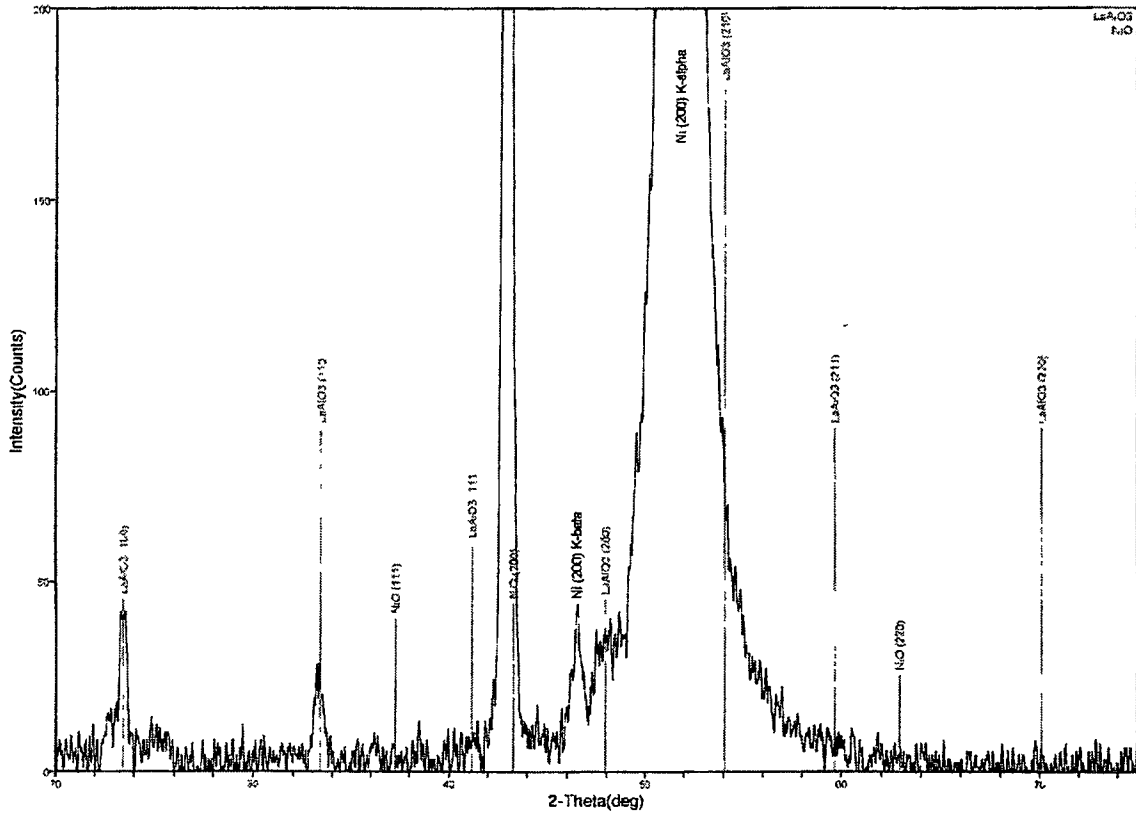
Figure 4.10 Phase Scan of Cube Textured NiO Coated with LaAlO₃

Note: Sample (N103) Annealed in O₂ for 20 seconds.
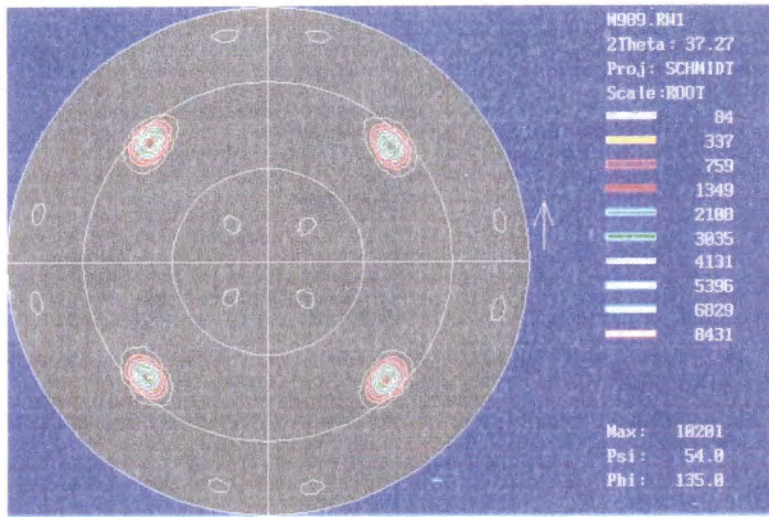
Figure 4.11 (111) Pole Figure of NiO on Ni

Note: Poles at 45°, 135°, 225°,315° correspond to NiO (100)[001]

Other poles are reflection of (212) [212] twin of cube texture.

Sample (N103) Annealed in O_2 for 20 seconds.

was coated and thermally processed at 950-1150 °C on the NiO substrates. Phase scans reveal that samples processed at 1150°C no longer have NiO(100) peaks, while samples at temperatures below 1150°C still have NiO(100). The NiO may have decomposed or reverted to an amorphous state at 1150°C.

Table 4.11, page 98, shows the results of $LaAlO_3$ omega scans and phi scans for NiO substrate samples. The mean values of phi and omega scans for all the processed samples were only 14.60° and 17.41° respectively which is significantly higher than those obtained on Plastronic "A" nickel. The poor results may be caused by the inclusion of $LaAlO_3$ atoms in the NiO matrix. Some of the samples showed signs of enlarged d-spacing through peak shifts on phase scans. According to Marvis White, this suggests the inclusion of other atoms (possibly $LaAlO_3$) within the NiO matrix thereby increasing its d-spacing. This shifting may introduce further mismatch between the $LaAlO_3$ and the NiO and could account for the poor results.

Additional amounts of oxygen were added during heat treatment of the $LaAlO_3$ coated NiO/Ni samples. The goal was to simulate processing in an air environment. However, the addition of oxygen by 5 volume % volume made only the NiO peak grow and the $LaAlO_3$ phase scan peaks became undetectable. The poor omega, phi, and phase ratio values in addition to inability to offer a benefit of eliminating special processing atmosphere suggest that textured NiO may not offer a feasible alternative to just the cube textured nickel substrate.

Table 4.11 Results for LaAlO$_3$ on Cubic Textured NiO Substrate

Sample ID	Phi FWHM (°)	Omega FWHM (°)
K27	13.70	16.35
K28	17.82	21.37
K29	13.04	13.80
K30	12.29	14.51
K24	11.12	17.21
K31	17.73	20.91
K32	16.47	17.69
Averages	14.60	17.41

LaAlO$_3$ on Resistively Annealed Plastronic Nickel

It was intended for the resistive annealing time to be the eighth factor in the

Taguchi L12 screening design. However, mechanical failure of the diffusion pump made

it impossible to include resistive annealing parts in the screening design matrix.

Recrystallization was accomplished as previously stated during the thermal treatment

after LaAlO$_3$ coating.

Surface Roughness Measurements with Optical Profilometer

Surface roughness measurements were made for the unannealed Plastronic "A"

nickel, electropolished Plastronic "A" nickel, Plastronic "B" nickel that was resistively

annealed for 1 hour and for 20 ½ hours, NiO on Plastronic "B" nickel, and LaAlO$_3$

coated nickel samples. Tables 4.12-4.17, pages 100-105, show the results for each type of

sample and Table 4.18, page 106, shows the comparison of all the results. In Tables 4.12

- 4 17, each cell represents a reading taken at a different point on the sample or on

another sample prepared in the same way.

The unannealed Plastronic "A" had less roughness than those samples annealed

at 1 and 20½ hours The greater surface roughness may be explained by grain boundary

grooves. In a grain boundary grooving study on cube-textured nickel by Conrad Simon,

grain boundary groove depth was shown to increase with time in nickel samples annealed

above 800°C (Simon, 1999) Samples resistively annealed at 55 amps or higher typically

Table 4.12 Surface Roughness Results for Plastronic "A" Nickel

Ra	Units	Ra	Units
0.497	Microns	0.439	Microns
0.485	" "	0.446	" "
0.455	" "	0.433	" "
0.290	" "	0.363	" "
0.288	" "	0.391	" "
0.373	" "	0.414	" "
0.451	" "	0.397	" "
0.362	" "	0.393	" "
0.359	" "	0.349	" "
0.304	" "	0.540	" "
0.924	" "	0.335	" "
0.432	" "	0.345	" "
0.542	" "	0.328	" "
0.361	" "	0.327	" "
0.400	" "	0.382	" "
0.425	" "	0.481	" "
0.374	" "	0.632	" "
0.363	" "	0.357	" "
0.500	" "	0.596	" "
0.465	" "		
Average			
0.426	Microns		
Standard Devation			
0.114	Microns		

Note: Each cell represents a reading taken at a different point on the sample or on another sample prepared in the same way. See page 59 for definition of Ra.

Table 4.13 Surface Roughness Results for Polished Plastronic "A" Nickel

Ra	Units	Ra	Units
0.882	Microns	0.541	Microns
0.878	" "	0.257	" "
0.921	" "	0.230	" "
0.970	" "	0.243	" "
0.630	" "	0.312	" "
0.526	" "	0.437	" "
0.514	" "	0.461	" "
0.627	" "	0.457	" "
0.720	" "	0.377	" "
0.660	" "	0.614	" "
0.661	" "	0.565	" "
0.702	" "	0.568	" "
0.546	" "	0.453	" "
0.440	" "	0.469	" "
Average			
0.559	Microns		
Standard Deviation			
0.197	Microns		

Table 4.14 Surface Roughness Results for Short-Term Annealed Plastronic "B"

Ra	Units	Ra	Units
0.459	Microns	0.780	Microns
0.950	" "	0.360	" "
1.500	" "	0.354	" "
1.200	" "	0.532	" "
1.200	" "	0.731	" "
0.760	" "	0.469	" "
1.700	" "	0.258	" "
1.400	" "	0.507	" "
2.100	" "	0.932	" "
1.300	" "	0.470	" "
1.200	" "	1.200	" "
0.760	" "		
Average			
0.9	Microns		
Standard Deviation			
0.5	Microns		

Note: Samples were resistively annealed for 1 hour.

Table 4.15 Surface Roughness Results for Long-Term Annealed Plastronic "B" Nickel

Ra	Units	Ra	Units	Ra	Units
0.55	Microns	0.81	Microns	0.84	Microns
0.97	" "	0.69	" "	0.72	" "
2 00	" "	0.56	" "	0.93	" "
1.88	" "	0.64	" "	0.55	" "
1.27	" "	0.59	" "	1.09	" "
1.68	" "	0.89	" "	0.80	" "
0.84	" "	0.73	" "	1.05	" "
1 49	" "	0.49	" "	0.61	" "
1.72	" "	0.62	" "	1.07	" "
0.95	" "	0.68	" "	0.58	" "
1.12	" "	0.56	" "	0.94	" "
0.77	" "	1.16	" "	1.34	" "
0.67	" "	0.80	" "	1.31	" "
0.87	" "	0.74	" "	1.07	" "
1.05	" "	1.19	" "	0.76	" "
2.04	" "	1.61	" "	2.35	" "
2.03	" "	0.69	" "	0.61	" "
2.43	" "	0.80	" "	0.53	" "
0.86	" "	0.81	" "	0.59	" "
0.62	" "	1.31	" "	0.91	" "
0.84	" "	0.66	" "	1.33	" "
1.15	" "	0.77	" "	1.09	" "
1.65	" "	1.12	" "	1.78	" "
0.98	" "	1.23	" "	0.86	" "
0.86	" "	0.66	" "	0.47	" "
0.87	" "	0.63	" "	0.79	" "
0.77	" "	0.57	" "	0.72	" "
0.93	" "	1.08	" "	0.96	" "
0.92	" "	0.80	" "	1.11	" "
0.50	" "	0.75	" "	1.18	" "
0.70	" "	0.74	" "		

Average
0.98   Microns
Standard Deviation
0.42   Microns

Note: Samples were resistively annealed for 20 1/2 hours.

Table 4.16 Surface Roughness Results for Cube Textured NiO Samples

Ra	Units
0 98	Microns
0 86	" "
1 33	" "
1 24	" "
1 08	" "
1 15	" "
0 67	" "
0 89	" "
0 69	" "
1 02	" "
1 24	" "
0.97	" "
1 29	" "
Average	
1 03	Microns
Standard Deviation	
0 22	Microns

Table 4.17 Surface Roughness Results for LaAlO$_3$ Coated Samples

Ra	Units	Ra	Units	Ra	Units
2.32	Microns	0.64	Microns	1.56	Microns
1.41	" "	0.85	" "	1.83	" "
0.77	" "	2.14	" "	1.47	" "
2.71	" "	2.69	" "	1.95	" "
3.78	" "	0.83	" "	1.52	" "
1.77	" "	0.34	" "	1.98	" "
2.77	" "	0.43	" "	1.21	" "
1.63	" "	0.35	" "	2.63	" "
1.04	" "	0.75	" "	1.89	" "
1.40	" "	0.44	" "	2.13	" "
1.72	" "	1.14	" "	1.09	" "
1.61	" "	3.57	" "	2.69	" "
1.75	" "	3.72	" "	2.15	" "
1.98	" "	2.99	" "	2.33	" "
2.53	" "	1.33	" "	3.13	" "
1.05	" "	2.53	" "	1.79	" "
1.43	" "	2.95	" "	2.41	" "
2.09	" "	1.87	" "	0.77	" "
2.08	" "	1.90	" "	1.02	" "
3.80	" "	1.73	" "	2.29	" "
1.72	" "				
Average		1.84	Microns		
Standard Deviation		0.80	Microns		

Note: Conditions for LaAlO$_3$ coating were oven temperature of 1150°C, oven time of 1

hour, oven atmosphere of 4% hydrogen in argon, degree of hydrolysis of 1.3, withdrawal

rate of 4 cm/min, and samples were polished.

Samples used were CON1 through CON4.

Table 4.18 Comparison of Surface Roughness for Various Substrates

Sample Type	Average Ra	Units	Standard Deviatio	Units
Unannealed "A"	0.43	Microns	0.11	Microns
Unannealed "A" & Polished	0.56	" "	0.20	" "
Short Term Annealed "B"	0.90	" "	0.50	" "
Long Term Annealed "B"	0.98	" "	0.42	" "
NiO on Ni	1.03	" "	0.22	" "
Coated with LaAlO$_3$	1.84	" "	0.80	" "

reached temperatures in excess of 1200°C. In samples processed at for 20½ hours, the grain boundaries became highly noticeable on the optical profilometer scans. The nickel oxide and coated LaAlO₃ samples showed the greatest surface roughness. These results may be compromised because of the different effects dissimilar materials have on light. The following is taken from the manufacturer's manual.

"A thin film is considered transparent, and it must have a substrate layer below it. Because the (thin) film is transparent, there is an additional phase change upon reflection from the underlying substrate."

This suggests that the signal returned to the optical profilometer has been modified in an unaccounted way by either the LaAlO₃ thin film or the NiO film. The optical profilometer provides a dissimilar material analysis option. However, a portion of the substrate has to be present in the scan. This would only allow regions near the meniscus line of coating to be examined on LaAlO₃ coatings. This region has been shown to be a thick region nonrepresentative of larger constant thickness region as seen away from the meniscus region by Vineet Lasrado (1998).

Finally, unannealed samples that were polished did not have lower R_a values than those that were polished The effectiveness of the polishing is thus in question. The brightness originally observed when the polishing was optimized may be due to etching away of the surface contaminants. As a result, the surface roughness factor in the Taguchi L12 matrix may not really be a measure of the surface roughness but probably that of removal of surface material and contaminants. Surface contaminants have been

107

mentioned as a possible negative factor to the epitaxial growth (Shoup et al. 1998). This may explain the positive effect the polishing/etching had on the omega FWHM and the phase ratio

CHAPTER 5

ECONOMIC ANALYSIS OF SOL-GEL BASED FILM COATING

SCHEME

HTSC Production Objective and Goals

The production objectives of a commercial process to produce HTSC were based on the work done by Dr. James Chapman on MOCVD, e-beam, and PLD processes (see Chapman, 1998, 1999). The production objectives were 18,000 kilometers of HTSC conductor tape per year for ten years at a plant capacity factor of 65%. A cost goal for the production of the conductor material was set at $10.00/kA-m. Achieving this goal would be necessary for the superconducting materials to replace copper in large-scale applications in the electrical industry (Muehlhauser, 1997).

HTSC Conductor Scheme

It was assumed that RABiTS nickel substrates will be produced in ten centimeter width by one kilometer length foil. As a final step the tape would be slit into one centimeter width pieces and cut to customer specified lengths. The RABiTS layer architecture was assumed to be 38.1 microns thick nickel followed by double-sided coating of one micron thick $LaAlO_3$ buffer layer and two micron thick YBCO layer on each side. J_c of 10^6 A/cm^2 for applications involving no external magnetic fields and J_c of

10^5 A/cm^2 for applications in a perpendicular five tesla magnetic field were assumed for HTSC quality performance.

Sol-Gel Processing Scheme

Figure 1.1, page 4, provides a process flow diagram of a sol-gel based film coating process to produce high T_c superconductors on RABiTS nickel. This sol-gel processing scheme assumed that the precursor solution and RABiTS nickel will be produced on-site in addition to the final product. The precursor preparation scheme assumed that the raw materials, metal alkoxides and organic solvents, would be purchased from the suppliers and then transformed into precursor sols on-site. These on-site steps would involve dissolving metal organics in solvents, mixing of metal organic solutions, conversion of metal organics to usable form, and partial hydrolysis of metal organics to form precursor sols. The conversion process for this study assumed that the metal alkoxides require ligand substitution by reactions with organic solvents at their bubble point temperatures

RABiTS nickel production on-site would involve rolling and annealing of the nickel tape. The RABiTS nickel will be rolled into length of one kilometer and ten centimeters in width and stored on spools. The material will be batch annealed at 800°C for two hours to promote sharpening of the nickel textures

The final production of the HTSC conductors would involve a continuous dip-coating scheme followed by thermal treatment. The RABiTS nickel is continuously drawn through the buffer layer sol-gel solution and then into a pyrolyzing unit. The

pyrolyzing unit will utilize excess amounts of oxygen and heat to combust the volatile

organic solvents into CO_x and NO_x gases. The gases are exhausted to downstream air

quality treatment units while the nickel is wound up on a spool. Figure 5.1, page 112,

shows a simple conceptual diagram of the process. These spools are then taken to retort

furnaces where they can be batch processed at high temperatures in controlled

atmospheres. The coating and thermal processing is again repeated for coating the

superconducting material layer. Then a passivation layer was assumed to be applied in an

similar fashion that that used currently on copper magnet wire. Finally, the multilayer,

coated conductor is slit as the very last processing step.

Capital Costs Associated with Precursor Solution Production

Precursor solution processing equipment was sized based on 100% capacity

factor. In addition, a 85% materials utilization factor was used to reflect losses of solution

through leaks, spills, evaporation, slitting of the conductor at final stage, and etc..

Thereby, the total amount of precursor solution required per year was calculated at

52,309 gallons of 0.1M $La[Al[OCH_2CH_2OCH_3]_6$ and 124,994 gallons of 0.026M

$Cu_3O_3Ba_2Y[OCH_2CH_2OCH_3]_7$. The Appendix gives the calculations used for the

equipment sizing and production requirements in this costing study. Equipment was

assumed to be operated on a batch mode. The number of batches per year was assumed to

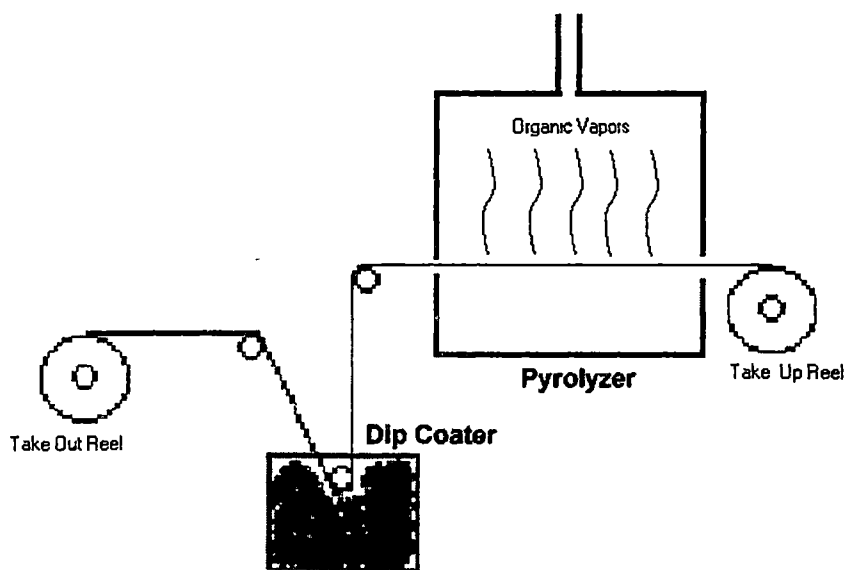be fifty-three or roughly once per week.

Figure 5.1 Continuous Dip-Coater

Based on these production assumptions the following processing equipment were assumed necessary for the production of the precursor solutions. Four 1,000 gallon, one 1,500 gallon, one 2,000 gallon, and one 2,500 gallon stationary mixing tanks would be needed. The four 1,000 gallon and the one 1,500 gallon stationary mixing tanks could be used as dissolvers for each of the metal alkoxides in their respective organic solvent. The 2,000 and the 2,500 gallon tanks could be used as the mixing units, where the solution would also be partially hydrolyzed. They could also act as an intermediate storage from which the continuous or batch dispension to the dip coaters could occur. All these stationary mixing tanks would continuously churn the materials at low speeds through agitation devices like shaft-mounted, off-set blades. Two additional 10,000 gallon carbon steel storage tanks would be used to unload and store solvent the from tanker trucks.

The metal alkoxides are assumed to be purchased in a pure form. That is yttrium isopropoxide, barium isopropoxide, lanthanum isopropoxide, and aluminum sec-butoxide are assumed to be purchased from out-side sources and no additional purification would be necessary. However, the metal alkoxides will be converted to metal 2-methoxyethoxides by ligand exchange with 2-methoxyethanol at bubble point conditions. Thereby, two batch reactors with agitators and heating jackets will be necessary to carry out the reaction. Two 2,000 gallon batch reactors are assumed to be used to perform the reflux reactions in the yttrium/barium and lanthanum/aluminum alkoxide systems.

Y, Ba, La isopropoxides and Al sec-butoxide ligand substitution reactions with 2-methoxyethanol would produce discernable amounts of isopropanol and butanol. Based on the vapor pressure data posted at the NIST Chemistry WebBook site on the Internet, the relative volatility of isopropanol/2-methoxyethanol system is 1.9 and the butanol/2-

methoxyethanol system is 1.1 at atmospheric pressures and respective, bubble point temperatures. (NIST, 2000) This suggests that the isopropanol but not butanol may be economically recoverable using vapor-liquid equilibrium methods such as distillation. Ninety percent IPA (isopropanol) trades for roughly $0.26/lb according to the Purchasing Online's bulk chemicals listing (Purchasing Online, 2000). Assuming 100% conversion, there would be 5 mol % IPA in the barium/yttrium reflux system and 2.5 mole % IPA in the lanthanum/aluminum reflux system in the product stream. This translates into only $50,000 over a ten year life of the plant used aforementioned costs. However, it is unlikely that this resale value will cover the cost of recovery of IPA. However, if some solubility problems should arise in regards to the contamination of 2-methoxyethanol, then the removal of IPA may be warranted. This was assumed in this case study, and a small, sieve-tray distillation column was designed for mounting on a batch reactor. The batch reactor would act like a reboiler and the system could be kept in total reflux until the reaction had progressed to a desired conversion.

The capital cost of the processing equipment was estimated based on the purchase costs. Purchase prices were obtained from charts and "rules of thumb" in Peters' and Timmerhaus' Plant Engineering and Economics for Chemical Engineers (1991). Prices were adjusted for inflation by using the Marshall and Swift index for all industries ("Chemical Engineering", 2000). Installation and other additional costs were assessed using correlations from Peters and Timmerhaus on fluid processing plants (pp. 171-183). Table 5.1, page 115, shows a breakdown summary of the capital cost associated with the precursor solution processing equipment. The majority of the total purchase price for equipment was due to the reactor vessel consisting of a glass-lined, carbon steel shell, a

Table 5.1 Capital Costs Associated with Precursor Solution Production

Item	Purchase Price Cost
Mixing Tanks	$111,000
Solvent Storage Tanks	$48,000
Batch Reaction Vessels	$202,000
Distillation Columns Shell Fabrication	$20,000
Sieve Trays & Associated Structural Parts	$23,000
Condensors	$6,000
Total Purchase Price	$410,000
Additional Items	Cost
Physical Installation of Equipment (55% purchase price)	$225,500
Associated Piping Labor & Materials (66% of purchase price)	$270,600
Electrical Installation (10% of purchase price)	$41,000
Basic Instrumentation & Controls (13% of purchase price)	$53,300
Insulation Costs (8% of purchase price)	$32,800
Total Additional Costs	$623,200
Total Capital Cost of Precursor Processing Equipment	$1,033,200

Note: Precursor Solution includes both $LaAlO_3$ and YBCO.

10 hp, 120 rpm, agitator, a heating jacket, and a thermometer well. The total capital cost of the precursor processing equipment was estimated to be about $1,000,000.

Capital Costs Associated with the Direct Production of HTSC Coated Conductor Tape

The direct production cost of HTSC coated conductor tap entails RABiTS nickel production, two sol-gel coating layers, thermal treatment for each layer, and some final packaging steps including slitting and the addition of a passivation/insulation layer. Table 5.2, page 117, shows the various costs associated with the direct production of the HTSC coated conductor tape.

RABiTS nickel is produced from purchased high purity nickel that is biaxially rolled and annealed to give cube-textured grain alignment. The rolling mill was adopted from Chapman's work (1998, 1999). The mill has ten stages and each stage reduces the strip by twenty-five percent (Chapman, 1998). All together, 30-mil-thick nickel is reduced by ninety-five percent (Chapman, 1998) to 1.5 mils. The rolling mill's cost includes a control system that monitors and controls surface roughness and thickness (Chapman, 1998). The batch-annealing furnace was also adopted from Chapman (1998, 1999). It's capabilities included 600 kilometer per batch and operation in a protective, forming gas atmosphere (Chapman, 1999). The cost estimates for the direct production of HTSC coated conductor tape is shown in Table 5.2, page 117.

Coating of the RABiTS nickel with LaAlO$_3$ and YBCO is accomplished by a continuous, dip-coating apparatus. This apparatus is followed in-line by pyrolysis unit

116

Table 5.2 HTSC Direct Production Capital Costs

Items	Capital Costs
Rolling Mill	$259,300
Heat Treatment Facility for RABiTS Nickel	$443,000
Continuous Dip-Coaters/VOC Pyrolyzing Units	$12,960,000
Retort Furnaces for Crystallization	$230,720
Enamel Dip & Dry Insulation Process	$1,000,000
Slitting Machinery	$300,000
Total Capital Cost	$15,193,020

which would remove and combust the toxic solvents. Figure 5.1, page 112, illustrates the concept of a continuous dip-coater followed by an in-line pyrolyzer. The tape is fed from the take-out reel, then drawn through the sol-gel solution vertically, then taken directly through a pyrolyzer, and then is collected on a take-up reel. Cost estimates for the continuous, dip-coating systems for $LaAlO_3$ and YBCO sol-gel solutions are shown in Table 5.2, page 117. The cost estimate for the dip-coating system was provided by Matt Vega, Chemat Inc. (Vega, 2000). An entire system of dip-coaters was sized to process 5.27 meters per min, which is the minimum continuous production rate to meet the yearly production goals (2,769,231 meters, preslit). Line speeds were estimated to apply the desired thickness in one dip per coating from data in Vineet Lasrado's work. That data suggest that at 3 cm /min, a film thickness of 1200 angstroms is deposited. The appendix shows the calculations of the film thickness based on this design's withdrawal rate.

The cost of the pyrolyzer was also gathered by Vega. The necessary pyrolyzer length for the aforementioned line speeds was estimated to be about eight feet. The pyrolyzer unit is capable of running at 400°C and metering in pure oxygen. Both costs (pyrolyzer & dip-coater) were then doubled to account for the additional units necessary to make up the time lost in loading, winding, unwinding, and unloading. According to Paul Kramer, Kramer Koatings Inc., the winding / unwinding would be a very time consuming task. (Kramer, 2000)

Retort Furnaces for crystallization of the thin-films were quoted by Dan Lipsi of Electra Products Company, Inc. (Lipsi, 2000). The retort furnaces were fitted with carts for loading and unloading of spools in protective atmosphere. Other capabilities include maximum operational temperature of 1150°C, safe operation with hydrogen atmospheres,

and multi-program control system. A standard retort furnace with working space of 16"
by 21" by 24" with above capabilities had a unit price of $32,000. Four units for YBCO
crystallization and one unit for $LaAlO_3$ crystallization were calculated as necessary in
Appendix C. Thereby, the total purchase cost with adjustments of 25% for physical
installation, 9% for insulation, and 15% for electrical installation, was $230,720 for the
retort furnace system

Final packaging of the coated conductor involves adding a passivation/insulation
layer and slitting to customer specified widths, which was assumed as one centimeter in
this study. The enamel dip and dry process in Chapman's study was used (1998, 1999).
This process was patterned after the one used in the making of copper magnet wire. The
slitting operation could be outsourced or performed in-plant. In regards to outsourcing of
the slitting operation, Wayne Etchells, Metlon Inc., had quoted $11.95 per spool. This
works out to an annual cost of $33,000 plus shipping. Over the ten-year plant life this
becomes at least $330,000. Whereas, John Smero, Metal Conversion Systems Inc.,
quoted only $300,000 for a light-gauge slitting machine capable of operating at several
hundred feet per minute. Thereby, it would probably be more economical to have the
slitting operation on-site than to outsource, and the in-plant equipment cost is shown in
Table 5.2, page 117.

<center>Facilities Related Capital Costs</center>

Table 5.3, page 120, lists all the capital costs associated with the facilities. These
facilities were assumed to be approximately similar to those used by Chapman (1998,

<center>119</center>

Table 5.3 Facilities Capital Cost

Additional Items	Capital Costs
Building	$3,720,000
Yard Improvements	$500,000
Electrical Substation	$1,000,000
Q/A Test Facility	$1,500,000
Emission Cleanup System	$250,000
Total Facilities Capital Cost	$6,970,000

1999). The building was sized at 100,000 ft^2 on 10 acres of land (Chapman 1998, 1999).

On-site facilities included a twenty-five megawatt, electrical substation and a quality

assurance laboratory with general purpose laboratory equipment including, XRD, SEM,

TGA, AFM, and a superconductivity testing device (Chapman 1998, 1999). The facilities

also accommodated for emission cleanup of pyrolyzer off-gases. Off-gases would mainly

consist of CO_x and NO_x with a limited number of non-combusted VOC. An emission

control device was assumed in accordance with Chapman's work (1999). This device

includes a stack-mounted flare for further VOC cleanup and a selective catalytic

reduction system to reduce nitrogen oxides (NO_x).

Total Capital Cost

The total capital cost is shown in Table 5.4, page 122. A couple of additional

factors were included to generate the total capital cost. Architect's and engineer's fee of

15% was added. Also, a project contingency of 20% was assessed on top of that subtotal.

Both factors were adopted from Chapman's work (1998,1999). A process contingency

was not directly included since it was assumed that the process was not undeveloped.

Manufacturing Costs

The manufacturing costs including utilities, maintenance, labor, and raw material

purchase, were figured on a yearly basis. Table 5.5, page 123 shows the yearly costs

Table 5 4 Total Capital Cost

Capital Components	Cost
Precursor Processing Equipment	$1,033,200
HTSC Direct Production Equipment	$15,193,020
Facilities	$6,970,000
Subtotal	$23,196,220
Architect's & Engineer's Fees (15%)	$3,479,433
Subtotal	$26,675,653
Contingency (20%)	$5,335,131
Total Capital Cost	$32,010,784

Table 5.5 Operating Costs

Item	Yearly Cost
Labor	$8,836,380
Raw Materials	$17,708,826
Utilities	$3,000,000
Maintenance (10% of Total Capital Cost)	$3,201,078
Total Manufacturing Costs	$32,746,285

associated with each of the four components. Utilities and maintenance costs were assumed to be similar to those in Chapman's work since the facilities are roughly considered to be the same That is that maintenance was 10% of capital cost, and utilities were $3,201,078 (Chapman 1998, 1999).

Labor costs were assumed to be $8,836,380. This cost was assumed to be roughly in the same order of magnitude as that presented in Chapman's work on MOCVD (Chapman 1998, 1999). This base case assumed 157 employees with an average wage of $25 per hour plus 26% for fringe benefits as adopted from Chapman's assumptions (1998, 1999). An example of cost calculation is shown in the appendix. The most laborious tasks at such a facility may be associated with handling of spools. That is the loading and unloading of spools from the dip coaters and from the furnaces.

Individual raw material costs are listed in Table 5.6, page 125. Quotes for the unit prices for the solvents, triethanolamine and 2-methoxyethanol (methyl cellosolve), came from Union Carbide and Brown Chemicals respectively (Smucker, 2000; Brown, 2000). Metal alkoxides prices were estimated from small quantity prices given in an Alpha Aesar's 1999-2000 catalog by scaling to larger quantities using the following function.

$$Unit\ Price = aR^b$$

, where a&b are constants and R is the amount of material purchased

The Appendix shows the calculations performed with Microsoft Excel's power series regression for aluminum sec-butoxide and lanthanum isopropoxide. Lanthanum, yttrium, and barium isopropoxide units cost were in excess of several thousand dollars

Table 5.6 Raw Material Costs

Raw Material	Purity	Amount (lbs)	Unit Price ($/lb)	Yearly Cost
Triethanolamine	99.0%	368,712	$0.59	$217,600
2-Methoxyethanol	99.4%	612,058	$1.45	$887,500
Lanthanum Isopropoxide	95.0%	9,445	$454.55	$4,536,400
Aluminum Sec-Butoxide	95.0%	7,359	$0.62	$4,600
Yttrium Isopropoxide	95.0%	4,886	$454.55	$2,223,000
Barium Isopropoxide	99.0%	9,002	$454.55	$4,095,900
Copper (II) Methoxide	98.0%	7,177	$417.18	$2,994,300
Nickel	99.9%	134,584	$17.36	$2,749,300
Oxygen	99.9%	776,435	$0.02	$17,600
Total Cost				$17,708,826

per pound. It is assumed that this is to costly for a commercial process and lanthanum isopropoxide, yttrium isopropoxide, and barium isopropoxide were instead assumed to have unit prices of $1,000 per kilogram or $454.55 per pound. This coincides with the base assumption that James Chapman made regarding the MOCVD precursors (1999). The sensitivity of this assumption is examined further in this chapter.

Other material costs include the gases: argon, hydrogen, and oxygen, and the price of high purity nickel Hydrogen and argon were used in batch processes, thereby the amounts were assumed to be small and consequently the price negligible in comparison with the other raw materials. The amount of oxygen was calculated assuming that three moles of oxygen would be needed for every mole of VOCs in the pyrolyzer. The unit cost of oxygen was assumed to be the same as that presented by Chapman (1999). The cost associated with oxygen is relatively small, and thereby, it is unlikely that variation in the 3:1 mole ratio will have significant impact on the production cost. Finally, the unit cost of high purity nickel was assumed to be the same as that presented in Chapman's work (1999).

Annual Capital Charge

The capital costs, shown in Tables 5.1-5.4, pages 115, 117, 120,122, incur an annual cost related to taxes, interest, depreciation, and money. The percentages of total capital cost for each charge component was adopted directly from Chapman's study (1998, 1999). Table 5.7, page 127 shows all the annual capital charge components and

Table 5.7 Annual Capital Charge Components

Annual Capital Charge Components	
Cost of Money (7.5%)	$2,400,800
Income Taxes (4.1%)	$1,312,440
Depreciation (10%)	$3,201,078
Other Taxes (2.8%)	$896,300
Working Capital (0.2%)	$64,000
Total (24.7%)	$7,906,664

their amounts. Depreciation was determined by straight-line method over ten years (Chapman, 1998, 1999).

Total Annual Cost & Product Cost

The total annual cost was the sum of the manufacturing costs plus the capital charges. The overall product cost was determined by dividing the total annual cost by the amount of coated conductor produced. This number was then divided by a performance factor of kiloamperes of critical current capacity. For base conditions the critical current capacity of the conductor was 400 amperes or 0.4 kiloampere. The product cost for the base case is shown in Table 5.8, page 129. The calculated product cost ($5.65/kA-m) meets the product cost goal of $10/kA-m for this base case Inherent to calculating the product cost for the base case were several key assumptions, as a result the sensitivity of product cost to them are examined in the following sections.

Sensitivity to Plant Capacity Factor

Figure 5.2, page 130 illustrates the variation of product cost with plant capacity factor. As the plant capacity factor reaches one, the production rate approaches the limit of the equipment size. Thereby, there is a reduction of excess capital, which translates into a lower annual capital charge that gradually reduces the product cost. The broadening out of the slope as the plant capacity approaches one suggests that the rising material costs begin to cut into the savings made by reducing excess capital expenditure.

Table 5.8 Product Cost

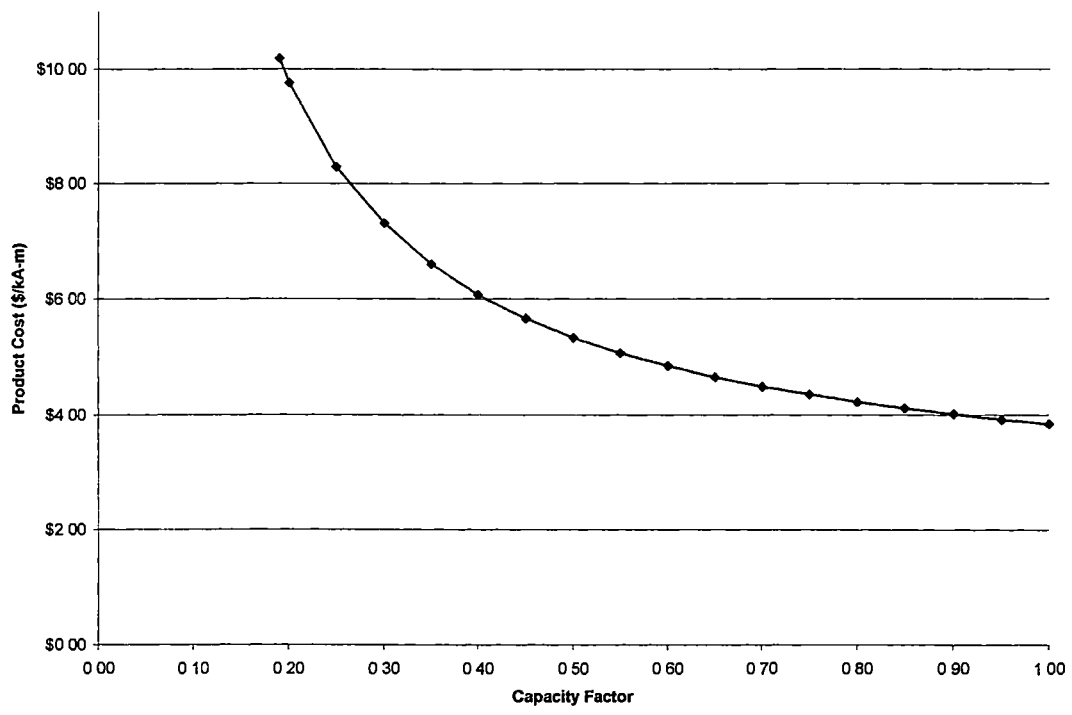| Total Annual Cost Components	
Manufacturing Costs	$32,746,285
Annual Capital Charges	$7,906,664
Total Annual Cost	$40,652,949
Annual Production (m)	18,000,000
Critical Current Density (kA)	0.4
Product Cost ($ / kA-m)	5.65

Figure 5.2 Product Cost Versus Plant Capacity Factor

130

At plant capacity factors of 0.25 or less, the product cost no longer meets the $10/kA-m objective.

Sensitivity to Raw Material Costs

One of the major assumptions in the base case is the cost of yttrium, barium, and lanthanum isopropoxides. Figure 5.3, page 132, shows the variation of the product cost with a collection of assumed values for the cost of these raw materials. At prices of $1750 per pound and greater, the product cost escalates above the product cost goal. On the other hand, when the price of the these precursors drops to $100 per pound then product cost is only $4.47/kA-m.

Sensitivity to Material Utilization Factor

Material can be lost through various ways including pipe leaks, slitting scrap, and human error. The material utilization factor represent the decimal form of the percentage of material that actually produces the final product. Figure 5.4, page 133 shows the variation of product cost with material utilization factor. When the amount of scrap or lost material is greater than 70%, then the product cost goal is no longer met. If all the material is utilized, which is an unrealistic goal, then the product cost becomes $5.29/kA-m.
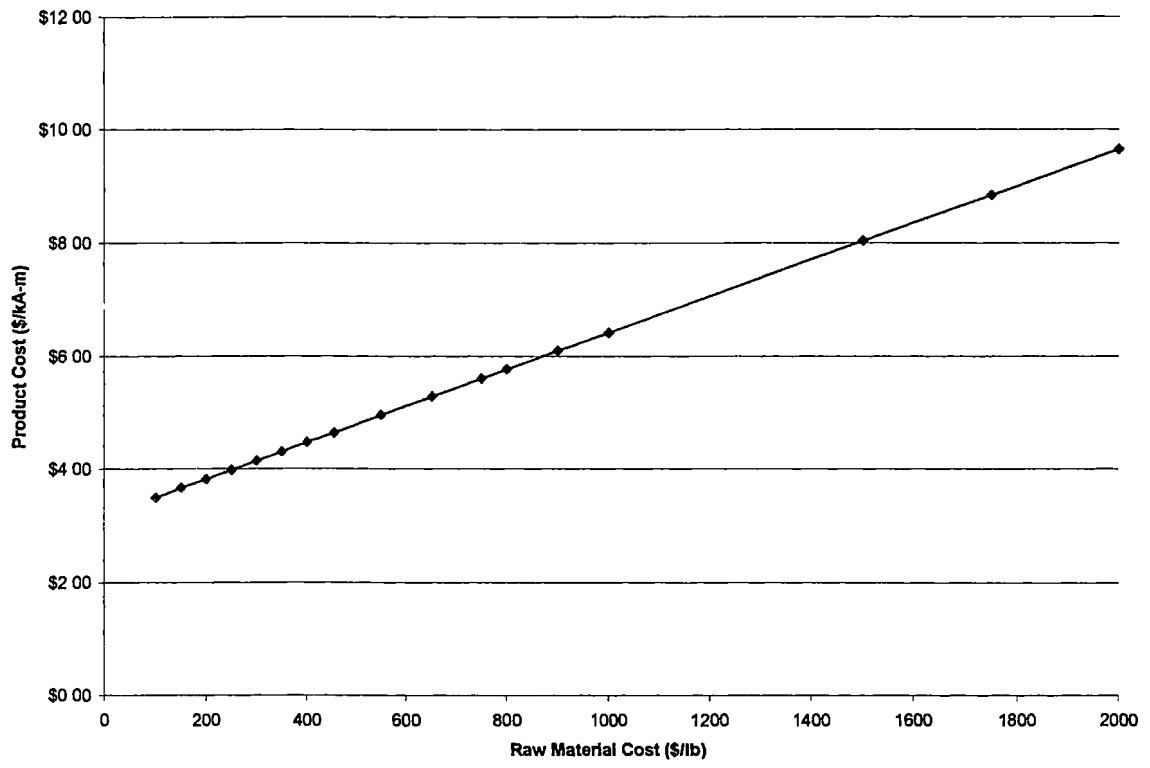
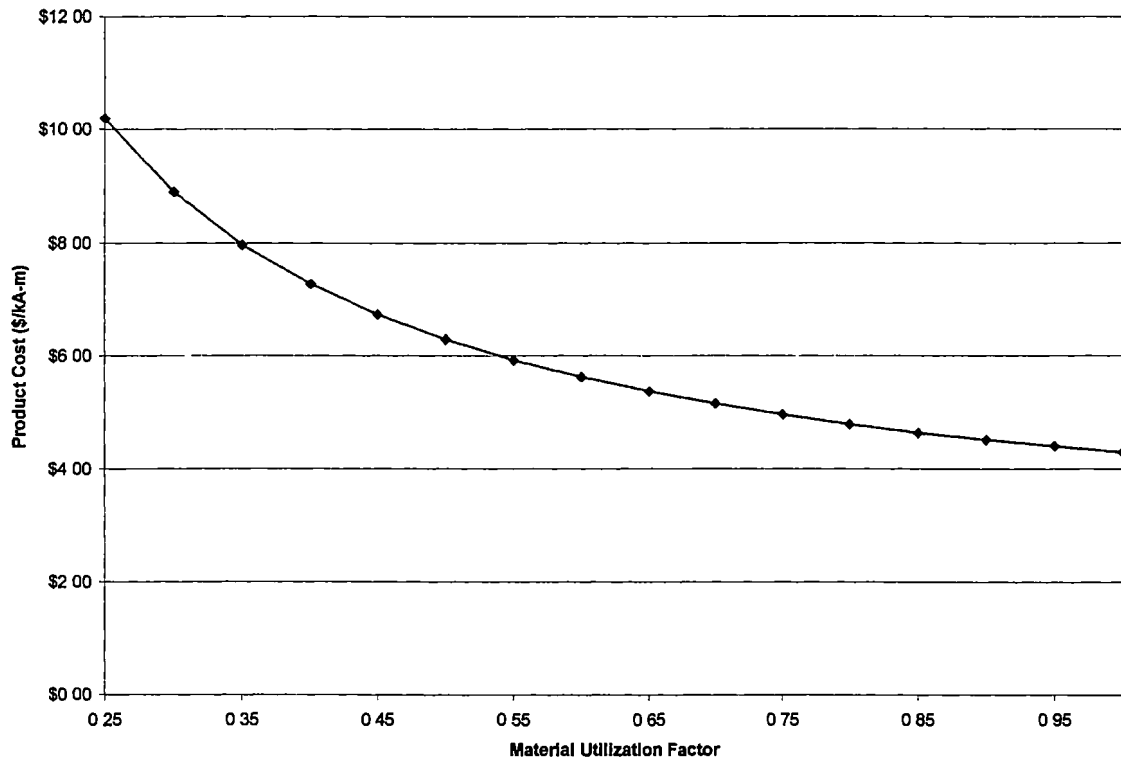Figure 5 3 Product Cost Versus Raw Material Cost

Figure 5.4 Product Cost Versus Material Utilization Factor

Sensitivity to Critical Current Density Performance

One of the basic underlying assumptions is that the critical current density of the superconducting material will be 1,000,000 A/cm^2. Figure 5 5, page 135, shows the variation of product cost with different critical current densities of the superconductor. Differences in the critical current densities can be caused by operating at different temperatures, by opposing magnetic fields, and by differing crystalline quality. Product cost sharply increases with declining critical current densities. At 500,000 A/cm^2, the product cost already exceeds the goal. At 100,000 A/cm^2 the product cost is $56 / kA-m. This would correspond to current density results obtained in five tesla fields.

Sensitivity to YBCO Thickness

The base case assumed a thickness of two microns of YBCO film per side on a double-sided tape. Thinner YBCO layers may become necessary, if good crystal quality cannot be demonstrated by the sol-gel method at such thicknesses. Figure 5.6, page 136 shows the variation in product cost with YBCO total layer thickness. The total layer thickness is the thickness of both sides of the tape. The product cost goal is exceeded at a total layer thickness of 1.75 microns or 0.88 microns per side
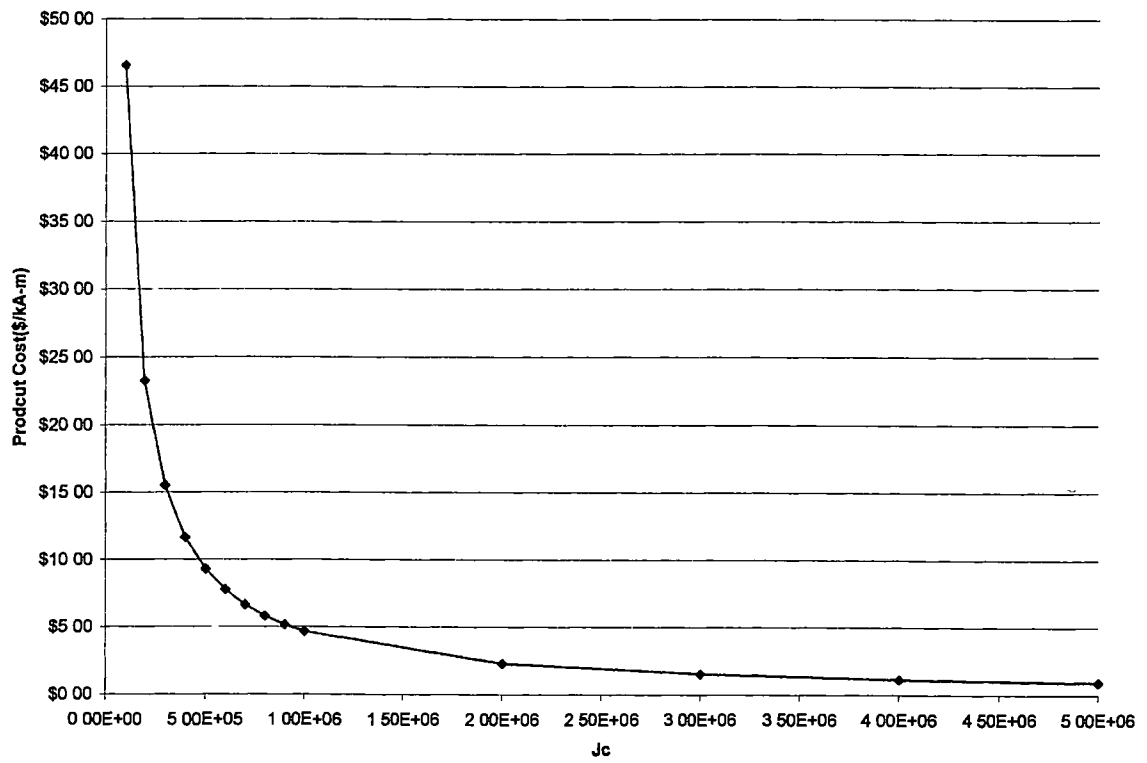
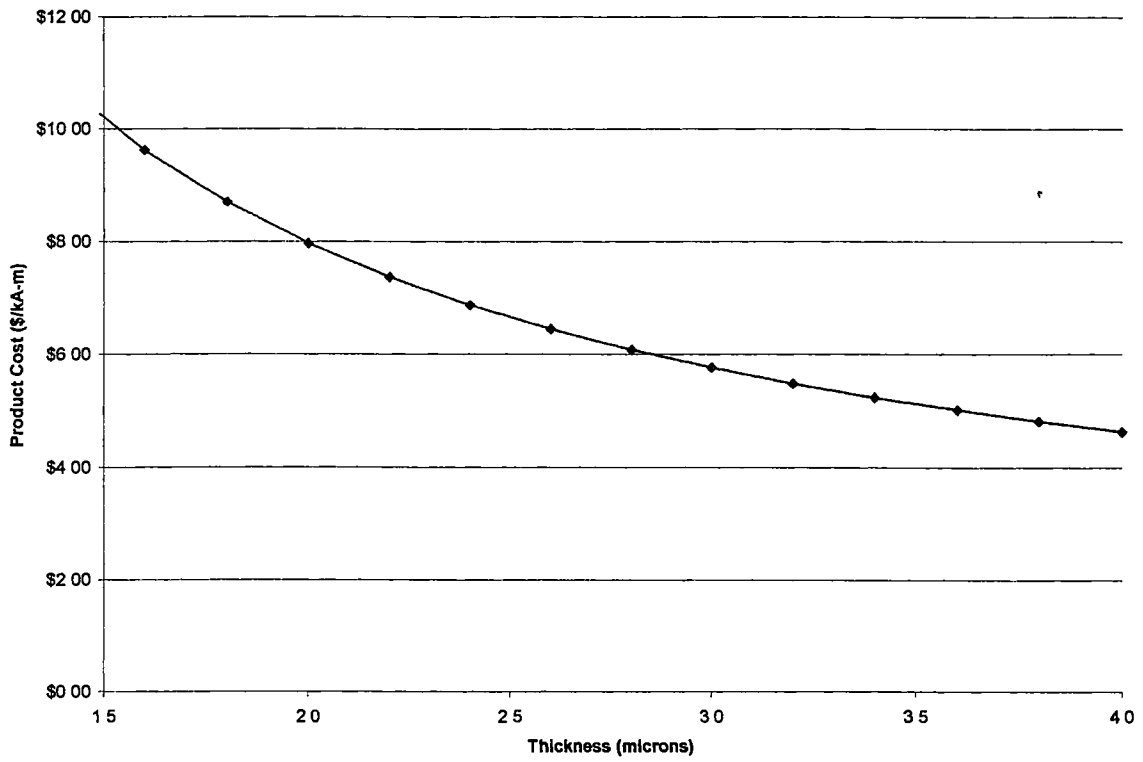Figure 5.5 Product Cost Versus Critical Current Capacity

Figure 5.6 Product Cost Versus YBCO Thickness

Sensitivity to Dip Coater Line Speed

Another important assumption to be examined is the speed of the dip coating lines. As the speed of the lines increase, then the number of lines needed to obtain the yearly throughput is decreased. Also, the number of dip coating units on each line decreases due to increased thickness per pass through a dip coating tank. However, the increased amount of material per pass may not compact sufficiently during pyrolysis and could effect the overall quality of the end product. Figure 5.7, page 138, shows graph of the product cost versus the dip coating line speed (withdrawal velocity). The product rises sharply as the withdrawal rate of the lines decreases to under 10 cm / min.

Alternative Sol-Gel Scheme

An alternative scheme for Sol-Gel was considered in regards to in-house or supplier-side precursor solution production. For the alternative scheme, YBCO and LaAlO$_3$ precursor solutions were assumed to be purchased from a supplier. The capital costs of the facility were adjusted for removal of the necessary equipment and labor. The cost of each precursor material was then calculated to achieve a product cost equal to $5.65 / kA-m (in-house precursor production). This cost was determined to be $168 per gallon or $13 per pound of precursor solution. The total raw material costs for this scheme could equal $19,361,492 for production of 115,247 gallons of precursor solution and still give a product cost of $5.65 / kA-m. At a precursor costs greater then $440 per gallon then the product cost exceeds the product cost goal.
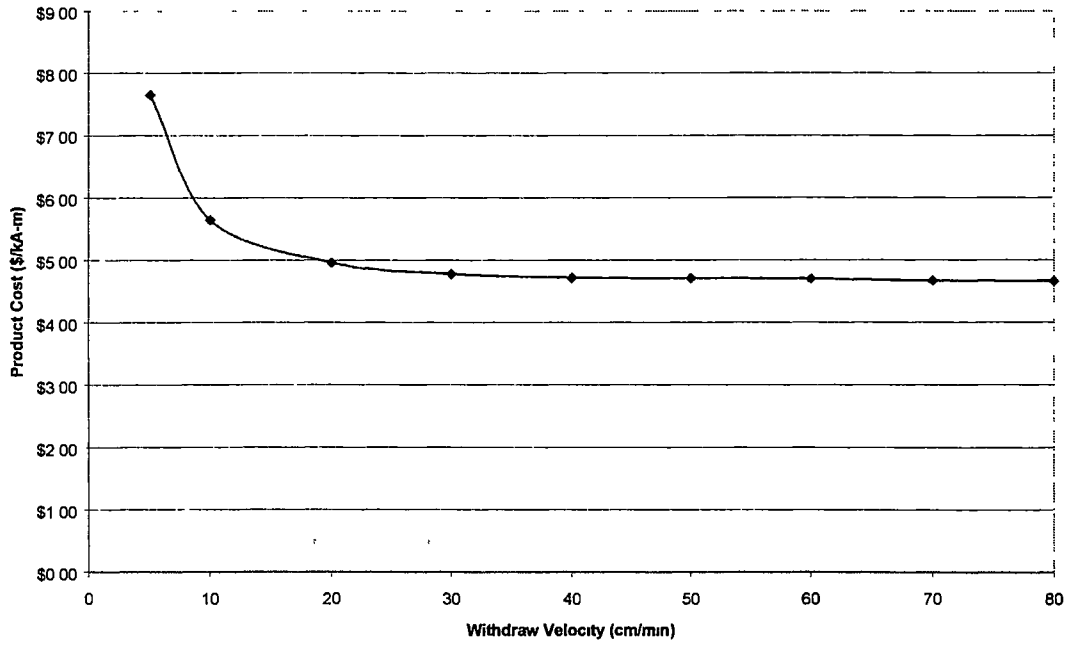
Product Cost Versus Velocity

Figure 5.7 Product Cost Versus Withdrawal Velocity

Comparison to Literature Findings

Table 5.9, page 140, lists the product costs of sol-gel base case (precursor production) along with the various literature findings for product costs based on the MOCVD, e-beam, and PLD schemes. These literature sources include the MOCVD, e-beam, and PLD with RABiTS studies performed by Chapman (1998,1999) and an e-beam process with IBAD performed by Robert Hammond (1996) of Stanford University. It is important to note that Hammond considered the HTSC layer to be only one micron thick and plant life was taken over only five years. With adjustments of a plant life to ten years and of a four micron thick layer, the product cost would adjust to $1.21 / m or $3.03 / kA-m. The product cost of the sol-gel base case is more expensive then e-beam scheme in Chapman's work (1998). However, it is less expensive than all the other schemes listed (MOCVD, e-beam on IBAD substrates, and PLD).

Table 5 9 Product Cost Comparison

Source	Current Work	(Chapman,1998)	(Hammond,1996)	(Chapman,1998)	(Chapman,1999)
Method	Sol-Gel	e-beam w / RABiTS	e-beam w / IBAD	PLD	MOCVD
Production Rate	18,000 km / yr	18,000 km / yr	18,000 km / yr	18,000 km / yr	18,000 km / yr
Annual Depreciation	10%	10%	20%	10%	10%
J_c (A/cm^2)	1×10^6	1×10^6	1×10^6	1×10^6	1×10^6
HTSC Thickness(m)	4×10^{-6}	4×10^{-6}	1×10^{-6}	4×10^{-6}	4×10^{-6}
Critical Current (A)	400	400	100	400	400
Total Capital Cost	$32,010,784	$30,950,110	$59,100,000	$88,185,588	$33,586,440
Material Cost	$17,708,826	$8,028,507	$3,600,000	$11,992,372	$18,935,247
Labor Cost	$8,836,830	$9,013,486	$1,800,000	$9,974,664	$7,142,000
$ / m	2.26	1.71	0.94	3.09	2.26
$ / kA-m	5.65	4.28	9 4	7.72	5.66

CHAPTER 6

CONCLUSIONS & RECOMENDATIONS

Conclusions with Regards to Experimental Findings

In conclusion, the effects of several processing parameters on epitaxial growth of LaAlO$_3$ on cube-textured nickel were successfully characterized using the Taguchi L12 screening experiments. The epitaxial growth was performed without annealing of nickel before coating. The characterization involved the development of a non-dimensional term, epitaxial #, to weigh together the in-plane and out-plane sharpness along with the composition of each crystal orientation. This characterization also involved the successful development of variance and response models that could be used to identify trends in the epitaxial # and to differentiate significant factors from insignificant ones. These models were developed on the sole basis of each experimental test's (phi, omega, and phase scans) results and then on the combined performance number (epitaxial #) to confirm the existence of trends in the responses and to locate the origins of them.

The experimental results suggested that the major factors in determining the epitaxial growth were the oven temperature, the solution concentration, the oven time, and the oven atmosphere. Increasing oven time and temperature while decreasing solution concentration and maintaining 4% hydrogen in argon produced higher epitaxial #'s. Eight confirmation runs were used to validate the above trends. Results showed marked improvement in all aspects (phi FWHM, omega FWHM, phase ratio). The phase scans showed the presence of one dominant peak of LaAlO$_3$(100). The average FWHM

141

of omega and phi were 11.94° and 12.31° These were comparable to the omega and phi

FWHM average values of 10 55° and 15.75° reported by Vineet Lasrado using the ORNL

supplied RABiTS nickel that had been annealed prior to dip-coating (Lasrado 1998). In-

plane twins were also found at half the intensity as the (100) oriented LaAlO$_3$. These

were also reported in work done by Vineet Lasrado.

The processing parameters that produced the improved results were as follows·

Oven Temperature = 1150°C   *Oven Time = 1 hr*

Oven Atmosphere = 4% H$_2$ in Ar   *Solution Concentration = 0 10 M*

Withdrawal Rate = 3 cm / min   *Degree of Hydrolysis = 1 3*

Surface Roughness = 0 (Electropolished State)

Samples that were electropolished prior to coating also had an identifiable trend

of improved epitaxial growth. Optical profilometer scans of surface roughness of

polished and unpolished scans were, however, inconclusive as to showing any

improvement in the surface roughness with the electropolishing work done here. Instead,

the improved results may have been linked to the etching away of possible surface

contaminants during the electropolishing process. In addition, optical profilometry

indicated that surface roughness increased between unannealed and annealed cube-

textured nickel samples. Ra values increased from 0.43 to 0.98 microns with annealing

times of twenty hours plus. This may be explained by thermal grain boundary grooves

developing during the annealing process.

Finally, the use of an intermediate cube-textured NiO layer was explored for processing in air and improved textures. The results indicated that it provided neither. At temperatures above 1050°C, the NiO layers broke down. In air, the NiO peaks grew on the phase scan, but the LaAlO₃ peaks disappeared. Some phase scans indicated an enlarging of the lattice parameters suggesting possible cross-contamination between the LaAlO₃ and NiO.

Conclusions with Regards to Process Costing Study

In conclusion, a sol-gel manufacturing cost study was successfully performed to determine the product cost ($/kA-m) and to compare it with the other production methods under comparable production rates and specifications. The product cost for the base case conditions is $5.65/kA-m. This is within the objective of $10/kA-m for economic feasibility for large scale electrical applications. In comparison to other processing methods explored by Dr. James Chapman of UTSI and Robert Hammond of Stanford University, the sol-gel based processing scheme has a product cost greater than e-beam with RABiTS substrate and very similar to MOCVD ($5.6/kA-m).

The sensitivity to several key assumptions including, material utilization, YBCO thickness, critical current density, plant capacity, withdrawal velocity, and raw material prices were examined. As capacity factor increases, the product cost decreases exponentially. Increasing the material costs leads to linear growth in the product cost. By increasing the material utilization factor, the product cost is decreased exponentially. Decreasing the critical current capacity leads to a sharp exponential rise in the product

143

cost. Decreases in the YBCO film thickness leads to higher product costs. The following limits for each sensitivity variable were identified to remain within the product cost objective.

YBCO thickness > 1 75 microns $J_c > 5x10^5$ *Material Utilization Factor > 0.30*

Plant Capacity Factor > 0.25   *Raw Material Price < $1750/lb*

The limit for withdrawal velocity was not determined, but the product cost was shown to rise exponentially to approximately $8/kA-m at withdrawal rate less than 10 cm / min.

Finally, the concept of having precursor solution not produced on site was explored. For unit prices of $168 per gallon then the product cost would remain unchanged. In order to meet the $10 / kA-m goal, the precursor price can not exceed $440 per gallon.

Recommendations

In terms of future characterization of epitaxial growth, it is important to investigate interaction terms when modeling the process. Time and temperature represent and obvious factors which may have some interactions. In addition, solution concentration may also form a three way interaction with these terms due to the fact that higher concentrations mean more material that has to be crystallized in the same period of time and under similar thermal input. Also of interest, might be investigations into

porosity of the buffer and HTSC layers prior to thermal treatment. Porosity could account for increases in thermal treatment time due to increased diffusion times for atoms to migrate to the growing epitaxial grains. They may also act as possible dislocation sites where the orientation of crystals forming around may be altered in orientation.

Lastly, in order to keep the sol-gel product cost within the goal, the most influential factors (labor and material costs) must be addressed. Savings in labor can result through further automation or reduction in the number of manual tasks needed. Adjustments to the width and length of processing tape dimensions should be considered to increase the amount of material on a spool. This would increase the ratio of process time to transition time for processes like dip-coating and batch thermal treatment for crystallization. Consequently, there will be a reduction in labor through less time and less number of sessions of manual loading and unloading of spools. Alternatives for the raw metal alkoxide precursor used (particularly lanthanum, barium, yttrium isopropoxide) should be considered This alternatives may include purchasing more fundamental forms of these materials (like Y_2O_3) and transforming and purifying in-plant. Since, the total capital expense for sol-gel was much lower than the other processes ($17 million to $30+ million), there is extra capital money that can be spent to try to reduce the costs. Finally, there may be concerns about decreasing product quality with increased throughput. It may be necessary to examine the maximum amount of material that can be put down per pass and still maintain epitaxial growth throughout the final product. The limitations of the material's crystallization rate combined with the nickel substrate's tendency to recrystallize back into random orientations will complicate the determination of the optimal settings for this process.

LIST OF REFERENCES

LIST OF REFERENCES

1. Sheahen, T. Introduction to High-Temperature Superconductivity. New York: Plenum Press, 1994.

2. Metha, S. Waukesha Electric Systems News Release, www.waukeshaelectric.com/weshtspr.htm, May 27, 1998.

3. Leftwich, G. Southwire Company News Release, http://www.southwire.com/news/082499a.htm, August 24, 1999.

4. Vollmar, W. 3M News Release, http://www.mmm.com/profile/pressbox/superc.html, 2000.

5. Chapman, J. Life Cycle Cost Study for Coated Conductor Manufacture by Electron Beam and Pulsed Laser Deposition Systems. Tullahoma: University of Tennessee Space Institute, July 1998. (Submitted under DOE contract # DE-AC22-95PC95231)

6. Chapman, J. Life Cycle Cost Study for Coated Conductor Manufacture by Metal Organic Chemical Vapor Deposition. Tullahoma: University of Tennessee Space Institute, July 1999. (Submitted under DOE contract # DE-AC22-95PC95231)

7. Tinkham, M. (1988). Phys. Rev. Lett., 61, 1658

8. Yeshuran, Y. & Malozemoff, A. (1988) Phys. Rev. Lett., 60, 2202.

9. Oak Ridge National Laboratory. (1998). Annual Report for Superconducting Technology Program for Electric Power Systems. 6-7.

10. Chudnovsky, E. (1990). Phys. Rev. Lett., 65, 3060.

11. Kwok, W. (1991). Phys. Rev. Lett., 67, 390.

12. Lasrado, V. Bench Scale Evaluation of Solution-Growth Based Techniques for Manufacturing HTS Wire/Tape. Master's Thesis. Knoxville: University of Tennessee, December 1998.

13. Cullity, B. Elements of X-ray Diffraction. Redding· Addison Wesley, 1978.

14. Brinker, C. & Scherer, G. Sol-Gel Science. San Diego: Academic Press, 1990.

15. Schmidt, S. & Launsby, R. Understanding Industrial Designed Experiments. Colorado Springs: Air Academy Press, 1998.

16. Oak Ridge National Laboratory. Annual Report for Superconducting Technology Program for Electric Power Systems. 1996. 11-12.

17. Simon, C. Experimental Study of the Effects of Annealing Time, Equilibrium Angle, and Absolute Misorientation Angle on Thermal Grain-Boundary Grooving in Cube-Textured Nickel. Master's Thesis. Knoxville: University of Tennessee, May 1999.

18. Shoup, S., Paranthaman, M., Beach, D., Specht, E., Lee, D., Kroeger, D. & Goyal, A. (1998) "Epitaxial Thin Film Growth of Lanthanum and Neodymium Aluminate Films on Roll-textured Nickel Using a Sol-Gel Method". J. Am. Ceram. Soc., 81, 3019-3021.

19. Muehlhauser, J. Ed. Research and Development Roadmap to Achieve Electrical Wire Advancements from Superconducting Coatings. Tullahoma: University of Tennessee Space Institute, July 1997.

20. Peters, M. & Timmerhaus, K. Plant Design and Economics for Chemical Engineers. New York: McGraw-Hill, 1991.

21. NIST Chemistry WebBook. http://webbook.nist.gov/chemistry/

22. Purchasing Online. http://www.manufacturing.net/cgi-

bin/frame.cgi/magazine/purchasing/depts/chemical.html

23. Fouhy, K. Ed Chemical Engineering. January 2000.

24. Underwood, A. J. V. (1948). Chem. Eng. Prog., 44, 603.

25. Gilliland, E. R. (1940). Ind. Eng. Chem., 32, 110.

26. Kramer, P., Kramer Koatings, Personal Communication, May 2000

27. Vega, M., Chemat Inc, Personal Communication, May 2000

28. Lipsi, D., Electra Products Inc., Personal Communication, April 2000

29. Etchells, W., Metlon Inc., Personal Communication, April 2000

30. Smero, J., Metal Conversion Systems Inc., Personal Communication, April 2000

31. Smucker, B., Union Carbide, Personal Communication, April 2000

32. Brown, P., Brown Chemicals, Personal Communication, April 2000

33. Hammond, R.H., (April 26, 1996) "YBCO Thick Film Manufacturing Issues:

Electron Beam Evaporation Controlled By Insitu Sensors" International

Conference on Metallurgical Coatings and Thin Films. San Diego, Ca.

Appendix

Calculation of Sol-Gel Precursor Solution Production Requirements

Basis

Yearly Rate of pre-spliced Conductor.	2,769,231 m
Conductor Width.	0.10 m
Capacity factor:	1
Crystal Density of $LaAlO_3$:	6500 kg / m^3
Crystal Density of $YBa_2Cu_3O_7$.	6220 kg / m^3
Molarity of $LaAlO_3$ Precursor.	0.10 M
Molarity of YBCO Precursor:	0.026 M
Material Utilization Factor:	0.85
$YBa_2Cu_3O_7$ Molecular Weight.	666.22 g / mol
$LaAlO_3$ Molecular Weight.	213.89 g / mol
$YBa_2Cu_3O_7$ Layer Thickness:	2×10^{-6} m
$LaAlO_3$ Layer Thickness:	1×10^{-6} m
# of Sides on Coated Conductor:	2

Volumetric Flowrate of Required Precursors Per Year Calculations

Mass of $LaAlO_3$ = $(2)*(1 \times 10^{-6}m)*(0.1m)*(2,769,231m)*(6500kg/m^3)$ = 3,600 kg

Mass of $YBa_2Cu_3O_7$ = $(2)*(2 \times 10^{-6}m)*(0.1m)*(2,769,231m)*(6220kg/m^3)$ = 6,890 kg

Moles of $LaAlO_3$ = $\dfrac{(3,600kg)*(1,000g/kg)}{(213.89g/mol)}$ = 16,831 mol

$$\text{Moles of YBa}_2\text{Cu}_3\text{O}_7 = \frac{(6,890\text{kg}) * (1,000\text{g/kg})}{(666\ 22\text{g/mol})} = 10,342 \text{ mol}$$

$$\text{Volume of LaAlO}_3 \text{ Precursor Required} = \frac{(16,831\text{mol}) * (0\ 26\text{gal/L})}{(0.1\text{mol/L}) * (0\ 85)} = 52,309 \text{ gal}$$

$$\text{Volume of YBa}_2\text{Cu}_3\text{O}_7 \text{ Precursor Required} = \frac{(10,342\text{mol}) * (0.26\text{gal/L})}{(0.026\text{mol/L}) * (0\ 85)} = 124,994 \text{ gal}$$

Distillation Column Sizing (LaAlO$_3$ Unit)

Basis

Yearly Number of Batch Runs·   53

Feed Per Batch·   47,376 moles 2-Methoxyethanol

1,121 moles Isopropanol (Light Key)

1,121 moles Butanol (Heavy Key)

Antione's Constants·

Component	A	B	C
Butanol	4.55	1,351.56	-93.34
Isopropanol	4.86	1,357 43	-75.81
2-methoxyethanol	5.06	1,853.56	-30 84

152

Molar Compositions & Flowrates:

Component	Distillate Mole Fraction	Bottoms Mole Fraction	Distillate Molar Flow Rate (mol / sec)	Bottoms Molar Flow Rate (mol / sec)
Isopropanol (LK)	0.99	0.0002	0 895	0 009
Butanol (HK)	0.01	0 0229	0 009	0 895
2-methoxyethanol	0.00	0.9769	0 000	38 207

Operating Reflux Ratio·   10

Operating Pressure   1.01 bar

Tray Efficiency: 80%

Bottom's Bubble Point Calculation

Antione's Vapor Pressure Equation $Ln\ P_i = A_i - \dfrac{B_i}{(C_i + T)}$, with units T (K), P (bars)

Distribution Coefficient $K_i = \dfrac{P_i}{P_{Total}}$, assuming Raoult's & Dalton's Laws

Bubble Point Equation $\displaystyle\sum_{i=1}^{\text{\# of Components}} y_i = \sum_{i=1}^{\text{\# of Components}} K_i x_i$

Strategy - Assume a T, then calculate $\sum y_i$, if $\sum y_i \neq 1.0$, then iterate about T until.

T_{Bottom} = 397 7 K P_{total} = 1.01 bar

Components	x_i	K_i	$y_i = K_i x_i$
Isopropanol	0.000	1.878	0.000
Butanol	0.023	1.096	0.025
2-methoxyethanol	0.977	0.998	0.975
		$\sum y_i$	1.000

Distillate's Dew Point Calculation

Dew Point Equation
$$\sum_{i=1}^{\text{\# of Components}} x_i = \sum_{i=1}^{\text{\# of Components}} \frac{y_i}{K_i}$$

Strategy - Assume a T, then calculate $\sum x_i$, if $\sum x_i \neq 1.0$, then iterate about T until.

$T_{\text{Distillate}} = 356\ 3\ \text{K}$ $P_{\text{total}} = 1.01\ \text{bar}$

Components	y_i	K_i	$x_i = y_i / K_i$
Isopropanol	0.990	1.008	0.982
Butanol	0.100	0.545	0.018
2-methoxyethanol	0.000	0.525	0.000
		$\sum x_i$	1.000

Average Column Temperature

$$T_{\text{Column}} = \frac{T_{\text{Distillate}} + T_{\text{Bottom}}}{2} = \frac{356.3 + 397.7}{2} = 377.0\ \text{K}$$

154

Relative Volatility's

$$\alpha_{\text{Temperature},i,j} = \frac{K_i}{K_j}$$

Component	K_I	$\alpha_{\text{Column},LK,HK}$
Isopropanol (LK)	1.41	1.77
Butanol (HK)	0.79	1.00
2-methoxyethanol	0.74	0 93

of Theoretical Trays at Infinite Reflux

Fenske Equation

$$N_{min} = \frac{\ln \dfrac{x_{D,LK} / x_{B,LK}}{x_{D,HK} / x_{B,HK}}}{\ln (\alpha_{\text{Column},LK,HK})} - 1 = 28 \text{ Trays}$$

Minimum Reflux Ratio Calculation

Underwood's method used (Underwood, 1948)

Assume a φ, then correct it to match the following equation

$$1-q = \sum_{i=1}^{\#\text{Components}} \frac{\alpha_i x_{\text{Feed},i}}{\alpha_i - \varphi}$$

Then find R_{min} by the following equation

$$R_{min} = \sum_{i=1}^{\#\text{Components}} \frac{\alpha_i x_{\text{Feed},i}}{\alpha_i - \varphi} - 1$$

$$q = -\frac{Cp_v (T_{\text{Feed}} - T_{\text{Distillate}})}{\lambda} , \text{ for saturated feed.}$$

$Cp_v = 114.8$ J/mol*K $\lambda = 45,200$ J/mol , constants based on butanol pure component

values from NIST Chemistry WebBook

$$q = -\frac{114.8(396\ 25 - 356\ 3)}{45,200} = -0.10$$, T_{Feed} calculated in the same way as bottom's bubble

point temperature

For $\varphi = 0.085$, the first equation is true ($1.10 = 1\ 10$)

Thereby, $R_{min} = 0.05$

Number of Theoretical Plates at Operating Reflux Ratio

Gilliland Correlation used (Gilliland, 1940)

$$\frac{R - R_{min}}{R + 1} = 0.90$$

From correlation, $\dfrac{N - N_{min}}{N + 1} = 0.03$, and thereby, $N = 30$

Actual Number of Trays

N_{Actual} = # of Theoretical Trays / Tray Efficiency = 38

Distillation Column Sizing (YBCO Unit)

Basis

Yearly Number of Batch Runs: 53

Feed Per Batch   43,665 moles 2-Methoxyethanol

                                    1,607 moles Isopropanol

Antione's Constants

Component	A	B	C
Isopropanol	4.86	1,357 43	-75.81
2-methoxyethanol	5.06	1,853.56	-30.84

Molar Compositions & Flowrates:

Component	Distillate Mole Fraction	Bottoms Mole Fraction	Distillate Molar Flow Rate mol / s	Bottoms Molar Flow Rate mol /s
Isopropanol	0.90	0.0037	0 739	0 082
2-methoxyethanol	0 10	0.9963	0 082	22 231

Operating Reflux Ratio.   10

Tray Efficiency·   80%

<u>Bottom's Bubble Point Calculation</u>

Distribution Coefficient $K_1 = \dfrac{P_1}{P_{Total}}$, assuming Raoult's & Dalton's Laws

Bubble Point Equation $\displaystyle\sum_{i=1}^{\#\,of\,Components} y_i = \sum_{i=1}^{\#\,of\,Components} K_i x_i$

Strategy - Assume a T, then calculate $\sum y_i$, if $\sum y_i \neq 1.0$, then iterate about T until.

$T_{Bottom} = 397.6\ K$ $P_{total} = 1.01$ bar

Components	x_i	K_i	$y_i = K_i x_i$
Isopropanol	0.0037	1.876	0.007
2-methoxyethanol	0 9963	0.997	0.993
		$\sum y_i$	1.000

Distillate's Dew Point Calculation

Dew Point Equation
$$\sum_{i=1}^{\text{\# of Components}} x_i = \sum_{i=1}^{\text{\# of Components}} \frac{y_i}{K_i}$$

Strategy - Assume a T, then calculate $\sum x_i$, if $\sum x_i \neq 1.0$, then iterate about T until.

$T_{\text{Distillate}} = 361.0 \text{ K}$ $P_{\text{total}} = 1.01 \text{ bar}$

Components	y_i	K_i	$x_i = y_i / K_i$
Isopropanol	0.90	1.009	0.824
2-methoxyethanol	0.10	0.569	0.000
		$\sum x_i$	1.000

Average Column Temperature

$$T_{\text{Column}} = \frac{T_{\text{Distillate}} + T_{\text{Bottom}}}{2} = \frac{361.0 + 397\ 6}{2} = 379.3 \text{ K}$$

Relative Volatility

$$\alpha_{i,j} = \frac{K_i}{K_j} = \frac{1.45}{0.76} = 1\ 90$$

of Theoretical Trays at Infinite Reflux

Fenske Equation $\qquad N_{min} = \dfrac{\ln \dfrac{x_{D,LK} / x_{B,LK}}{x_{D,HK} / x_{B,HK}}}{\ln \left(\alpha_{Column,\ LK,HK} \right)} - 1 = 18$ Trays

Minimum Reflux Ratio Calculation

Underwood's method used (Underwood, 1948)

Assume a φ, then correct it to match the following equation

$$1-q = \sum_{i=1}^{\# Components} \dfrac{\alpha_i x_{Feed,i}}{\alpha_i - \varphi}$$

Then find R_{min} by the following equation

$$R_{min} = \sum_{i=1}^{\# Components} \dfrac{\alpha_i x_{Feed,i}}{\alpha_i - \varphi} - 1$$

$$q = - \dfrac{Cp_v (T_{Feed} - T_{Distillate})}{\lambda}, \text{ for saturated feed}$$

$Cp_v = 108$ J/mol*K $\quad \lambda = 45{,}200$ J/mol , constants based on IPA pure component values

from NIST Chemistry WebBook

$$q = - \dfrac{108(395.6 - 391.0)}{45{,}200} = -0.08, \ T_{Feed} \text{ calculated in the same way as bottom's bubble}$$

point temperature

For $\varphi = 0.075$, the first equation is true $(1.08 = 1.08)$

Thereby, $R_{min} = 0.05$

Number of Theoretical Plates at Operating Reflux Ratio

Gilliland Correlation used (Gilliland, 1940)

$$\dfrac{R - R_{min}}{R + 1} = 0.90$$

From correlation, $\dfrac{N - N_{min}}{N+1} = 0.03$, and thereby, N = 20

Actual Number of Trays

N_{Actual} = # of Theoretical Trays / Tray Efficiency = 25

Distillation Columns Sizing (Identical Units for YBCO & LaAlO$_3$)

Distillation Column's Flowrate Restrictions

Max Allowable Vapor Velocity (V) $V = K_v \sqrt{\rho_G(\rho_l - \rho_G)}$, from

Peters & Timmerhaus pp 656-7

$\rho_G = 0.12\,lb/ft^3$ $\rho_L = 60\,lb/ft^3$, Property Data of 2-methoxyethanol

K_v = 0.12 ft / s, from Peters & Timmerhaus p.657, assuming 6" tray spacing

$V = (0.12ft/s)\sqrt{(0.12lb/ft^3)(60lb/ft^3 - 0.12lb/ft^3)} = 0.321\ lb/s*ft^2$

$A_{Column} = \pi(\dfrac{(1ft)}{2})^2 = 0.79\ ft^2$, 5% of area is assumed to be devoted to downcomers,

thereby, A_{Column} = 0.75 ft^2

$V = (0.75ft^2)(0.321lb/sft^2) = 0.24$ lb / s = 0.11 kg /s = 1.4 moles / sec, assuming molecular

weight of vapor the same as 2-methoxyethanol (75.65 g /mol)

$V_{operating}$ = (70%)(V) = 1 mol / sec, a "rule of thumb" from Peters & Timmerhaus

Condenser Sizing

$Q = DCp_v(T_{Feed}-T_{Distillate})+DH_{vap}+DCp_l(T_{Distillate}-T_{Coolant})$, where Q is the heat required, D

is the distillate molar flow rate, Cp_v is the constant pressure heat capacity of the vapor

phase, Cp_l is the constant pressure heat capacity of the liquid phase, H_{vap}, is the enthalpy

of vaporization

$T_{Coolant} = 293$ K

$$D = V_{operating}/(1+R) = \frac{(1\,mol/s)(3600s/hr)}{(1+(10))} = 3285 \text{ moles/hr, where R is the reflux ratio,}$$

and $V_{operating}$ is the operating vapor molar flow rate

$Cp_v = 114.8$ J / mol K , $Cp_l = 180$ J / mol K , $H_{vap} = 40,000$ J / mol from NIST Chemistry

WebBook for IPA

$Q = (3285mol/hr)(114.8J/mol\,K)(396.25K\text{-}356.3K)+(3285mol/hr)(40,000J/mol)$

$\qquad +(3285mol/hr)(180J/mol\,K)(356.3K\text{-}293K) = 183,889$ kJ/hr $= 174,327$ Btu/hr

$Q = UA(T_{in}\text{-}T_{out})$, $A = Q / U\,(T_{in}\text{-}T_{out})$, where U is the heat transfer coefficient, A is heat

exchanger area, T_{in} is the temperature of the distillate entering the heat exchanger, and

T_{out} is the temperature of the distillate exiting the heat exchanger

$U = 50$ Btu / hr ft^2 °F, assuming water coolant with Peters & Timmerhaus estimates

$\qquad$ on p. 660

$(T_{in}\text{-}T_{out}) = (396.25K\text{-}293K) = (253.58°F\text{-}68°F) = 186°F$

$$A = \frac{174,327 \text{ Btu / hr}}{(50 \text{ Btu / hr ft}^2 \text{ °F})(186° \text{ F})} = 19 \text{ ft}^2$$

Dip-Coating Thickness Calculations From Withdrawal Rate Data

Film Thicknesses were derived using an empirical form of the analytical equation

presented in work by Vineet Lasrado (1998). The analytical form presented in Vineet

Lasrado's thesis was: $t_{film} \equiv C\left(\dfrac{\rho}{\rho_{TH}}\right)\left(\dfrac{0.944(\mu V_w)^{2/3}}{(\sigma)^{1/6}(\rho g)^{1/2}}\right)$

Where C is solution-loading factor, ρ is density of precursor solution, ρ_{TH} is the density

of the crystalline LaAlO$_3$, Φ is surface tension of precursor solution, : is the viscosity of

the precursor solution, V_w is the withdrawal velocity, g is the gravitational constant, and

t_{film} is film thickness

An empirical form of this equation was made by combining all the property constants

into one constant, a, which can be determined empirically from data presented in

Lasrado's work. The variable, Vw, is still kept to it's form.

Thereby, that empirical equation is:

$t_{film} = a(V_w)^{2/3}$

Where a is a constant with units Å/(cm min)$^{2/3}$, V_w is given in (cm / min), and t_{film} is

given as Å

Data from Lasrado (1998): t_{film} = 1200 Å at withdrawal rate = 3 cm / min

Solving the empirical equation for a based on data yields a = 576.9 Å /(cm min)$^{2/3}$

Thus, the empirical equation is given the form $t_{film} = 576\ 9(V_w)^{2/3}$

This was determined from the following figure.

Thin-film Thickness vrs Velocity
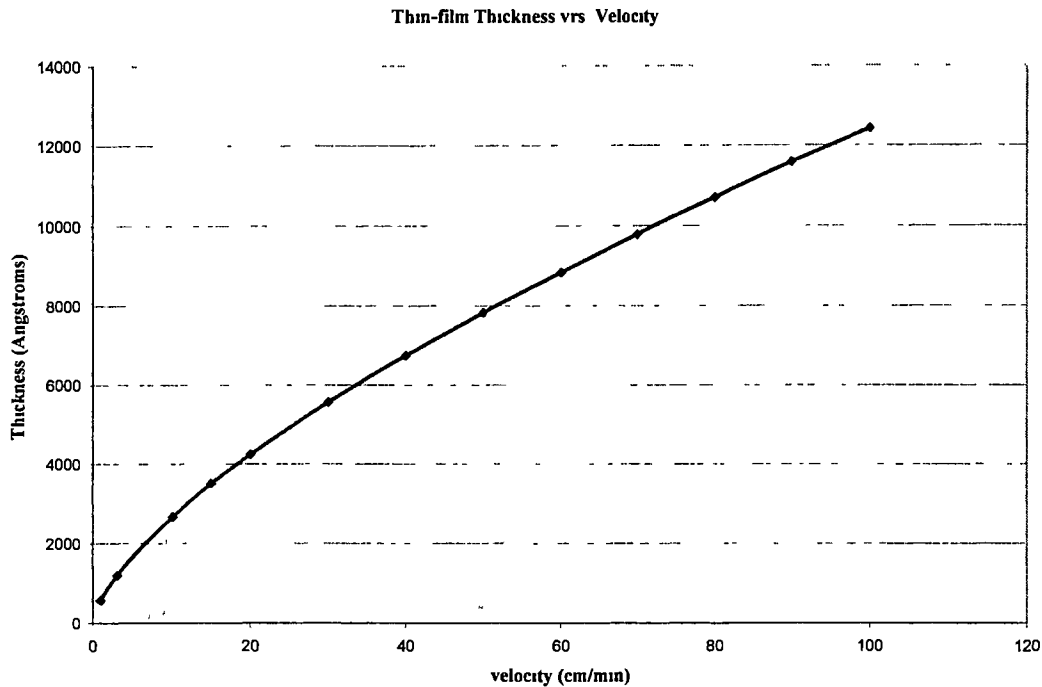
LaAlO₃ Dip-Coater Line Speed Calculation

Minimum Continuous Production Rate For All Lines: 5.27 m / min

(Which is equivalent to 2,769,231 m / year of 10 cm wide tape produced non-stop to produce

27,000,000 m / year of 1 cm wide product tape at full plant capacity)

Assume V_w = 10 cm / min

$t_{film} = 576.9 \, (10)^{2/3} = 2,680$ Å

Number of Dip Coating Units (1 Unit Consists of 1 Pyrolyzer & 1 Coater)

Example: LaAlO₃

Film Thickness 10,000 Å   Deposited Amount per Coater. 2,680 Å

$V_w = 10$ cm / min

$$\text{\# Dip Coating Units in Series (per line)} = \frac{10,000}{2,680} \approx 4$$

Total Process Time = Uptime + Downtime

Uptime = (10 cm / min)*(1000 m/spool)*(0.01 m / cm) = 10,000 min

Downtime was assumed as 120 min per spool

Total Process Time = 10,120 min

$$\text{Yield per line} = \frac{(365 * 24 * 60 \text{min/year})}{(10,120 \text{ min/spool})} \approx 52 \text{ spools / year}$$

$$\text{\# Lines Required} = \frac{(2,769,231 \text{ m/year})}{(1,000 \text{ m/spool})} \approx 54$$

Assume: 3 lines in parallel can be run through one coating unit

$$\text{\# Dip Coating Units} = \frac{(54\{\#\text{lines}\})(4\{\#\text{Coaters In Series}\}))}{(3\{\#\text{lines in parallel}\})} \approx 72$$

Retort Furnace System Sizing

Basis

Minimum Continuous Production Rate For All Lines: 5 27 m / min

Maximum Length per Charge per Furnace Unit.   3 km or 3 spools

Assumed Loading / Unloading Time of 120 min (Includes heating & cooling down time for parts)

LaAlO$_3$ Crystallization

164

Process Time: 60 min for crystallization + 120 min loading

/ unloading = 180 min total

Length per Charge = (5.27 m / min) * (180 min) = 948 m

# of Units = 948 / 3,000 ≈ 1

YBCO Crystallization

Process Time: 1740 min for crystallization + 120 min
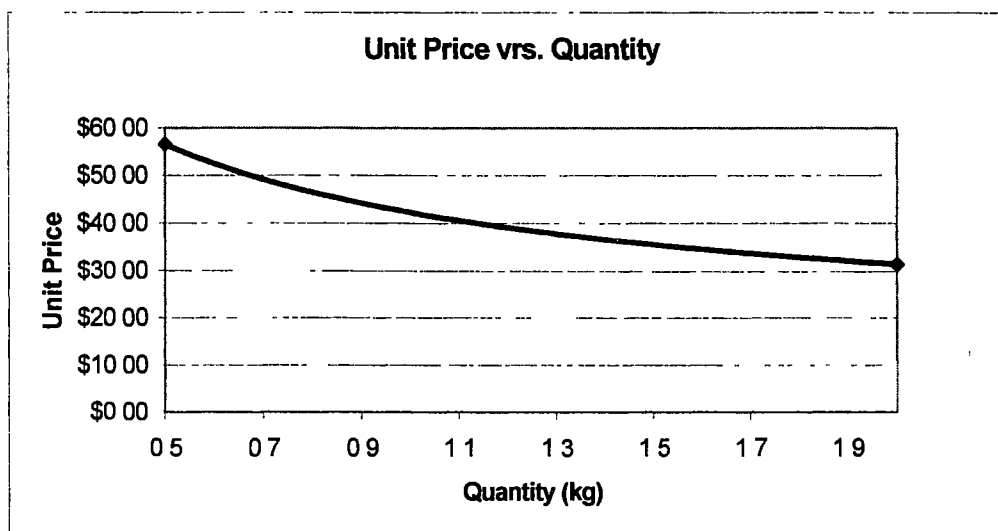
loading / unloading = 1860 min total

Length per Unit per Charge = (5.27 m / min) * (1860 min) = 9802 m

# of Units = 9802 / 3,000 ≈ 4

Raw Material Price Scaling

Aluminum Sec-Butoxide

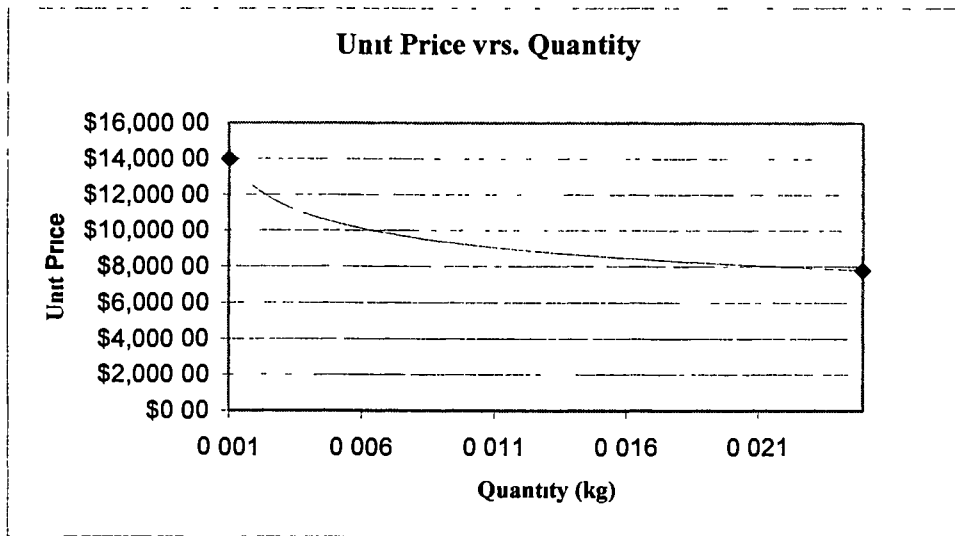1999-2000 Alpha Aesar Catalog Prices   0.5 kg $28.30

2.0 kg $63.00

Unit Price vrs. Quantity

Power-Series Regression Model Based On Data

Unit Price = $42.224(Quantity)^{-0.4227}$

Unit Price = $42.224(3,339)^{-0.4227} = \$1.37 / kg = \$0.62 / lb$

Copper (II) Methoxide

1999-2000 Alpha Aesar Catalog Prices   0.001 kg $14.00

    0.025 kg $195.00

Unit Price vrs. Quantity

Power-Series Regression Model Based On Data

Unit Price = $3990(Quantity)^{-0.1817}$

Unit Price = $3990(3,257)^{-0.1817} = \$918 / kg = \$417 / lb$

Labor Estimation

Working Hours Per Year Per Employee.   1792 (Chapman, 1998)

Average Salary Per Employee: $25.00 (Chapman, 1999)

166

Shift Workers

Duty	# employees per shift
Nickel Processing Operator	1
Precursor Processing Operator (YBCO & LaAlO$_3$)	1
Retort Furnaces Operator	1
Dip Coating Units Operator	5 (1 operator per 50 lines)
Passivation & Slitting	1
Maintenance	3
Shift Manager	1
Engineer	2
Janitorial	2
Receiving & Shipping	2
Materials Management	3
Loaders/Unloaders {Spools}	8

Shift Workers = 31

Total Shift Workers = (31)*(24 * 65 hrs) / (1792 working hours per employee) = 152

Nonshift Workers

Secretary & Accountants	2
Purchasing	2
Plant Manager	1

Total Workers = 157

Annual Labor Cost minus = (157)*($25.00/hour)*(1792 working hours) = $7,010,000

{Minus fringe benefits)

VITA

Kevin Trembath was born in Warren, Ohio on October 4th, 1975. He graduated high school from Newton Falls High School (Newton Falls, Ohio) in 1994. He attended the University of Detroit Mercy from 1994 to 1998. He received a bachelor's of chemical engineering degree in August, 1998 He directly entered the Master of Science in Chemical Engineering at the University of Tennessee, Tullahoma. As of August 2000, he earned his MS degree Kevin Trembath is presently working as a chemical engineer for Lexmark International (Lexington, Kentucky)